Vibration-Based Monitoring and Damage Simulation of an Extradosed Cable-Stayed Bridge

By

Arnold Vendiola

A thesis submitted in partial fulfillment of the requirements for the degree of

Master of Science

in

STRUCTURAL ENGINEERING

Department of Civil and Environmental Engineering

University of Alberta

ABSTRACT

Most of Canada's municipal infrastructure, including bridges, was built between the 1950s and 1970s. With design lives of 50-100 years, many of these structures are due for major rehabilitations or replacements. With the growing costs of deteriorating infrastructure, the cost savings from properly maintained structures are increasing in importance (Mirza, 2007). The use of Structural Health Monitoring (SHM), which uses sensor technology paired with data acquisition and analytical models to quantify various bridge parameters such as strain, vibration, and displacement, has been growing in popularity in recent years. The use of SHM systems can provide objective measurements which can supplement current inspection methods, such as visual inspections which can be prone to bias and inconsistency (Pines and Aktan, 2002).

The Tawatinâ Bridge is an extradosed cable-stayed bridge in Edmonton, Alberta, Canada, that carries light-rail vehicle (LRV) and pedestrian traffic over the North Saskatchewan River. This thesis focuses on the development of a long-term vibration-based monitoring system for the Tawatinâ Bridge with the goal of providing a framework for establishing a baseline response for future structural health monitoring and predicting the effects of various damage cases on the modal properties of the bridge using an analytical model. Twelve triaxial accelerometers were deployed in four locations along the bridge, and the modal properties were calculated from the acceleration data using a Blackman windowing function, Fast-Fourier Transform (FFT), Covariance-driven Stochastic Subspace Integration (SSI-Cov), and Modal Assurance Criterion (MAC). A model was developed using CSiBridge to determine a theoretical baseline response and perform damage simulations. The model was analyzed using an eigenvector analysis and a linear modal time history using predicted train loads. The linear modal time history was paired with an SSI-Cov algorithm to determine the modal properties of the bridge.

Data was collected from the field over ten site visits during the construction of the bridge's shared-use-pathway (SUP). Data collected in the field during ambient testing appeared to have significant noise, and it appeared that more data collection is needed to effectively measure an accurate baseline response under ambient loads. Data collected from dynamic testing appeared to have issues with synchronization which made reporting accurate mode shapes infeasible. However, the forced excitation appeared to be effective in exciting some of the natural frequencies of the bridge as shown by agreement between the SSI-Cov and FFT results. Limitations of the sensor layout and data collection methods were discussed, and recommendations for future testing were provided and applied to the analytical model.

An eigenvector analysis was performed with CSiBridge to determine the theoretical mode shapes of the bridge which may be measured during ambient conditions. A linear modal time history was also performed to investigate the theoretical behaviour of the bridge under predicted train loads. The mode shapes and natural frequencies of each damage case were compared to the baseline response to determine how effectively each damage type could be detected using the proposed damage detection scheme. In general, comparing mode shapes using MAC values appeared to be more effective at detecting damage than relying on natural frequency changes alone. Bearing damage and girder damage had the most notable impacts to the modal properties of the bridge which implies they could be easily detectable under the proposed damaged detection scheme. Stay cable damage and tower damage were found to have the least impact on the modal properties of the bridge which implies that other methods may be needed to detect damage to these components.

"Sometimes life is like this dark tunnel. You can't always see the light at the end of the tunnel, but if you just keep moving… you will come to a better place."

- Uncle Iroh, *Avatar: The Last Airbender*

Acknowledgments

I have many people to thank for their continued supported throughout the completion of this work. First of all, I would like to thank my supervisor Dr. Douglas Tomlinson for taking a chance on a wide-eyed undergrad student who shared a common enthusiasm for bridges. Thank you for your support, mentorship, and endless supply of puns. Please continue to do what you do for your students; your passion and enthusiasm for concrete and the world of structures is contagious.

To my family, especially my parents, Meynardo and Victoria Vendiola, who sparked my interest in Engineering and whose sacrifices have opened so many doors for me. Thank you for allowing me to pursue my passion, even when my choice to pursue this degree was not the easiest. I am forever grateful, and I aspire to have the same level of work ethic, resilience, and faith as the both of you.

To the University of Alberta Powerlifting Association where I have made lifelong friends and where I have essentially become furniture. Thank you for your continued friendship and camaraderie. I am who I am today in large part because of what this club has done for me. Don't worry, I'm finally leaving.

To my friends who have been my support system through late night drives, late games on PSN (can't end on a loss), deep talks over hotpot, hikes, and the like. Thank you for motivating me to keep going. We finally did it.

To my partner, Carlie Hornsby. Your belief in me over the latter half of my degree has meant more than you could ever know. Thank you for being by my side and often being my shoulder to lean on. I wouldn't be where I am without you.

Table of Contents

List of Figures

List of Tables

CHAPTER 1.   INTRODUCTION

1.1   Background

Much of the physical infrastructure in Canada, including bridges, was built between the 1950s and 1970s due to rapidly growing populations during those time periods. With common design lives of 50-100 years, many of these structures are due for major rehabilitation or replacement and there may be insufficient investment to keep up with the growing costs of deteriorating infrastructure. Cost savings related to properly maintained structures are considerable and infrastructure achieves considerably longer service life if as little of 2% of the facility cost is invested in maintenance (Mirza, 2007).

Bridges are exposed to various external factors throughout their lifetimes, including environmental effects such as wind and rain, dynamic loads from vehicles, and long-term effects such as fatigue and creep. If not maintained properly, the failure of critical infrastructure such as bridges can be catastrophic and costly. Therefore, studying the damage characteristics and disaster evolution of structures is becoming increasingly important (Li et al., 2006).

Currently, visual inspections are the most common method of bridge inspection but can be inconsistent between different inspectors. Structural Health Monitoring (SHM) uses sensor technology, paired with data acquisition and analytical models, to quantify various bridge responses such as strain, vibration, and displacement. Figure 1.1 shows the typical layout of a SHM system which typically consist of: (1) sensory system; (2) data acquisition and transmission system; and (3) data processing and control system. Monitoring systems aim to detect signs of anomalies or deterioration early so that asset managers can perform the required maintenance. These systems can be used to reduce the number of visual inspections, and the data acquired can be used to supplement the observations made – thereby reducing inconsistencies.
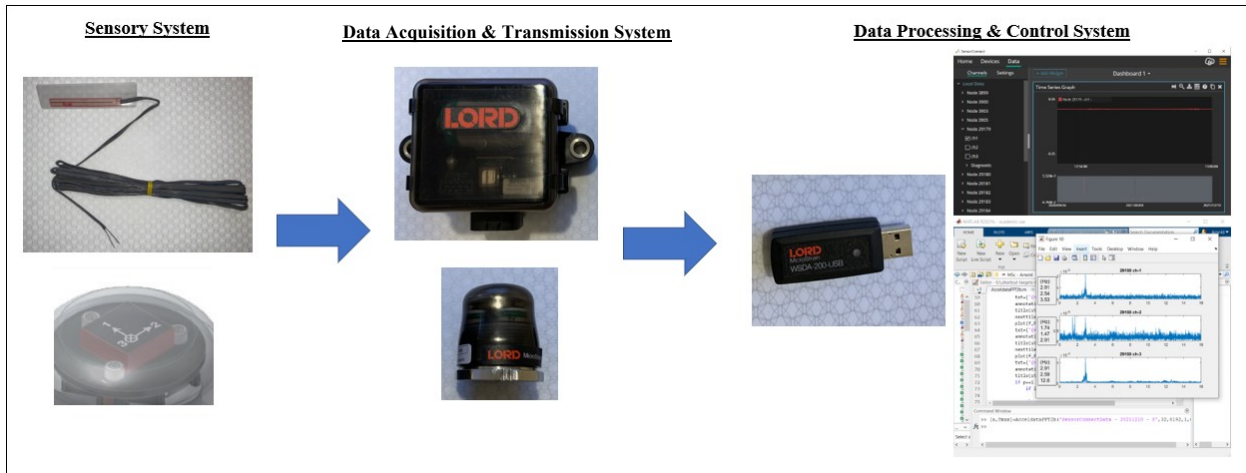
Figure 1.1. Components of a typical SHM system

As technology advances and tools become more affordable, the use of SHM has become more common in recent years (Li and Ou., 2015). There have been an increasing number of studies on the SHM of different types of bridges, but few studies focus on the SHM of extradosed bridges under live load (Guo et al., 2020)

1.2 Introduction to the Tawatinâ Bridge

The Tawatinâ Bridge is a 3-span extradosed cable-stayed bridge under construction in Edmonton, Alberta, Canada. The bridge is part of Edmonton's Valley Line Southeast light-rail transit (LRT) line which carries light-rail vehicle (LRV) and pedestrian traffic over the North Saskatchewan River. The bridge tower has an open shape with two outer cable planes that each hold seven stays (14 stays in total). Stay angles for the bridge range from 26.2º to 17.4º relative to the horizontal. The bridge consists of two cable supported spans that are 100 m and 110 m in length, along with an adjacent continuous 50 m span. The bridge superstructure has a cast-in-place 3.5 m tall by 11 m wide post-tensioned trapezoidal box girder. Beneath the bridge deck is an 8 m wide steel, timber, and asphalt shared-use pathway (SUP) suspended by steel rods attached to the bottom of the box girder.

1.3 Objectives and Scope

The objectives of this study are to provide a framework for a monitoring system that can effectively establish a baseline response for future structural health monitoring of the Tawatinâ Bridge and predict the effects of various damage cases on the modal properties of the bridge using an analytical model. To achieve these objectives, the following tasks were completed:

1. Conduct a literature review on current bridge monitoring and structural health monitoring methods to understand the current state of the art to assist with determining a sensor layout for the Tawatinâ bridge;

2. Collect data from the field over 2-3 months during construction of the shared-use pathway and process the data using relevant methods explored in Task 1 to provide a framework for establishing a baseline response for future monitoring, and provide recommendations for future testing based on the results;

3. Develop an analytical model using CSiBridge and establish a theoretical baseline response, then simulate damage by applying stiffness or tension reductions to different components of the bridge;

4. Analyze the model results under ambient conditions and simulated dynamic loading then compare the results with the baseline response to determine how each damage case affects the baseline response.

The scope of this research is limited to vibration-based structural health monitoring of the Tawatinâ bridge, and the sensors were placed in such a way that only global parameters could be detected. The analytical model is a simplified model developed using CSiBridge which does not include the shared-use-pathway. Model updating is recommended for future work but is outside the scope of this study.

1.4   Thesis Organization

This thesis is divided into seven chapters, and their content is described as follows:

Chapter 1:   Presents the purpose of the study, including the objects and scope.

Chapter 2:   Presents a literature review on bridge monitoring methods and current structural health monitoring research, including: destructive and non-destructive methods, an overview of structural health monitoring systems, and applications of structural health monitoring systems on real life structures. Chapter 2 addresses *Task 1*.

Chapter 3:   Establishes the methodology for collecting and analyzing field data and developing the analytical model. The proposed sensor layout and data collection method are presented. The damage cases and loading conditions to be considered for the damage simulations using the

analytical model are also presented. Chapter 3 addresses part of **Task 2**, **Task 3**, and **Task 4**.

Chapter 4:   Discusses the results of ambient and dynamic testing performed in the field and collected using the proposed sensor layout. Limitations of the proposed sensor layout and data collection methods are discussed, and recommendations are made for future study. Chapter 4 addresses *Task 2*.

Chapter 5:   Discusses damage simulations performed on the analytical model analyzed using an eigenvector analysis to determine the theoretical modal properties of the bridge under ambient loading. Modal properties between the baseline and damage cases are compared to determine the effects of each damage case. Chapter 5 addresses *Task 3* and part of *Task 4*.

Chapter 6:   Discusses the damage simulations performed on the analytical model subjected to train loads to simulate real life excitation of the bridge. Modal properties are calculated for each damage case and compared with the baseline to determine the effects of each damage case. Chapter 6 addresses *Task 3* and the rest of *Task 4*.

Chapter 7:   Summarizes the entire thesis, including the results and conclusions from Chapters 4, 5, and 6. Recommendations for future study provided in previous chapters are also included.

CHAPTER 2.   LITERATURE REVIEW

2.1   Review of Bridge Monitoring Methods

Structural health monitoring is the process of assessing the nature of damage in a structure and tracking changes in parameters related to structural integrity. In highway bridges, concrete degradation, steel corrosion, boundary condition changes, and weakening of connections are major concerns. Wu (2021) found that prestressed concrete box girders with severe corrosion experienced diagonal tension failure and loss of capacity compared to girders without severe corrosion. Anchorage issues can develop as a result and lead to catastrophic failure (Wu, 2021). Structural health monitoring can be divided into global health monitoring and local health monitoring. Structural health monitoring at global levels focuses on detecting the presence and location of damage using global properties of the bridge through methods such as vibration monitoring and determining the modal properties of the structure. Local health monitoring systems focus on determining the extent, location, and severity of damage and include methods such as audio-visual tests (Rehman et al. 2016).

Generally, methods for evaluating the strength and condition of a structure can be divided into destructive testing or non-destructive testing. Destructive testing consists of loading structures or elements until failure. This type of testing is typically conducted in a laboratory setting. Due to the high costs of destructive testing and its impracticality for bridge structures that are in service, non-destructive testing is typically used for evaluating bridge structures. Non-destructive testing (NDT) or non-destructive evaluation (NDE) consists of testing structures, often in-situ, under various load conditions. A common NDE method for bridge structures is visual inspection. In Alberta, highway bridges are inspected following provisions in the Alberta Transportation Bridge Inspection and Maintenance (BIM) manual which provides a rating system for the visual inspection of critical bridge elements such as superstructure, substructure, and culverts (Alberta Infrastructure and Transportation, 2008). However, various studies have shown the limitations of visual inspection. Bennetts et al. (2018) compared the scoring of defects by pairs of independent inspectors across 200 bridge structures on England's strategic road network. They found significant uncertainty in classifying and grading individual defects during visual inspections. To supplement visual inspections, other forms of non-destructive testing such as dynamic testing have been used. Dynamic testing methods may involve forced excitation using a measured input such as impact testing (e.g., dropping a known weight, striking with an impact hammer) or a mass shaker. Another

method of dynamic testing is ambient testing which involves the excitation of a bridge under typical operating conditions using ambient loads such as wind, traffic, and seismic excitation (Farrar et al. 1999).

2.2 Overview of Non-Destructive Testing Methods

NDT methods are used to examine structural damage or deterioration quickly and effectively. Damage includes concrete delamination, seepage, reinforcement corrosion, cracks, and voids. Without proper intervention, cracking and corrosion can lead to premature deterioration and reduced deflections at failure. In severe cases where prestressing tendons are corroded, girders can experience sudden failure before yielding. Failure in the linear-elastic range is very undesirable as the failure mode is brittle and provides little warning before collapse (Wu, 2021).

NDT methods are typically used as additional checks or when direct physical measurements (e.g., destructive testing) are impractical or too expensive. Typical applications of NDT include quality control in new construction, condition assessments of existing structures, and quality assurance of repair works. NDT can be divided into audio-visual methods, stress-wave methods, electro-magnetic methods, deterministic methods, and miscellaneous testing (Rehman et al. 2016).

2.2.1 Audio-Visual Methods

Audio-visual testing methods include visual inspections and acoustic methods that detect possible deterioration based on changes in sound along different sections of a bridge deck. Visual inspections can effectively examine visible surfaces for cracking, seepage, spalling, exposed reinforcement, staining, moisture ingress, beam delamination, concrete deterioration, and reinforcement corrosion. Speed and low cost are major advantages of visual inspections. A disadvantage to visual inspections is that damage can only be detected once it has reached the surface; the actual extent of the damage may be worse than expected. Visual inspections can also be subject to inspector's biases as a study conducted by the Federal Highway Administration found that at least 56% of condition ratings were incorrect with a 95% probability. The accuracy of condition ratings was based on the NDE Validation Center reference condition ratings, and the number of inspectors who correctly identified documented bridge defects (Pines and Aktan, 2002).

Chain dragging and coin tap tests are simple examples of acoustic testing (Figure 2.1). The basis of acoustic testing is that the presence of defects and delamination changes the frequency of oscillation, thereby changing the audible response of the deck. Chain dragging involves dragging steel chains on the surface of a bridge deck and marking locations where dull/hollow sounds are

produced (Rehman et al. 2016). Barnes et al. (2008) showed that chain-drag and ground-penetrating radar tests produced similar results within thresholds set by the authors. Coin tap tests involve striking areas under investigation with a coin or lightweight hammer to produce echo or ringing. Damaged locations are indicated by significant changes in audible frequency (Rehman et al. 2016). Cawley and Adams (1988) performed a coin tap test on an aluminum beam with milled slots to simulate delamination. When plotting force-time histories of the impacts, it was found that the impact duration increased, and peak force decreased as the impact approached the defect.
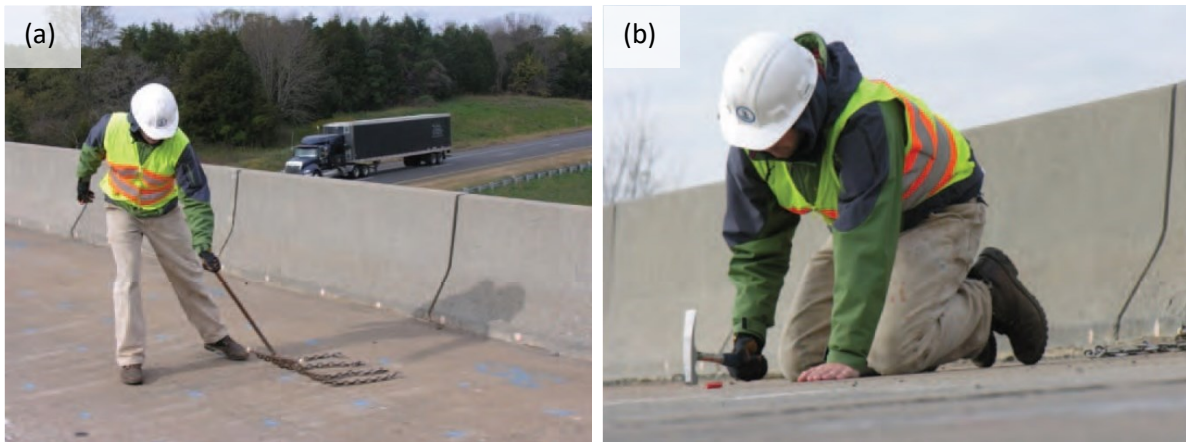
Figure 2.1. (a) Chain dragging (b) Lightweight impact hammer (Transportation Research Board of the National Academies, 2013).

2.2.2 Stress Wave Methods

Stress-wave methods involve transmitting stress waves via impact or deformation and analysing the frequency changes of the stress-waves to locate damaged areas. The presence of defects such as cracks have been experimentally shown to cause a significant decrease in the amplitudes of time signals (Kocherla and Subramaniam, 2020; Rucka and Wilde, 2013). Common examples of stress wave methods include ultrasonic pulse velocity and impulse response. Ultrasonic pulse velocity measures relative concrete condition based on the travel time of ultrasonic waves over a known path length (Figure 2.2). Velocities in deteriorated regions will be significantly lower than those in intact regions since a small amount of the energy emitted is reflected where defects are present. Impulse response (Figure 2.3) is typically used for deep foundations and involves producing low-strain impact stress waves using an impact hammer. This method measures the frequency of the stress waves and relies on the assumption that the structure's response can be approximated by a single degree-of-freedom system (Rehman et al. 2016).
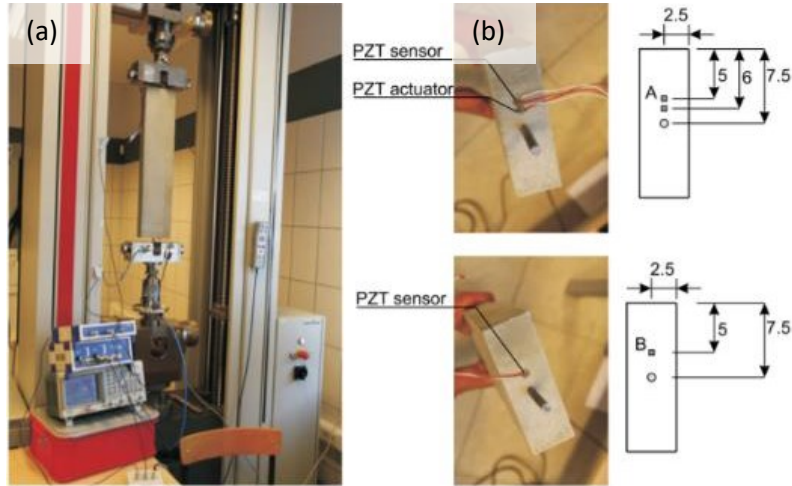
Figure 2.2. (a) Ultrasonic pulse velocity test setup for specimen under tensile loading. (b) Locations of piezo-electric transducers (PZT) (Bogas et al. 2013)
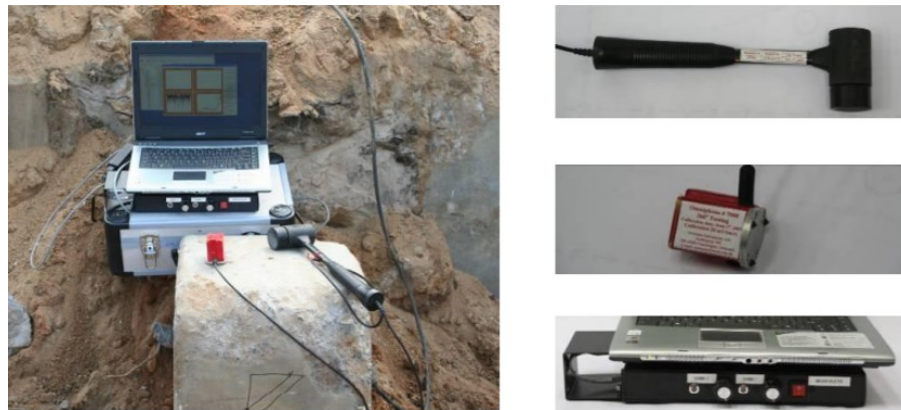
Figure 2.3. Typical impulse response test setup and equipment (Gorzelanczyk et al., 2009)

2.2.3   Electro-magnetic Methods

Electro-magnetic methods involve transmitting electromagnetic pulses through areas of interest. Deterioration can be detected based on changes in conductivity, voltage, or travel time and velocity of pulses. Ground penetrating radar (GPR), shown in Figure 2.4, is a well-known method for detecting sub-surface damages like delamination, voids, cracks, reinforcement diameter, member thickness, abnormal moisture content, settlement, and deformation induced by strain. High-frequency electro-magnetic waves are transmitted and reflected to the surface where rebar or other anomalies (such as defects) are present (Transportation Research Board of the National Academies, 2013). Conductivity tests can be conducted by generating electromagnetic fields through a test object using transmitting coils. Several properties related to hydration of concrete affect conductivity. Contour maps of conductivity distribution can be plotted and indicate areas of

8

crack growth (Rehman et al. 2016). Tomlinson et al. (2017) tested the resistivity (inverse of conductivity) of five concrete mixtures at early-ages (younger than 28-day) subjected to two thermal cycles. They showed that resistivity is impacted by mix design (e.g. varying levels of concrete hydration, admixtures, and supplementary compounds), and temperature.
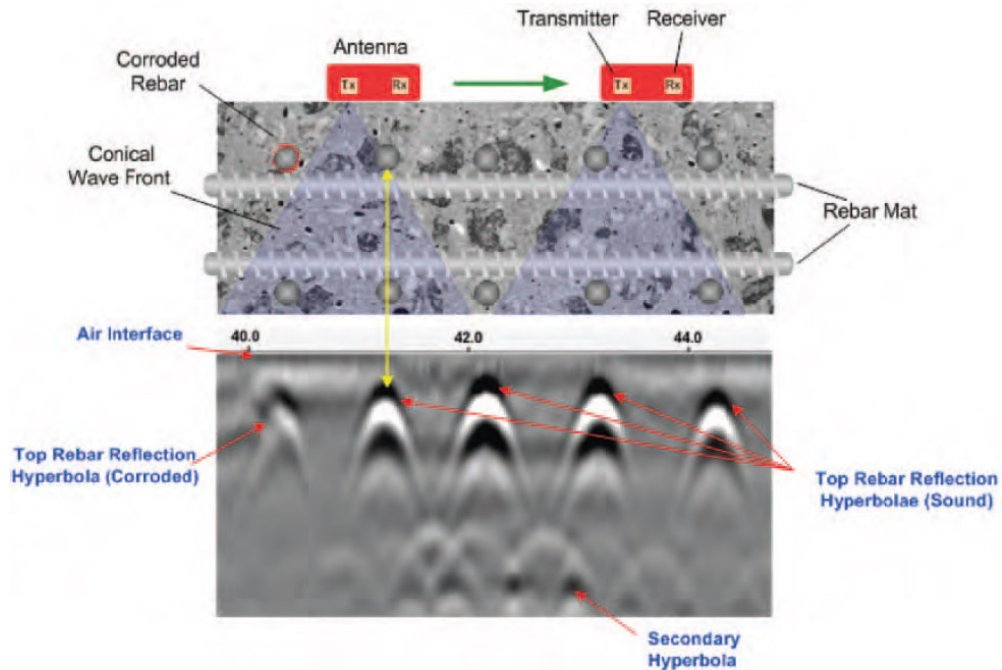
Figure 2.4. Principle of GPR testing (Transportation Research Board of the National Academies, 2013).

2.2.4 Deterministic Methods

Deterministic methods can be very expensive and include proof load testing and coring. Tests like proof loading are considered non-destructive because measures are taken to stop testing before the structure reaches irreversible damage (e.g., permanent deformation) (Olaszek et al. 2010). Proof load testing (Figure 2.5) is used to determine the actual load carrying capacity of existing structures when there is not enough information to perform an appropriate assessment (e.g., a lack of structural drawings) (Olaszek et al. 2010). The difficulty of proof load testing is estimating a target load that will not cause irreversible damages or collapse of the test structure. An accurate monitoring system is required to ensure proper loading sequence and determine the onset of non-linear behaviour to stop testing before irreversible damages occur (Casas and Gomez, 2013). Olaszek et al. (2010) tested the Barcza bridge (a three-span prestressed bridge with precast beams) and used acoustic emissions to stop loading before non-linear behaviour occurred. The bridge was

able to withstand the load applied and the load-deflection diagram showed no signs of slope change. Casas and Gomez (2013) developed a new method for obtaining target proof loads based on weigh-in-motion (WIM) data from highway locations representative of the heaviest traffic conditions within five European countries. An additional simplified method was proposed to allow extrapolation of WIM data for countries where the heavy traffic conditions may be too conservative. Coring is a semi-destructive method where cores are extracted from an existing structure and used to perform compressive, splitting tensile, and flexural strength tests. Coring can provide a reliable measure of the quality of construction and strength of the concrete in existing structures (Rehman et al., 2016).

Figure 2.5. Concrete slabs and steel blocks used for proof load testing (Olaszek et al., 2010)

2.2.5 Vibration-based Methods

Vibration-based monitoring is a common method for measuring structural health and is the focus of this research study. The method typically involves excitation of a structure using ambient loads (such as wind, traffic, etc.) or forced excitations (using measured loads and frequencies). Modal parameters, such as natural frequency, and damping, are measured. Since modal parameters are dependent on the mass and stiffness of a structure, changes in these properties can be an indicator of damage (Xu et al., 2020). The first three mode shapes typically show global behaviour and are relatively easy to obtain. Higher order mode shapes are better at signifying localized damage but are more difficult to identify accurately and typically require a large number of sensor locations (Ni et al., 2021). Figure 2.6 shows the first three mode shapes of the Komurhan Highway Bridge identified experimental using vibration-based monitoring (Bayraktar et al., 2009). Vibration-based monitoring systems are discussed in further detail in section 2.5.1.

10
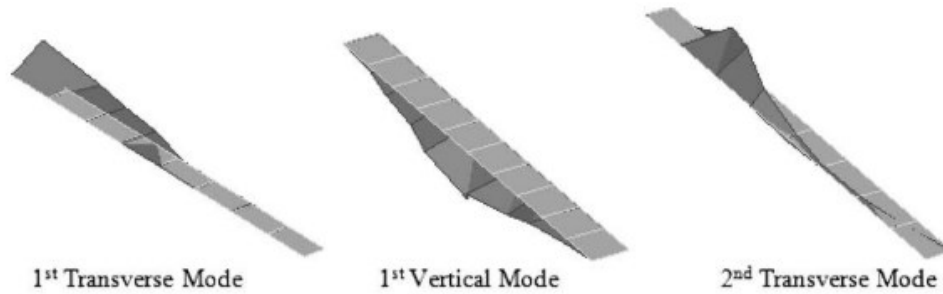
Figure 2.6. Experimentally identified mode shapes of the Komurhan Highway Bridge (Bayraktar et al., 2009)

2.2.6 Miscellaneous Methods

A method that does not fall into the previous categories is infrared thermography. Infrared thermography is a global inspection method based on two heat transfer mechanisms: radiation, and conduction. It is used for detecting delamination and anomalies on concrete surfaces since delaminated areas will heat up and cool down quickly compared to sound concrete. An infrared thermography study conducted by Raja et al. (2021) (Figure 2.7) simulated delamination inside of a concrete bridge deck. The study found that the absolute thermal contrast (ΔT) decreases as delamination depth increases and increases as delamination size increases.
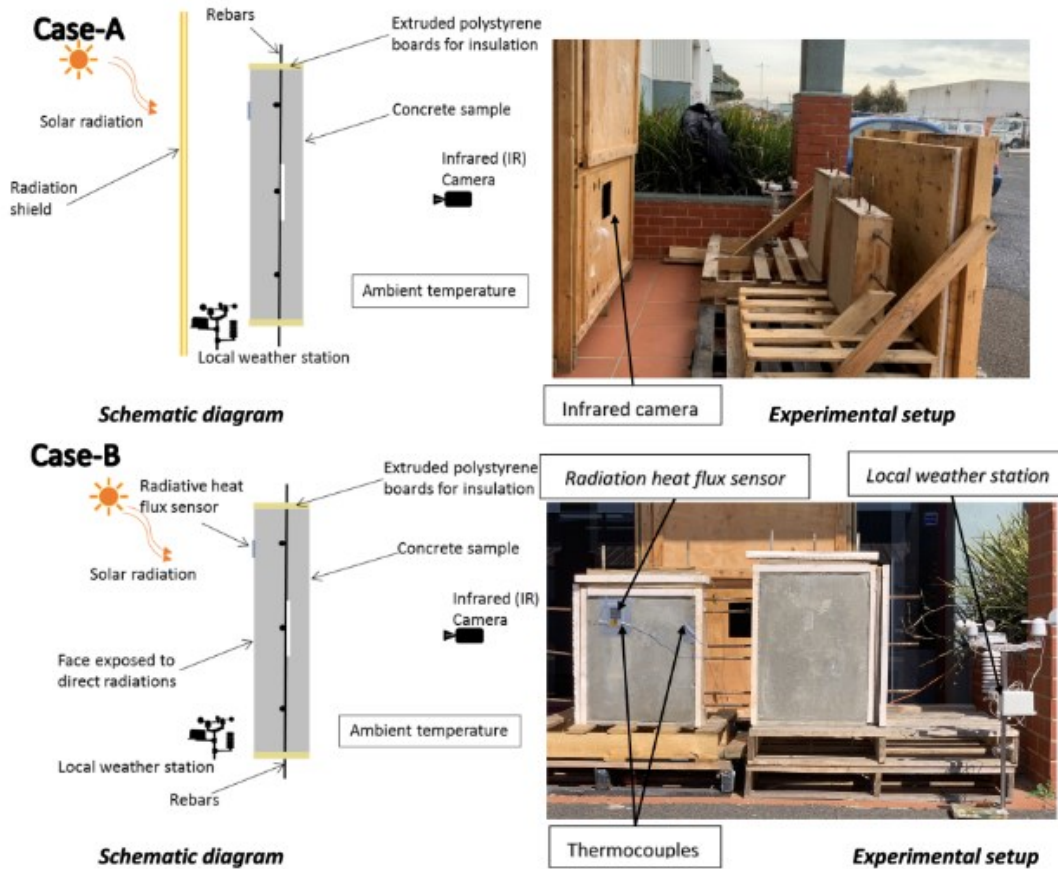
Figure 2.7. Schematic diagram and experimental setup of infrared thermography for no radiation (Case A) and indirect radiation (Case B) (Raja et al., 2021)

2.3 Overview of Structural Health Monitoring Systems

Due to rapid developments in sensor technology, Structural Health Monitoring (SHM) has become more prevalent over the past 20 years (Vardanega et al., 2016). A typical Structural Health Monitoring System (SHMS) can be divided into three modules (Figure 2.8): (1) sensory system; (2) data acquisition and transmission system; (3) data processing and control system. The sensory system is comprised of the sensors used to monitor bridge and ambient responses. Sensors are used to measure external loads, including environmental loads and traffic loads, or to monitor bridge characteristics such as vibration and stiffness. External loading can be captured using anemometers for wind or a combination of weigh-in-motion sensors and dynamic strain gauges for vehicle loads. Bridge characteristics and responses, such as deflection, vibration, and strain, can be captured using GPS systems, accelerometers, and strain gauges. The data acquisition and transmission system is comprised of nodes which store and transmit the data to gateways which collect data.

Finally, the data processing and control system consists of the software used to analyze and interpret data for decision making.
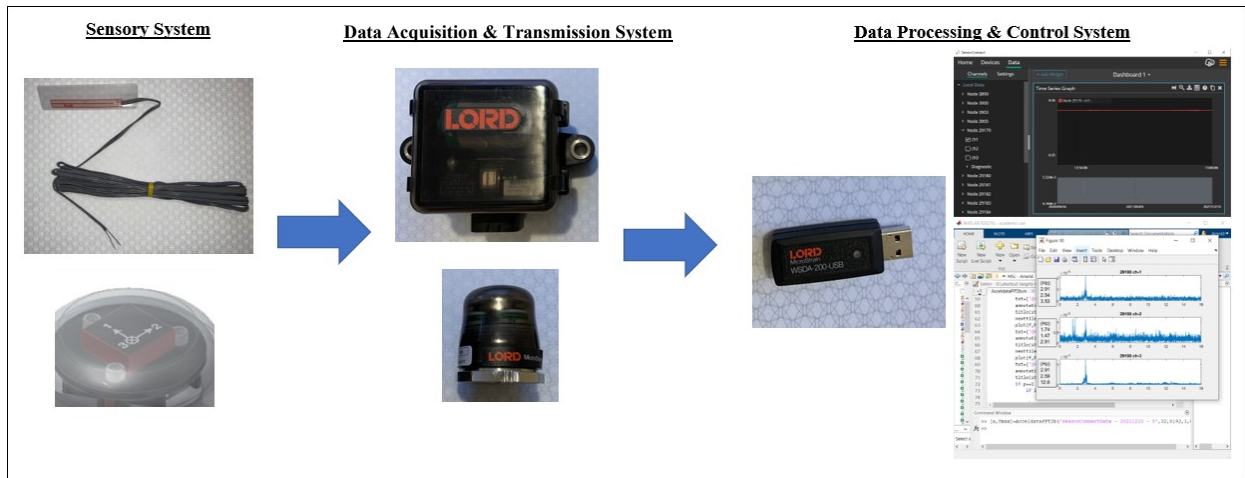
Figure 2.8. Typical SHMS

Anomaly detection involves long-term monitoring of a structure to establish a baseline response. A typical baseline response can be measured with forced or ambient excitation sources while the bridge is in sound condition. Once a baseline is established, future measurements can be used to detect anomalous events. Anomaly detection is a form of damage detection since the presence of anomalous data could imply damage or deterioration. A drawback of anomaly detection schemes is the inability to locate or measure the extent of the potential damage. However, the presence of an anomaly can initiate an investigation and allow for prompt corrective action.

Like anomaly detection, monitoring systems designed for threshold checks aim to detect when specific parameters exceed a specified value. Threshold checks are useful for monitoring specific design limits such as deflection limits, strain limits, corrosion limits, and others.

Monitoring systems designed for model validation aim to measure various parameters and compare them with a structural model. The data recorded can be used to verify design assumptions or to calibrate existing models for accurate simulation. Previous studies have even used calibrated models to perform damage simulation and set thresholds for future monitoring.

Damage detection schemes for localized damage are the most complex monitoring systems and can require upwards of 100 sensors (Li et al., 2006) compared to global damage detection which can be accomplished with as little as two sensors (Moschas and Stiros, 2011). While all the above applications provide some form of detecting damage or deterioration, monitoring systems designed

13

specifically for damage detection aim to identify the extent and location of the damage or deterioration.

2.4 Overview of Sensor Types

Sensors are used to measure either the loading on a structure or the structural response. Loads include environmental factors like wind or seismic forces and traffic loads from vehicles, trains, and pedestrians. The structural responses measured vary greatly depending on the purpose of the monitoring system but often include strain, vibration, deflection, and corrosion (Middleton et al., 2016).

2.4.1 External Load Sensors

Wind speeds are measured by anemometers while vehicle weights are commonly measured using WIM sensors. WIM sensors can provide a good measure of traffic loads, but wind speeds are not easily converted into wind load measurements.

Typical WIM sensors used for bridges measure strain responses of a bridge to determine weight, and other factors such as speed, of vehicles. WIM systems used for bridges require more complex data analysis compared to systems used for roads due to the structural response of the bridge itself and the interaction between vehicles and the bridge (e.g., vehicle suspensions and surface defects), such as vehicle suspension and the presence of potholes (FHWA, 2016).

Anemometers are a key component of wind and structural health monitoring systems (WASHMS) (Wong, 2004). Anemometers measure wind speeds using several methods like measuring rotational speeds of propellors or cups (propellor anemometers or cup anemometers), thermal cooling due to airflow (hot-wire anemometers), and detecting changes in the speed of sound waves (ultrasonic anemometers). An integrated system using GPS, accelerometers, and anemometers was used to monitor the tower displacements of the Erqi Yangtze River Bridge with millimetre precision (Han et al., 2016). Petersen et al. (2020) proposed an inverse force identification method which improves upon typical wind load assessments that rely on aerodynamic coefficients and admittance function obtained from wind tunnel tests using scale models.

2.4.2 Structural Response Sensors

Typical sensors used for measuring structural response include strain gauges, accelerometers, global positioning systems (GPS).

Measuring strain can give a good estimate of the external loads applied to a structure. Depending on the sensors, they can also be used to measure the effects of static strain (due to temperature, creep, and shrinkage) or dynamic strain (due to wind or traffic). Common strain gauges used for bridge applications include vibrating-wire strain gauges (VWSG's), fibre-optic sensors, and foil gauges. VWSG's use the changes in resonant frequency of a thin steel wire held in tension to measure strain. Fibre-optic sensors measure strains using a Fibre Bragg Grating. Foil strain gauges measure strain based on the changes in electrical resistance of a metallic foil (Xu and Xia, 2012).

Accelerometers measure vibrations and are a key component of modal analysis. Two accelerometer types common for bridge monitoring include piezoelectric accelerometers and micro-electromechanical system (MEMS) accelerometers. Piezoelectric accelerometers use a mass spring system with a small mass attached to a piezoelectric crystal to measure accelerations. MEMS accelerometers are small mechanical devices on silicon chips with an integrated analogue-to-digital convertor to produce digital outputs (Middleton et al., 2016).

GPS is commonly used to measure deflection or acceleration (via double differentiation) (Meng et al., 2007). An advantage of GPS is the ability to measure both long-term and instantaneous deflections (Meng et al., 2003). GPS and accelerometers are complementary sensors and are typically paired to improve the redundancy and accuracy of deflection and acceleration measurements (Meng et al., 2003; Meng et al., 2007; Han et al., 2016; Cheynet et al. 2019). Accelerometers are also able to provide missing data since GPS can be prone to signal outages from the multipath interference of satellites, and the relatively low sample rates are unable to accurately measure dynamic movements (Meng et al., 2003; Han et al., 2016).

2.5   Structural Health Monitoring Studies on Bridges

Seo et al. (2016) wrote a state-of-the-art paper on SHM applications for highway bridges. The basic principle for damage detection by SHM systems is that the modal properties and curve shapes of a structure are dependent on mass, damping and stiffness. Changes in the modal properties of the structure, measured by an array of sensors, can imply that damage or deterioration has occurred and affect the structure's physical parameters (mass, damping and stiffness). Several damage detection algorithms are discussed by Seo et al. (2016) which include vibration-based SHM systems and strain-based health monitoring.

2.5.1 Vibration-Based Structural Health Monitoring

Monitoring changes in natural frequencies of structures as indicators for detecting damage are a common application of vibration-based monitoring systems. Cawley and Adams (1979) developed an early damage detection algorithm using mathematical techniques to detect, localize, and quantify damage using changes in natural frequencies on an aluminum plate and a cross-ply carbon-fibre-reinforced polymer plate. Kato and Shimada (1986) conducted one of the first vibration-based monitoring studies on a damaged bridge by performing static loading of a 24 m main span prestressed concrete bridge until failure while the bridge was under simultaneous ambient vibration. The study found that the natural frequency of the first vertical mode shape decreased as static loading cycles increased until failure, implying the stiffness of the bridge reduced as damage increased. These findings were compatible with Huth et al. (2005) who simulated damage by replacing a bridge bent with hydraulic jacks and lowering the superstructure in stages to produce cracking. The study found mode shapes paired with natural frequencies to be the most sensitive damage indicators at the early stages of damage in prestressed concrete bridges. Farrar et al. (1994) carried out a SHM test on a steel girder bridge going over the Rio Grande that was taken out of service in 1993. Four damage states related to fatigue cracking were simulated using continuous cuts to the web and bottom flange of the girders. The natural frequencies were plotted to examine how natural frequencies change with structural stiffness and showed that a large reduction in bending stiffness was required to find a measurable change in modal frequencies. Mode shapes, however, were found to be more sensitive indicators of damage. After the work by Farrar et al. (1994), several studies adopted the method of saw-cutting girder webs and bottom girders to simulate fatigue damage (Seo et al. 2016). Kim and Stubbs (2003) developed a non-destructive crack detection algorithm using changes in mode shapes and natural frequency to locate and estimate the size of cracks in a damage-induced girder. The method showed the feasibility of accurately locating and estimating crack sizes with as few as three natural frequencies and mode shapes measured before and after damage (Kim and Stubbs, 2003). Peeters and De Roeck (2001) investigated the effects of ambient temperature on natural frequencies using a regression analysis. A 95% confidence interval was used to detect abnormal and damaged states. Whelan and Janoyan (2010) measured modal parameters of a damage induced steel girder bridge using bi-directional accelerometers. Kalman filters were used to investigate the correlation between baseline accelerations and the predicted responses to evaluate damage. It appeared that the modal

characteristics obtained from lateral accelerations were a better indicator for the simulated damage on the bridge than vertical accelerations, suggesting that torsional modes were better at describing damage states given the damage scenarios introduced in the study.

Modal strain energy is another parameter obtained from vibration-based monitoring systems and it has been found to be more sensitive to structural damage than natural frequency (Seo et al. 2016). Shi et al. (2000) proposed a modal strain energy change-based method for localizing damage that was able to localize and determine the magnitude of structural damage on a single-bay two-storey steel frame structure. Niu et al. (2015) presented a damage identification method coupled with modal strain energy for a steel girder bridge and found that the modal strain energy-based damage index was suitable for damage identification within the girders. While the strain energy-based damage detection algorithm has shown potential for locating damage through a vibration-based monitoring system, past studies focused on finite element simulations or small-scale testing. Therefore, there is a need to apply the strain energy-based damage detection algorithm to actual bridges under ambient traffic.

Another candidate for damage detection using a vibration-based monitoring system is using mode shape curvature. Guan et al. (2006, 2007) performed a modal analysis of the ambient vibrations on a two-span highway bridge to extract mode shape curvatures. Curvatures were found to be capable of detecting localized damage which appeared to have a relatively small effect on natural frequencies. Mode shape curvature was also used by Lee et al. (2007) to investigate the effects of externally bonded carbon fibre reinforced polymer on a deteriorated reinforced concrete bridge. Stiffness changes in the concrete deck were identified and located using damage indexes and fractional stiffness changes based on mode shape curvatures.

2.5.2   Strain-Based Structural Health Monitoring

Recent work has been done using the time-domain approach to incorporate strain measures. The basic principle of strain-based monitoring is that changes in physical properties cause changes in amplitudes of strain measurements. Analysis of time-domain strain measurements have been found to be effective in detecting and localizing damage. Wipf et al. (2007) used a network of fibre optic sensors to measure strain as a damage detection metric. The measured strains were used to find a relationship between sensors in undamaged regions and those in regions prone to fatigue damage. Lu et al. (2010) expanded on the work done by Wipf et al. (2007) to develop a statistical control chart that incorporated strain data residuals. When fatigue cracking occurred, the residuals shifted

from the baseline response to a point outside the control chart limits. Phares et al. (2013) performed field validation for the strain-based monitoring algorithm by installing two sacrificial specimens to simulate damage-sensitive locations on a bridge exposed to ambient traffic. Coupled with a statistical damage algorithm, the monitoring system identified damage using the strain data from the two specimens.

2.6   Analysis Methods

Modal identification methods can be classified as either Input-Output or Output-Output. Input-Output methods require both input force and response measurements, while Output-Output, also known as operational modal analysis (OMA), methods only require the response measurements of the structure in operational condition under ambient excitation. Finally, to validate field measurements various checks that compare measured modes to one another and/or to an analytical model should be incorporated. These include the Modal Assurance Criteria (MAC), orthogonality checks, or Coordinate Model Assurance Criterion (COMAC) (Chen and Ni, 2018).

Input-Output methods are focused on measuring the output response from a forced excitation where the exact input force is known. Common frequency domain methods for input-output methods include the Rational Fraction Polynomial (RFP) and Polyreference Frequency Domain (PRFD) (Chen and Ni, 2018).

Since it can be very difficult and costly to excite large civil structures, OMA methods are more popular in large structures since they only need to measure the response under ambient excitation (Peeters & De Roeck, 2001; Sun et al., 2017). OMA methods rely on the assumption that inputs are Gaussian white noise which is a valid assumption for many bridges due to the randomness of vehicle configurations (e.g., vehicle weights, axle configurations, vehicle suspensions) (Peeters & De Roeck, 2001; Sun et al., 2017; Ni et al., 2021; Yang et al., 2021). The peak-picking (PP) method is commonly used due to its simplicity. It relies on determining eigenfrequencies based on peaks found from a response spectrum (Chen and Ni, 2018).

Recent OMA methods include the eigensystem realization algorithm (ERA) and stochastic subspace identification (SSI) methods which are based on the state-space model. A drawback of these methods is the need to over specify the assumed model order in to capture all real structural modes. As a result, these methods tend to introduce spurious mathematical modes (i.e., modes that do not exist for the structure in reality) (Sun et al., 2017). Yang et al. (2021) noted the SSI method was reliable for analyzing modal parameters from ambient excitation but produced mainly

spurious modes for train loads (where the regularity of the load and axle spacing can no longer be assumed as random white noise). Yang et al. (2021) also extended a response-only deterministic SSI (DSSI) to effectively determine modal parameters given some known parameters of the train (e.g., train speed, carriage length, and axle spacing). Another OMA method tested on a cable-stayed bridge by Ni et al. (2021) is the fast Bayesian FFT method. The Bayesian FFT uses probabilistic logic to determine the most probable value of modal parameters. The method proposed by Ni et al. (2021) was used to effectively determine the effects of seasonal temperature changes on modal properties.

Various methods exist for comparing measured data with analytical or FE models for verification purposes. Modal Assurance Criteria (MAC), orthogonality checks, and coordinate model assurance criterion (COMAC). MAC has been widely used in recent studies (Peeters and Ventura 2002; Sun et al., 2017; Ye et al., 2020; Ni et al., 2021). MAC is essentially the squared correlation between two modal vectors and is used as a measure of similarity between modes. Values of MAC range from 0 to 1 with 1 indicating a high degree of similarity, and values below 0.8 indicating mode shapes deviate considerably (Peeters and Ventura 2002). MAC can be used to validate experimental modes by comparing with calculated modes, but several studies have also shown its effectiveness in filtering experimental mode shapes by comparing experimental modes with each other. Sun et al. (2017) developed a covariance driven SSI (SSICOV) using MAC as a criterion to eliminate spurious modes. In theory, real physical modes should have similar modal properties with modes at other system orders. Ni et al. (2021) used MAC for a similar purpose and found that while lower modes showed a higher similarity, a lack of similarity between higher modes indicated that more measurement locations are required to adequately capture the behavior of the higher modes.

2.7 Structural Health Monitoring Studies on Cable-stayed Bridges

Cable-stayed bridges are characterized by one or more stay cable towers and at least one forestay and one backstay. Examples of cable stayed bridges are shown in Figure 2.9. In a typical cable-stayed bridge, the stay cables have relatively steep inclination angles. The vertical reaction forces induced by the stay cables allow stay cables to be used in place of an intermediate support. The horizontal forces of the stay cables put the bridge deck into compression and act as an external post-tensioning force. These two factors combined allow cable-stayed bridges to reach long spans with relatively shallow superstructures. It is notable that in a cable-stayed bridge, the stays carry

most permanent loads and a significant portion of live loads (Collings and Gonzalez, 2013). In other words, the stays are responsible for most of the stiffness of the structure.

Figure 2.9.(a) Jindo Bridge, (b) Kap Shui Mun Bridge, (c) Ting Kau Bridge (Jang et al., 2010) (Wong, 2004)

Complex monitoring systems for damage detection have been used on cable-supported bridges worldwide. Li et al. (2006) developed a SHM system for the Shandong Binzhou Yellow River Highway Bridge to aid with bridge maintenance. A total of 141 sensors were used in conjunction with an automatically updated finite-element model (FEM), including fibre-bragg grated strain gauges, accelerometers, GPS, and anemoscopes. The objective of the monitoring system was to assess the structural health of the bridge, provide information for planning inspection and maintenance, and verify design assumptions to make recommendations for future cable-stayed bridge construction. They found that stay-cables are susceptible to fatigue and corrosion damage. Measured strain changed gradually to compression as trucks moved towards the tower which shows potential for strain measurement to estimate the vehicle location and weight. Li et al. (2006) also found that vehicle speed has little influence on cable vibration for the Shandong Binzhou Yellow River Bridge. Lin et al. (2018) used a FEM to plan and design a damage detection monitoring system on the Chaibu Bridge using a frequency response model, modal curvature algorithm, and data fusion techniques. A combination of accelerometers, fibre-optic distributed strain gauges, weigh-in-motion sensors, deflectometers, and GPS were proposed for the long-term monitoring of the bridge.

A wind and structural health monitoring system (WASHMS) was developed for three cable-supported bridges in China: the Tsing Ma (Suspension) Bridge, the Kap Shui Mun (Cable-stayed) Bridge, and the Ting Kau (Cable-stayed) Bridge) (Wong et al., 2000a; Wong et al., 2000b; Wong, 2004). Vehicle loads were monitored using weigh-in-motion sensors, railway loads were monitored using strain gauges, and seismic loads were monitored using three uniaxial accelerometers (Wong et al. 2000b). Bridge displacements were monitored using level sensing stations and via double integration of accelerometer measurements (Wong et al 2000a). Strain

gauges were also used to determine base-line references for damage detection. All measured load effects and responses were found to be well within the corresponding design limits.

2.8 Significance of the Tawatinâ Bridge

The Tawatinâ Bridge is a 3-span extradosed cable-stayed bridge in Edmonton, Alberta, Canada. The bridge carries light-rail vehicle (LRV) and pedestrian traffic over the North Saskatchewan River. Extradosed cable-stayed bridges have distinct characteristics from typical cable-stayed bridges. It is difficult to define exactly when a bridge becomes an extradosed bridge versus a cable-stayed bridge, but Collings and Gonzalez (2013) attempted to make the distinction. An extradosed bridge is a combination of a girder and a cable-stayed bridge (Figure 2.10). Extradosed bridges are characterized by a relatively short tower and shallower stay angles. The stays still allow for stay cables to be used in place of an intermediate support, allowing for longer spans. The shallower stays induce a larger horizontal force, and so the girders must be strong enough to withstand the axial forces (Guo et al., 2020). Because girder stiffness is significant compared to the stay cables, permanent loads are shared between the stays and the girder, and the girder carries most of the live load. Most studies on extradosed bridges focus on the longitudinal resonance characteristics, but few studies focus on the vibration characteristics of extradosed bridges under live load (Guo et al. 2020).
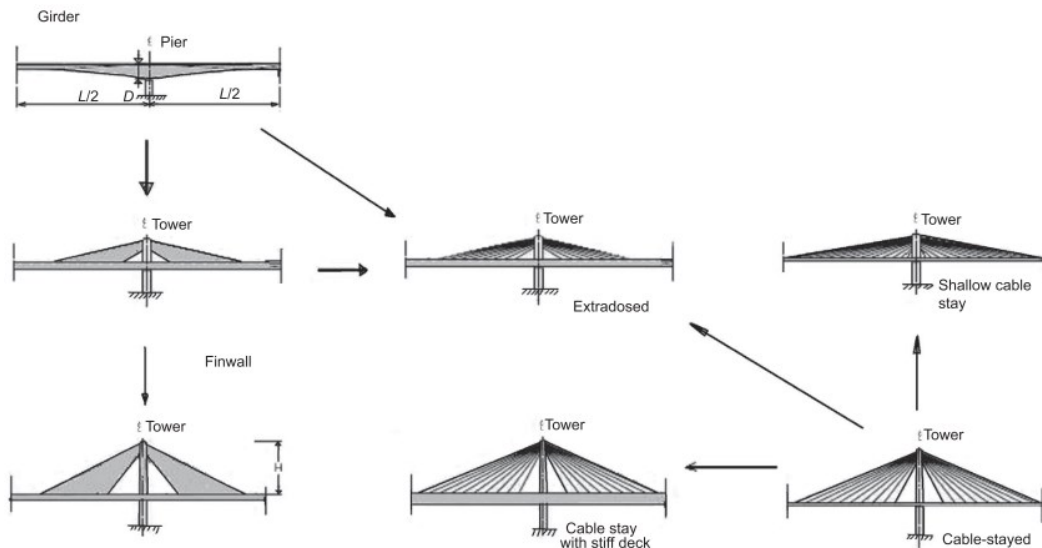
Figure 2.10. Typical Extradosed Bridge Arrangement (Collings and Gonzalez, 2013)

CHAPTER 3. METHODOLOGY

This study involves the use of accelerometers and strain gauges to perform structural health monitoring on the Tawatinâ Bridge. The goals of the study include examining the changes in modal frequencies during the construction of the shared-use-pathway (SUP) and to determine a baseline response for the completed bridge. An analytical model was also developed using CSiBridge to perform damage simulations and evaluate the effectiveness of modal identification methods for detecting various damage types.

3.1 Bridge Geometry

The Tawatinâ Bridge is a 3-span extradosed cable-stayed bridge that carries light-rail vehicle (LRV) traffic and pedestrian traffic, via a suspended SUP, over the North Saskatchewan River in Edmonton, Alberta, Canada. The two main spans are supported by 14 stay cables that run through an open shape bridge tower. The bridge deck is a post-tensioned 3.5 m tall by 11 m wide trapezoidal box girder (Figure 3.1). The SUP is 8 m wide and suspended by steel rods attached to the bottom of the box girder.

The bridge was constructed via segmental construction. The north main span is 100 m long with 20 segments: a 5.4 m segment adjacent to the stay tower, 17 equally spaced 5 m segments, a 4 m segment, and a 1 m closure segment. The south main span is 110 m long with 21 segments: a 5.4 m segment adjacent to the stay tower, 17 equally spaced 5 m segments, a 4 m segment, a 5 m segment, and a 1 m closure segment. The side span is a 50 m continuous box girder.

Figure 3.1. The Tawatinâ Bridge

3.2 Determining Sensor Layout

Sensor layouts are typically laid out based on an existing analytical model where the greatest deflections or vibrations are expected. For this study, sensor layouts were determined based on sensor placements of similar bridges found in the literature review since models and drawings were unavailable during the planning stages of this project. Theoretical bending moment diagrams of typical cable stayed bridges shown by Svensson (2013) were also used to understand the distribution of moments and determine potential critical areas. Locations were chosen to compare the behaviour between the first and last cable stays to infer the behaviour between cable stays. Another major consideration was sensor accessibility. Sensors had to be placed such that they could be easily accessed for data collection and troubleshooting purposes.

The selected sensor layout consists of four locations with three strain gauges and three accelerometers at each location (Figure 3.2). Accelerometers were placed on the bottom of the top slab and on the inside of the girder walls to capture vertical, transverse, and longitudinal accelerations. For simplicity, the bottom of the top slab will be referred to as the ceiling of the box girder, and the inside of the girder walls will be referred to as the east and west walls, accordingly. Strain gauges were added to estimate the relative load between accelerometer locations and provide further context for accelerometer readings. The use of the measurements to determine important parameters (e.g., load and natural frequencies) is discussed further in Section 3.4.

The type of monitoring system laid out in this chapter would be suitable for anomaly detection. Long term monitoring for anomaly detection is important for ruling out any false positives due to non-anomaly events, such as the effects of weather at different times of the year (La Mazza et al. 2023). As discussed in Section 2.3, anomaly detection systems differ from damage detection systems since they (anomaly detection systems) are only able to detect the presence of potential damage, but not locate or measure the extent of the damage. However, the presence of an anomaly can prompt asset owners to investigate and perform the appropriate corrective actions.
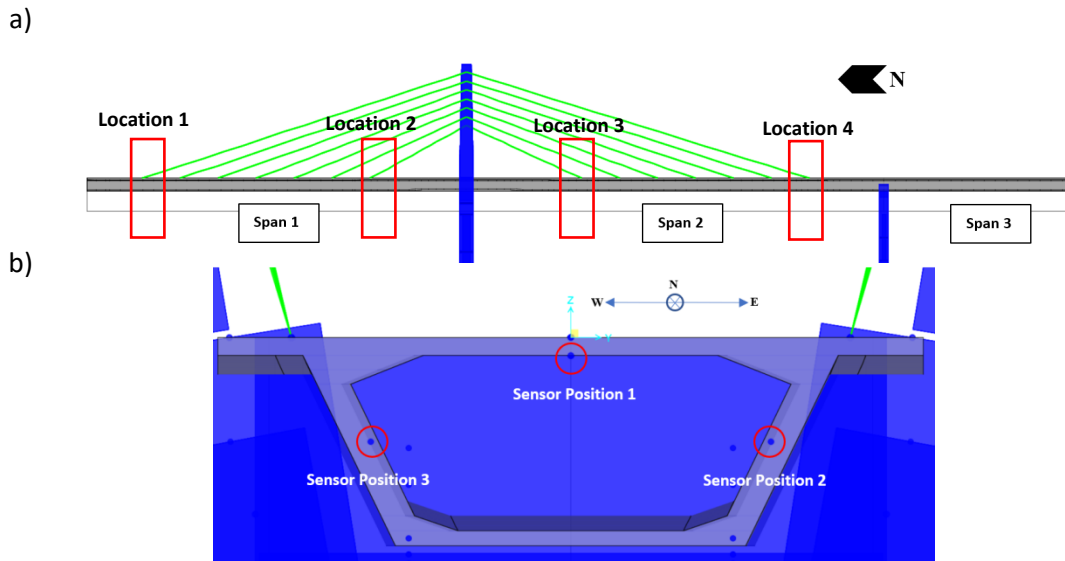
Figure 3.2. (a) Sensor locations on elevation view (b) Sensor positions cross-sectional view.

3.2.1 Limitations

Challenges related to the COVID-19 pandemic and working in an active construction site were present in the deployment, operation, and data collection of the sensors. Governments introduced restrictions such as limited capacity and physical distancing minimums for workers on site during the pandemic. Access to the inside of the bridge girder also required additional coordination to avoid interfering with construction activities. Together, these requirements limited the number of site visits possible and the duration of each visit. Additionally, strain gauges were damaged due to construction activity on the bridge and could not be reinstalled due to the time restrictions for site visits.

3.3 Instrumentation

3.3.1 Strain Measurement

As noted in Section 3.2.1, strain gauges were damaged during construction and not used for analysis. However, strain gauges are still discussed in this chapter for information purposes.

Foil strain gauges are the most common instrument for strain measurement (Xu and Xia, 2012). They consist of a metallic foil supported by a thin backing and are attached to testing surfaces using adhesives. Foil strain gauges are an economical and effective solution for measuring dynamic strains. Depending on the application, foil strain gauges can range from a few millimetres to centimetres in length (Xu and Xia, 2012). Foil strain gauges were chosen for this project due to

availability, ease of installation, and a focus on dynamic strain. A general rule of thumb for sizing strain gauges for concrete is select gauges with gauge lengths greater than twice the concrete aggregate size. This provides sufficient averaging of the concrete strain since concrete is a nonhomogeneous material. As a result, a gauge length of 60 mm was selected.

3.3.2 G-Link-200

The G-Link-200 (Figure 3.3) is a wireless accelerometer node with an integrated three-channel triaxial microelectromechanical system (MEMS) accelerometer. It includes a measurement range of up to $8g$ and a sampling rate of up to 4096 Hz. The G-Link-200 is capable of three sampling modes: continuous, periodic burst, and event triggered. The periodic burst and event triggered sampling modes require a gateway within range of the nodes to act as a beacon for synchronizing measurements. Onboard memory on the G-Link-200 allows datalogging of up to 8,000,000 datapoints. Table 3-1 shows the maximum sampling duration for datalogging continuous measurements on the G-Link-200. Triaxial accelerometers were chosen to capture accelerations in all directions since vertical and lateral movement was expected. In addition, the protective housing of the G-Link-200 provides protection from construction debris such as concrete dust and grout along with moisture.
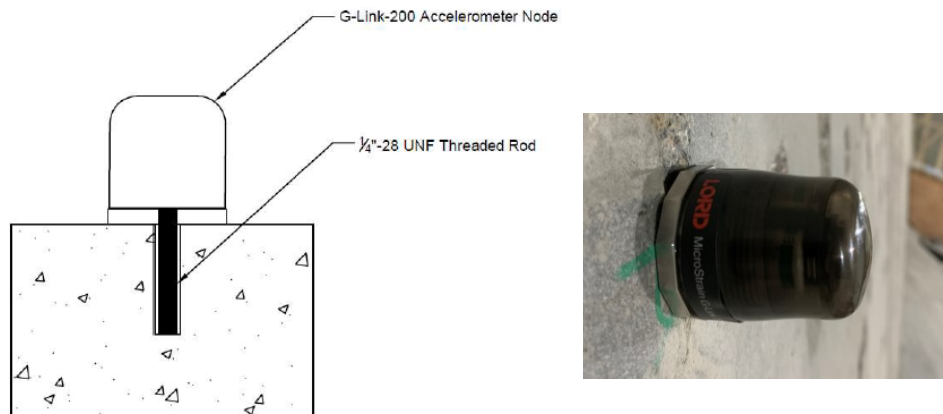
Figure 3.3. G-Link-200 installation assembly

Table 3.1. Maximum sampling ratio for continuous measurements given 16Mb onboard memory.

Sampling Rate (Hz)	Maximum Duration (hrs)
64	34.7
32	69.4
16	138.9

25

3.3.3   Installation

Figure 3.3 shows the installation assembly for the G-Link-200, and Figure 3.4 shows the positions of the sensors. For vibration measurements, it is important that a rigid connection is made between the G-Link-200 and the concrete. A non-rigid connection (e.g., a weak adhesive) could cause excessive damping between the concrete and the sensor which increases measurement noise and makes it difficult to accurately capture the response of the concrete. A 45 mm long, 6.3 mm diameter-28 Unified National Fine (UNF) threaded rod was used to anchor the G-Link-200 into the concrete by drilling a 9.5 mm diameter hole 40 mm into the concrete surface and using PL Premium MAX construction adhesive. The depth was chosen to provide sufficient anchorage while not exceeding cover requirements (specified as 50 mm in the construction drawings). The vertical and longitudinal axes of the nodes (lateral and longitudinal for accelerometers on the ceiling of the girder) were aligned to the concrete surface using a hand level.

Figure 3.4. G-Link-200 (circled for emphasis) installed inside box girder

3.4   Data Collection

Two wireless gateways from LORD MicroStrain were considered for data collection. The WSDA-2000 is a network connected wireless gateway capable of collecting data remotely and uploading to SensorCloud (LORD's cloud storage system). The other device considered was the WSDA-200-USB which is a USB gateway that requires a host computer to collect data. Due to the

requirement for a power source, the WSDA-2000 was not chosen as a consistent power source could not be guaranteed during and after construction.

With the WSDA-200-USB (the gateway), data must be collected in-person on site. The theoretical wireless range is 400 m, but the actual range for the gateway inside of the girder was closer to 40 m as the gateway could not connect to sensors past this distance. While on the bridge deck, the gateway was unable to obtain a signal from the accelerometers inside the girder likely due to the very dense steel reinforcement in the bridge interfering with the signal. The same was found when trying to connect to sensors on the opposite span of the gateway, likely due to interference from reinforcement in the bridge tower

Due to the constraints described above, it was not practical to have a permanent gateway installed on site, therefore periodic burst and event triggered measurements were not possible. The use of multiple permanent gateways installed along the bridge may have been able to resolve the above constraints but was decided against due to budget constraints. Continuous measurement was attempted over a period of three days, however the total time to collect the logged data exceeded the allowable time for site visits. As a result, measurements and data collection were performed with weekly site visits throughout construction of the SUP. Two to three samples were taken each visit. Sampling rate and duration were determined using a trial-and-error approach based on where peaks were found in the response spectrum. The resolution of the frequency range, Δf, was found using Equation 3.1 where N is the number of points in the acquired time-domain signal, and Δt is the sampling period (National Instruments, 2000). Table 3-2 summarizes the sampling rates, duration, and resolution on site visits where ambient response data was collected.

$$\Delta f = \frac{1}{N * \Delta t} \tag{3.1}$$

Table 3.2. Sampling information and response resolution for ambient data collection

Date	Sampling Rate (Hz)	Length (# datapoints)	Δf (Hz)
29/06/2021	64	512	0.125
20/07/2021	64	512	0.125
23/09/2021	64	512	0.125
30/09/2021	64	512	0.125
07/10/2021	64	512	0.125
29/10/2021	64	512	0.125
04/11/2021	64	512	0.125

3.5 Data Analysis

The data from accelerometers is collected as time-domain data and converted to the frequency domain to determine the modal frequencies and other modal parameters. A preliminary peak-picking analysis is conducted using a fast-Fourier transform (FFT). More complex analysis is conducted using a Covariance-Driven Stochastic Subspace Integration (SSI-Cov) method developed by Cheynet (2020). Mode shapes determined by the three methods are further processed using the modal assurance criterion for further verification. The methods above and their applications are discussed in detail in the following sub-sections.

3.5.1 Fast-Fourier Transform

The time-domain data was downloaded directly from SensorConnect and processed using a combination of Excel and Matlab. A Matlab script was written to apply windowing functions and perform a Fast-Fourier Transform (FFT) to obtain the frequency spectra. Built-in functions were used to apply windows and perform FFT. It is important to account for aliasing and spectral leakage when applying FFTs. Aliasing is the folding of higher frequencies about the Nyquist frequency (half of the sampling rate) and can be accounted for by increasing the sampling rate. The sampling rate should be at least double the frequency of interest. Spectral leakage occurs when a time-period sample contains a non-integer number of periods. The resulting spectrum is "smeared" by artificial discontinuities which show as high-frequency components that are not present in the actual signal (National Instruments, N.D.). Windowing functions reduce the effects of spectral leakage by forcing data to be periodic.

3.5.2 Windowing Functions

Many windowing functions exist and are typically chosen based on the signal content. Since this study focuses on ambient excitations, the signal contents were expected to be random noise. The Hanning window, Hamming window, and Blackman window were considered for their side lobe compression. Figure 3.5 shows a comparison of the three window functions applied to a sample of ambient data. For the sample shown, a distinct peak is visible using the un-windowed data. The window functions reduce the density and amplitude of the signal noise. There is a notable decrease in the amplitude of the peak of the spectra after applying the windowing functions, but this is unimportant since the primary concern is the frequency at which the peak occurs. In some datasets, applying the window functions reduced the amplitude of false peaks appearing in the un-windowed data such that they were indistinguishable from noise. It was not immediately obvious which

window function was qualitatively the best for our application, but the Blackman window was chosen due to its slightly better ability to reduce the noise density. This is consistent with the comparison performed by Podder et al. (2014) which showed the Blackman function was better than the Hamming and Hanning windows for reducing side lobes.
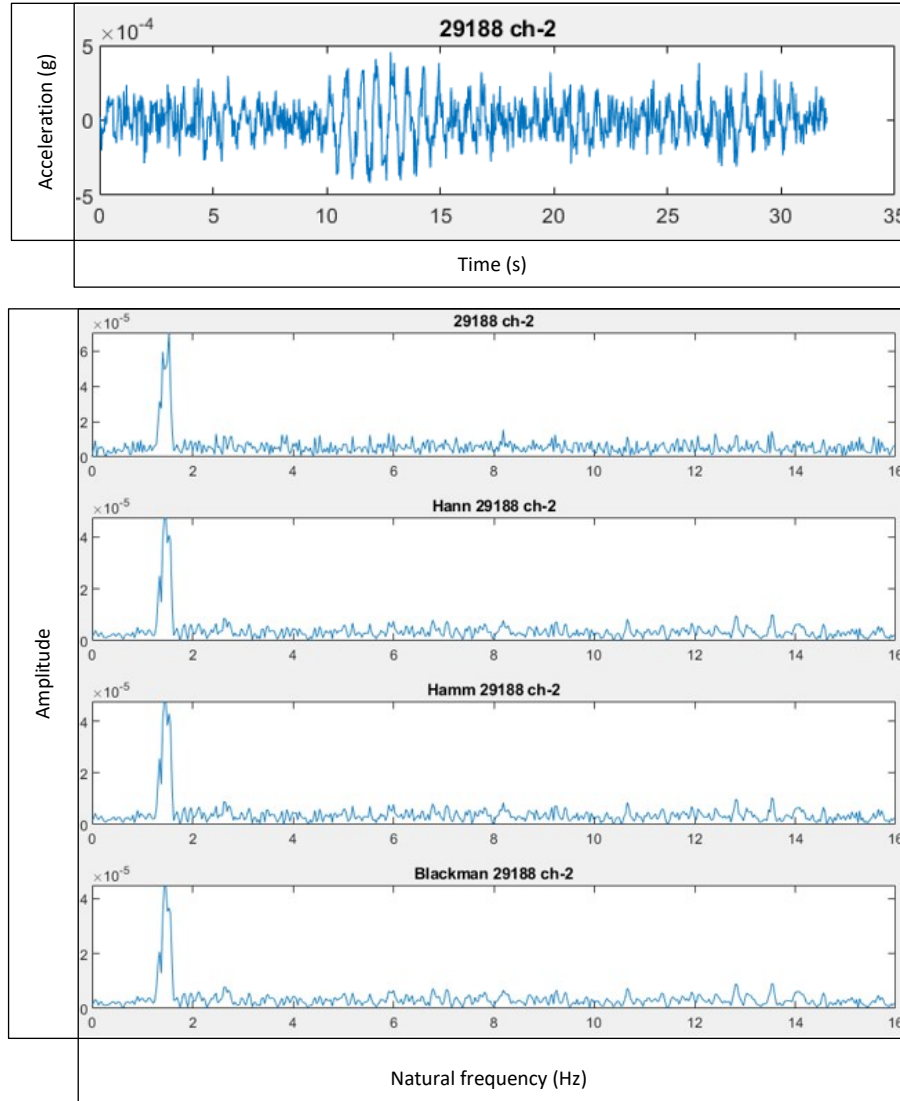
Figure 3.5. Sample comparison of different windowing functions.

3.5.3   Covariance-Driven Stochastic Subspace Integration

Cheynet (2020) developed a covariance-driven stochastic subspace integration (SSI-Cov) MATLAB script based on a paper by Magalhaes et al. (2009). The algorithm is paired with a hierarchical clustering algorithm (Yonggang, 2021; Ogier, 2021) to automatically analyse stabilization diagrams and identify spurious modes (mathematical modes which have little to no

physical relevance). Another common stochastic subspace integration method is the data-driven stochastic subspace integration (SSI-Data) which differs from the SSI-Cov method by projecting future data rather than calculating covariances to mitigate the effects of signal noise. Both have been found to perform similarly, but the SSI-Cov is computationally faster and more commonly used in OMA applications (Zahid et al. 2020). SSI-Cov has been successfully applied in various cases for measuring modal properties of structures under ambient loading (Magalhaes et al., 2009; Cheynet et al., 2016; Cheynet et al., 2017). The SSI-Cov method is described in detail by Magalhaes et al. (2010), but the key parameters are summarized in the following.

The equilibrium of a complex dynamic system with a finite number of degrees of freedom is represented by the equation of motion (EOM) in matrix form:

$$M\ddot{q}(t) + C_1\dot{q}(t) + Kq(t) = p(t) = B_2 u(t) \tag{3.2}$$

where M, C_1, and K are the mass, damping, and stiffness matrices, respectively, and $\ddot{q}(t)$, $\dot{q}(t)$, and $q(t)$ are column vectors which represent time functions of the acceleration, velocity, and displacement, respectively, of each degree of freedom. The term $p(t)$ represents a column vector with the forces applied to the system.

The second-order EOM (Equation 3.2) is transformed into a first-order system using mathematical manipulations to obtain the state equation (Equation 3.3a). By including the observation equation describing the observed acceleration responses (Equation 3.3b), the state-space model can be obtained as follows:

$$\dot{x}(t) = A_c x(t) + B_c u(t) \tag{3.3a}$$

$$y(t) = C_c x(t) + D_c u(t) \tag{3.3b}$$

where A_c is the state matrix, $x(t)$ is the state vector containing the displacements of the system, and $\dot{x}(t)$ is the state vector containing the velocities of the system. The observed acceleration vector is represented by $y(t)$, $u(t)$ is a vector containing the dynamic system inputs, C_c is the output matrix, and D_c is the designated direct transmission matrix. The eigenvectors and eigenvalues of A_c represent the modal parameters of the system.

In the context of operational modal analysis, system input is unknown, therefore the terms of the dynamic system inputs are represented by stochastic components, and the time functions are replaced by discrete-time variables. Therefore, the state-space model becomes:

$$x_{k+1} = Ax_k + w_k$$
$$y_k = Cx_k + v_k \qquad (3.4)$$

It can be shown that the eigenvectors of A coincide with those of A_c, providing a means of measuring the modal parameters using observed data. The correlation matrix is given by:

$$R_j = CA^{j-1}G \qquad (3.5)$$

where R_j is the correlation matrix of the outputs for an arbitrary time lag $\tau = j\Delta t$ and G is the "next state-output" correlation matrix defined as

$$G = E[x_{k+1}y_k^T] \qquad (3.6)$$

The SSI-Cov method identifies a stochastic state-space model from the output covariance matrix by first building a block Toeplitz matrix with the output correlation matrices evaluated at various positive time lags. A singular value decomposition (SVD) is applied to the Toeplitz matrix to derive the state-space model which is then used to obtain the modal parameters of the system.

To measure all the possible modes within a given frequency range, the SSI-Cov method requires estimating an upper limit of modes much greater than the number of physical modes within that frequency range. This helps to minimize the impact of noise, but the high model orders lead to the introduction of spurious modes. A popular approach for identifying and eliminating spurious modes is through the creation and evaluation of stabilization diagrams (Magalhaes et al. 2010).

3.5.4   Modal Assurance Criteria (MAC)

The MAC (Equation 3.7) was used to eliminate spurious modes and cluster similar modes in both the SSI-Cov and Bayesian FFT procedures. This application of the MAC allows the comparison of experimental data with calculated data. MAC values range from 0 to 1 with 1 indicating a high degree of similarity. The similarity between mode shapes ϕ_j and ϕ_k, where the $\{\phi_j\}^H$ denotes the Hermitian of ϕ_j is calculated as

$$MAC(\phi_j, \phi_k) = \frac{\left|\{\phi_j\}^H\{\phi_k\}\right|^2}{(\{\phi_j\}^H\{\phi_j\})(\{\phi_k\}^H\{\phi_k\})} \qquad (3.7)$$

3.5.5   Strain Measurements

As noted in Sections 3.2.1 and 3.3.1, strain gauges were damaged during installation. However, it is still relevant to discuss the potential uses of strain gauge data. From basic engineering materials

principles, it is known that stress (σ), strain (ε), and the modulus of elasticity (E) follow the relationship shown in Equation 3.8 while the material remains linear, expected for the bridge under service loading conditions. Since force is equal to stress times area, there is a direct relationship between force and strain. Various studies have used strain as a damage detection metric (see Section 2.5.2).

$$E = \frac{\sigma}{\varepsilon} \tag{3.8}$$

3.5.6 Displacements

Displacements can be estimated by applying a centred finite difference (CFD) scheme. Since acceleration is the second derivative of displacement, the accelerometer data can be double integrated using the CFD scheme shown in Equation 3.9 to calculate relative deflections. In lieu of strain gauges, the relative deflections can provide information on the movements experienced by the bridge (e.g., vertical movements, lateral movements, or longitudinal movements). Where t denotes the current time-step and $h = \Delta t$ denotes the time increments, the relative deflection is calculated as

$$x''(t) \approx \frac{f(t+h) - 2f(t) + f(t-h)}{h^2} \tag{3.9}$$

Since the focus of this study was to determine the mode shapes of the bridge based on vibration measurements, this method was not used.

3.5.7 Signal-to-Noise Ratio

The signal to noise ratio (SNR) (Equation 3.10a) in simplest terms is the ratio of the power of the desired signal to the power of the noise within the same bandwidth and can be used to quantify the strength of the signal or the amount of noise in a sample. The SNR is often expressed in decibels (Equation 3.10b). A SNR of 1 (or 0 dB) is undesirable and indicates the signal is buried in noise.

$$SNR = \frac{P_{signal}}{P_{noise}} \tag{3.10a}$$

$$SNR_{dB} = 10 \log_{10}(SNR) \tag{3.10b}$$

3.6 Development of Analytical Model

A 3-D analytical model of the Tawatinâ Bridge was developed from scratch using CSiBridge v21.2.0 Advanced with Rating (Figure 3.6). CSiBridge was chosen because it is commonly used in engineering practice and understood bridge engineers. It has been used effectively in previous

research programs at the U of A (De Laurentiis, 2015), and is more computationally efficient for the purposes of this study compared to finite-element-analysis (FEA) software such as ABAQUS. The model geometry and material properties were based on issued-for-construction (IFC) drawings of the bridge. The components of the bridge can be split into five main structural groups: the box girder, the stay tower, the stay cables, the prestressing tendons, and the SUP. For simplicity, the SUP was not included in the analytical model. Caution must be taken when drawing conclusions on the real structure based on this model. The IFC drawings provide nominal values and are not representative of the material properties of the actual bridge. Model updating techniques, including updating the model with the material properties measured in the field, would improve the accuracy of the model but are outside the scope of this research.
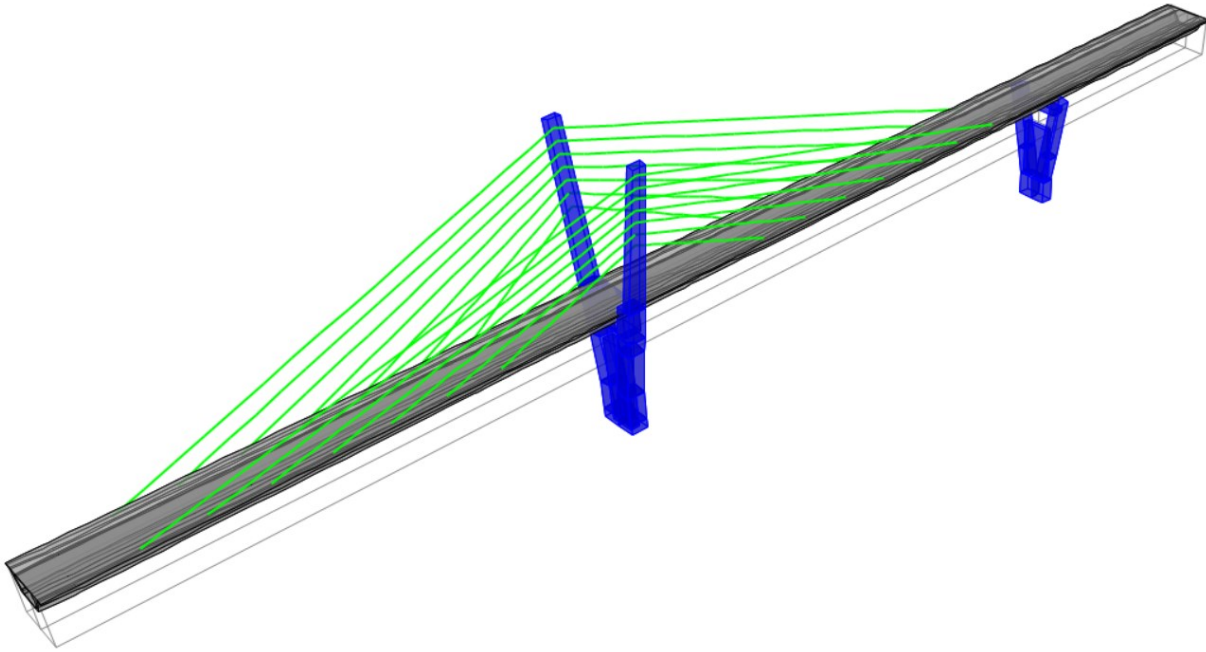
Figure 3.6. CSiBridge analytical model (extruded view)

The material properties for the concrete, stay cables, and prestressing tendons were taken from the IFC drawings and discussed in Sections 3.6.1, 3.6.2, and 3.6.3, respectively. For simplicity, non-prestressed reinforcement was not accounted for. Young's modulus of the concrete was estimated using the CSA S6-19 code (Equation 3.11), and all concrete components of the bridge are cast-in-place.

$$E_{c,28} = \left(3300\sqrt{f_c'} + 6900\right)\left(\frac{\gamma_c}{2300}\right)^{1.5} \tag{3.11}$$

where $E_{c,28}$ is the characteristic value of the modulus of elasticity, f_c' is the specified 28-day compressive strength of concrete, and γ_c is the mass density of concrete in kg/m³.

3.6.1 Box Girder and Stay Tower

The box girder was modeled as a concrete box girder deck section with 50 MPa concrete. The stay tower was modeled with two sets of five frame objects (one set each for East and West) with 35 MPa concrete and connected with rigid links for simplicity (see Figure 3.7). As the superstructure was the focus of this study, the piles and ground interaction were not modeled, and the bottom of the stay tower was fixed (i.e., fully restrained from translation and rotation).
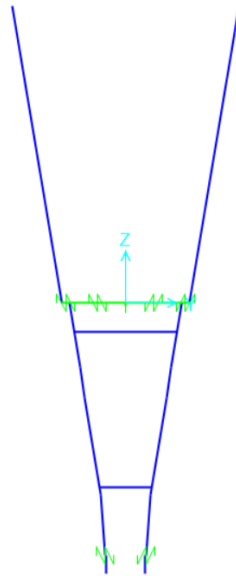
Figure 3.7. Stay tower (pier 1) analytical model showing rigid links and frame objects

Table 3.3. Concrete properties

Component	28-Day Strength (MPa)	Density (kN/m³)	Young's Modulus (GPa)	Exposure Class
Girders	50	24.5	34.2	S-3
Piers, Abutments, Pile Caps, SUP Infill	35	24.5	29.9	XD2
Piles	35	24.5	29.9	XD2

3.6.2 Stay Cables

Each stay cable consists of 40 seven-wire strand bundles which conform to ASTM A416 Low Relaxation steel. The stays were modelled as line objects using undeformed geometry and assuming zero sag for simplicity. Tension was applied at the ends of the cable attached to the deck

to mimic the real-life tensioning procedure and end-of-construction tension forces were used as per the IFC drawings (Table 3-4).

Table 3.4. Stay cable properties

Nominal Diameter	15.75 mm
Nominal Steel Area	149.2 mm^2
Nominal Ultimate Tensile Strength	1860 MPa
Guaranteed Nominal Breaking Load	260.7 kN
Young's Modulus	195,000 MPa
Relaxation (1000 hrs/70% UTS)	2.50%

3.6.3 Post-tensioning Tendons

Each tendon was modelled with interconnected line objects to match the geometry of the actual tendons. The girder contains cantilever tendons to counteract the negative bending moments at Pier 1 during the segmental construction of Span 1 and Span 2. Draped tendons are used to counteract the positive bending at midspan and negative moments at Pier 1 and Pier 2. Additional tendons include soffit tendons and deck tendons. Figure 3.8 shows the tendons in the analytical model and Table 3-5 shows the prestressing tendon properties. CSiBridge accounts for prestress losses using default factors shown in Figure 3.9.
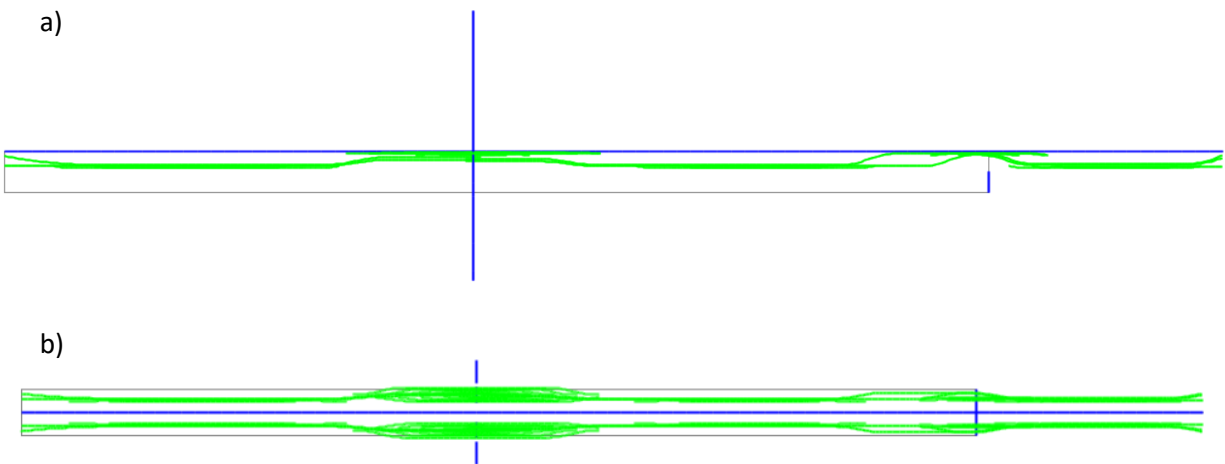
Figure 3.8. Post-tensioning tendons (shown in green): elevation view (a), and profile view (b)

Table 3.5. Prestressing tendon properties

Nominal Stand Diameter	15.24 mm
Nominal Steel Area per Strand	140 mm2
Nominal Ultimate Tensile Strength	1860 MPa
Guaranteed Nominal Breaking Load	260.7 kN
Young's Modulus	195,000 MPa
Relaxation (1000 hrs/70% UTS)	2.50%
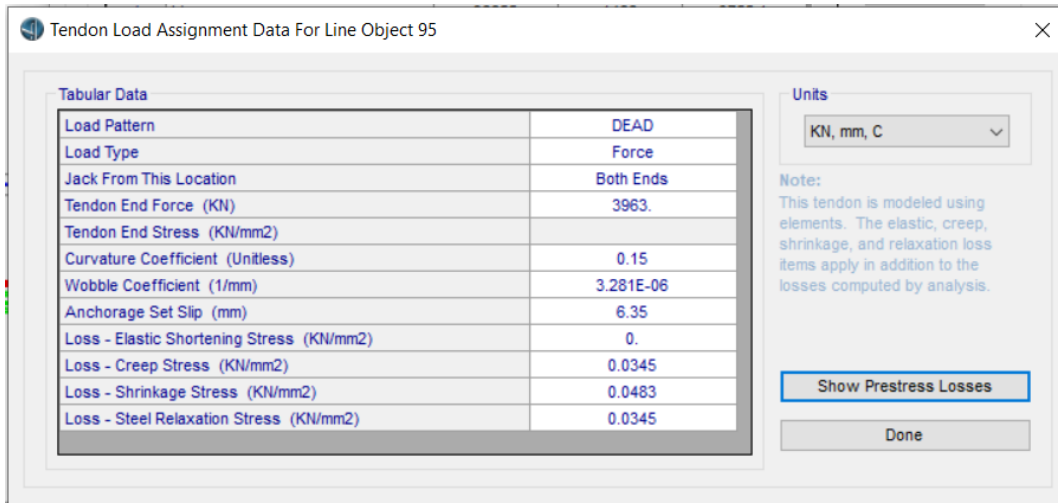
Figure 3.9. Sample tendon loads and default loss coefficients

3.6.4 Geometry

Information from Section 3.1 is repeated here for convenience. The box girder is split into two main spans and one side span. The north main span is 100 m long with 20 segments: a 5.4 m segment adjacent to the stay tower, 17 equally spaced 5 m segments, a 4 m segment, and a 1 m closure segment. The south main span is 110 m long with 21 segments: a 5.4 m segment adjacent to the stay tower, 17 equally spaced 5 m segments, a 4 m segment, a 5 m segment, and a 1 m closure segment. The side span is a 50 m continuous box girder.

The thickness of the bottom mat of the box girder is thickest for the two segments adjacent to the stay tower and then consistent throughout the rest of the girder. The variation was captured in the CSiBridge model using linear variations.

3.6.5 Bearings and Abutments

Relevant restraints were applied to the support locations to represent the actual supports on the bridge. The north abutment, Pier 2, and end of Span 3 were modeled as roller connections (restrained against vertical and lateral displacements) to represent the guided pot bearing supports. The girder is continuous and cast monolithically with the stay tower (Pier 1). This interaction was modeled as a rigid link connecting the girder and the stay tower to simulate a continuous fixed support.

3.6.6 Traffic Lanes

Lanes for dynamic vehicle loading were defined based on the dynamic envelope from the IFC drawings (Figure 3.10). The lanes are 3,420 mm wide and offset 2,250 mm from the centre of the

deck. For simplicity, the deck was modeled flat (without plinths), and the bridge-railway interaction was not considered. Including the bridge-railway interaction would add additional degrees of freedom and would allow for a more detailed analysis that accounts for the flexibility of railway components (Zhai et al., 2019). However, this level of detail is outside the scope of this study.
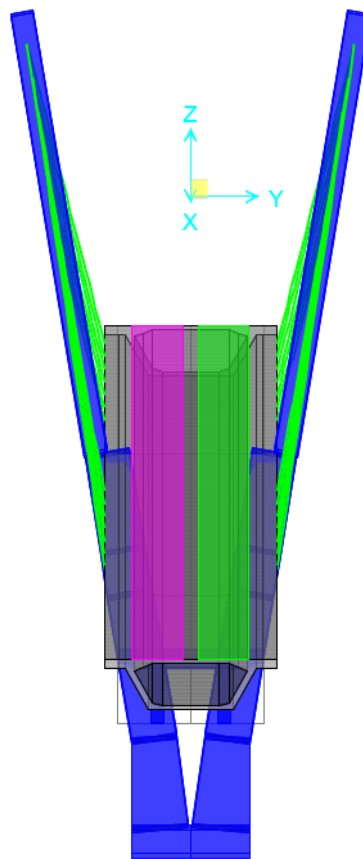
Figure 3.10. Lane definitions

3.7   Damage Simulation

To understand the effects of structural damage on the modal properties of the bridge, damage was simulated to various components of the bridge by manipulating the flexural stiffness of those components. The damage scenarios considered are bearing damage, cable damage, deterioration of specific segments, and post-tensioning tendon damage. Once damage was applied, a static modal analysis and a few dynamic tests were performed. Static modal analysis was performed to determine the change in natural frequencies and mode shapes of the various damage scenarios. Vehicle testing was conducted to predict the potential excitation that the bridge would experience

in response to train loads in service and how different damage scenarios affect that excitation. Figure 3.11 summarizes the damage scenarios considered.

Bearing damage was simulated by changing the pinned and roller supports to fixed supports (i.e., restraining rotation and displacement in all directions). Increasing the support stiffness is meant to simulate damage from debris obstructing the bearings and weakening of the elastomeric pads.

Stay cable damage was simulated by decreasing the stiffness of each pair of cables by 25%, and 75%. Damage to cables can occur from fatigue over time by the constant running of trains and pedestrians, or corrosion which can occur if the protective sheathing wears over time and allows water to penetrate to the steel strands. Damage was also applied to each pair of cables to determine which pair of cables affect the modal properties the most.

Stiffness reductions were applied to simulate damage to the segments (NP1 and SP1) adjacent to the stay tower (Pier 1). Damage to the concrete can occur from crack propagation or corrosion of reinforcing steel. From basic structural analysis, fixed supports also experience large shear forces and negative bending moments which show the importance of these segments. Stiffness reductions were applied at 25% and 75%.
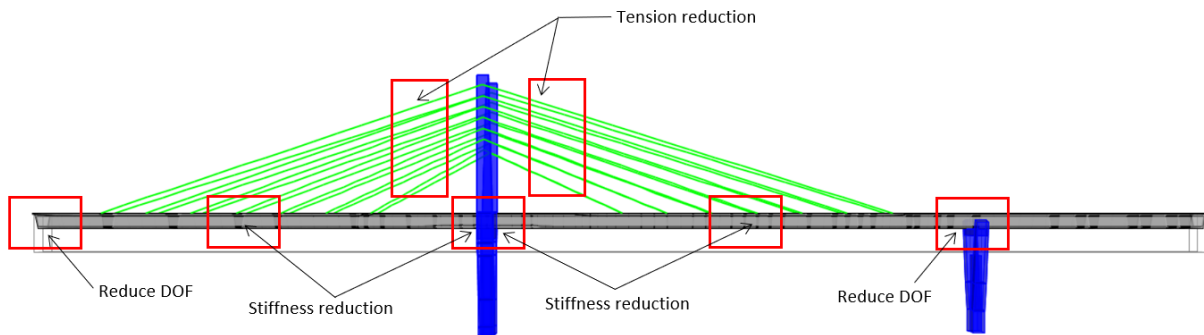
Figure 3.11. Damage simulation plan

3.8 Chapter Summary

This chapter discussed the methodology for performing the vibration-based monitoring of the Tawatinâ Bridge, including collection of field data and damage simulation using an analytical model. The objectives of the study and a detailed overview of the bridge structure were presented.

The proposed sensor layout for the bridge consists of four sensor locations with three accelerometers and three strain gauges at each location. Limitations present during sensor deployment and data collection were discussed. Due to strain gauges being damage from construction activities, data collection and analysis focused on vibration-based monitoring. A comparison of windowing functions was performed, and the Blackman window was chosen to filter acceleration data. FFT, SSI-Cov, and MAC were all discussed as each will be used for determining the modal properties of the bridge.

The geometry of the existing bridge and development of the analytical model using CSiBridge were also provided in detail. The components of the bridge were split into five main structural groups (box girder, stay tower, stay cables, prestressing tendons, and the SUP), and the assumptions for modeling each group were discussed. For simplicity, the SUP was not included in the analytical model. Additionally, the damage cases to be considered, and the methodology for simulating damage to the different structural components was discussed. Damage was simulated on the CsiBridge model to the bearings, stay cables, girder, and post-tensioning tendons using a combination of stiffness and tension reductions.

Chapter 4 discusses the results of the ambient and dynamic testing on the Tawatinâ Bridge where the modal parameters are determined using the methods discussed in this chapter. Chapters 5 and 6 both discuss the damage simulation performed using the analytical model. An analytical model developed using CsiBridge is analyzed using an eigenvector analysis in Chapter 5 to determine the possible mode shapes of the bridge. Chapter 6 discusses the analysis of the same model using a linear modal time history analysis to collect acceleration data from a simulated train load and determine the mode shapes using the methods used in this chapter.

CHAPTER 4.   ANALYSIS OF FIELD DATA

This chapter discusses the modal analysis of the accelerometer data obtained from the Tawatinâ bridge. Accelerations were collected in the vertical, transverse, and longitudinal direction for both ambient and dynamic excitation events from 12 triaxial accelerometers. Ambient data was taken during construction of the shared-use-pathway (SUP) with workers present on the site while the dynamic data was taken during dynamic testing of the SUP. Modal properties were calculated using a covariance-driven stochastic subspace integration (SSI-Cov) MATLAB script developed by Cheynet (2020). The goal of this analysis is to establish a framework for measuring a baseline response which can be compared with future bridge responses to detect potential damage. The effects of different damage types on the modal properties of the bridge are discussed further in Chapter 5 and Chapter 6.

4.1   Sensor Layout

The sensor layout is discussed in detail in Chapter 3 and summarized here for convenience. Triaxial accelerometers were installed at four locations along the two largest spans of the bridge inside of the concrete box girder. Three accelerometers were installed at each location: at the bottom of the top slab, and at mid-height of each girder wall. Each accelerometer captures vertical, transverse, and longitudinal accelerations and were positioned with the intent to also detect torsional movements. Figure 4.1a shows the sensor locations on an elevation view of the bridge and Figure 4.1b shows the positions of the sensors at each cross-section.
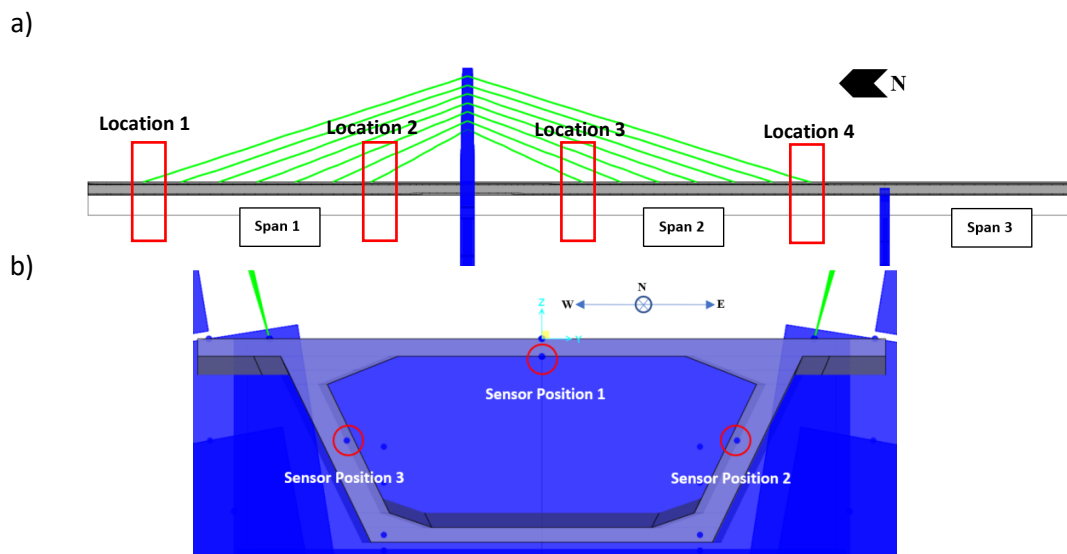
Figure 4.1. (a) Sensor locations in elevation view; (b) Sensor positions in cross-sectional view.

4.2 Ambient Excitation

The methodology for data collection was discussed in detail in Chapter 3 and summarized here for convenience. Ambient excitation data was collected during the construction of the shared-use pathway over 10 site visits. Data could only be recorded for one span at a time because interference from the reinforcing steel in the stay tower reduced the range of the gateway node for data collection. Therefore, data could only be synced for accelerometers on the same span and mode shapes could only be estimated for each span individually. Data was filtered using a Blackman window Hanning and Hamming windows were also considered, but the Blackman window was found to be better at reducing noise density. Preliminary analysis was performed using a Peak-Picking Fast-Fourier Transform (FFT) to determine possible natural frequencies for the bridge and a more detailed analysis was performed using the SSI-Cov MATLAB script to find various modal properties of the bridge. Sampling rate and sample lengths were determined using a trial-and-error approach to improve the Fourier Transform resolution. Multiple samples were taken at each span to account for potential data loss and/or connection issues for each sample. As a result, the sampling rate and duration were ultimately dictated by the length of each site visit. Measuring at 64 Hz with 512 datapoints was found to be an adequate compromise for collecting data under time constraints and connection issues sometimes faced with the USB gateway when collecting long samples. These issues could be resolved by using permanently installed data acquisition units with network capabilities. Table 4-1 summarizes the sampling information for each site visit.

Table 4.1. Sampling information and response resoluton for ambient data collection

Date	Sampling Rate (Hz)	Length (# datapoints)	Resolution (Hz)
29/06/2021	64	512	0.125
20/07/2021	64	512	0.125
23/09/2021	64	512	0.125
30/09/2021	64	512	0.125
07/10/2021	64	512	0.125
21/10/2021	32	512	0.0625
29/10/2021	64	512	0.125
04/11/2021	64	512	0.125
12/11/2021	32	1024	0.0312
19/11/2021	32	1024	0.0312

4.2.1 Preliminary Analysis with FFT

Figure 4.2 shows a sample taken on November 4, 2021, from the Location 4, Position 1 sensor in the U3 (vertical), U2 (transverse), and U1 (longitudinal) directions. This sample shows a typical

result where peaks are evident, but there is still considerable noise in the FFT plot. FFT results of the sample show a prominent peak in the U3 direction and a notable peak in the U1 direction while the U2 direction shows less prominent peaks. The results in the U2 direction indicate that there may have been a lot of noise in the collected sample, and/or the ambient loads did not excite the structure in that direction. In general, data collected in the U1 and U2 directions tended to have more noise, with SNRs of approximately 3.5 dB and 1.2 dB respectively, while the data collected in the U3 direction showed more prominent peaks with a SNR of approximately 10 dB, although many samples still contained noise. Natural frequencies in the vertical direction may have been easier to detect due to the presence of workers on the deck and SUP which applied enough acceleration in the U3 direction to reduce the effect of noise.

An issue that can arise with vibration-based monitoring systems, particularly when there is construction activity, is that sensors may pick up vibrations from external sources and create false readings. Figure 4.3 shows a sample that likely measured vibration from power tools. The acceleration response in the U3 direction appears to have a very uniform period, and FFT results show prominent peaks with relatively high magnitude. Samples such as these could result from power tools (e.g., impact drills) being used in the vicinity of the accelerometers and are likely not measuring the actual response of the bridge. Hence, samples such as these should be rejected as they are not useful for establishing a baseline response.
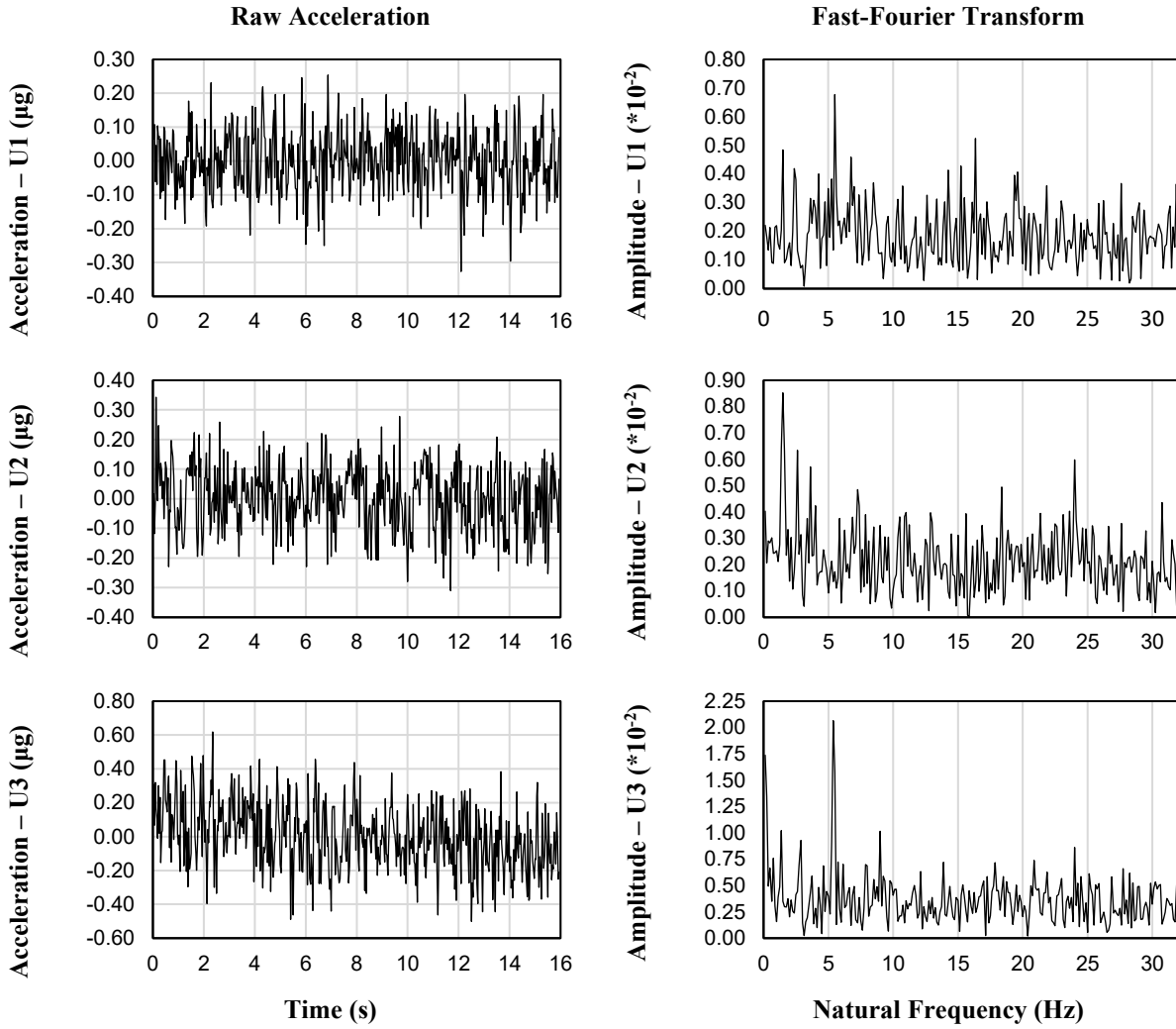
Figure 4.2. Raw acceleration and FFT result for sample taken on November 4, 2021, from the Location 4, Position 1 sensor.

Raw Acceleration   **Fast-Fourier Transform**
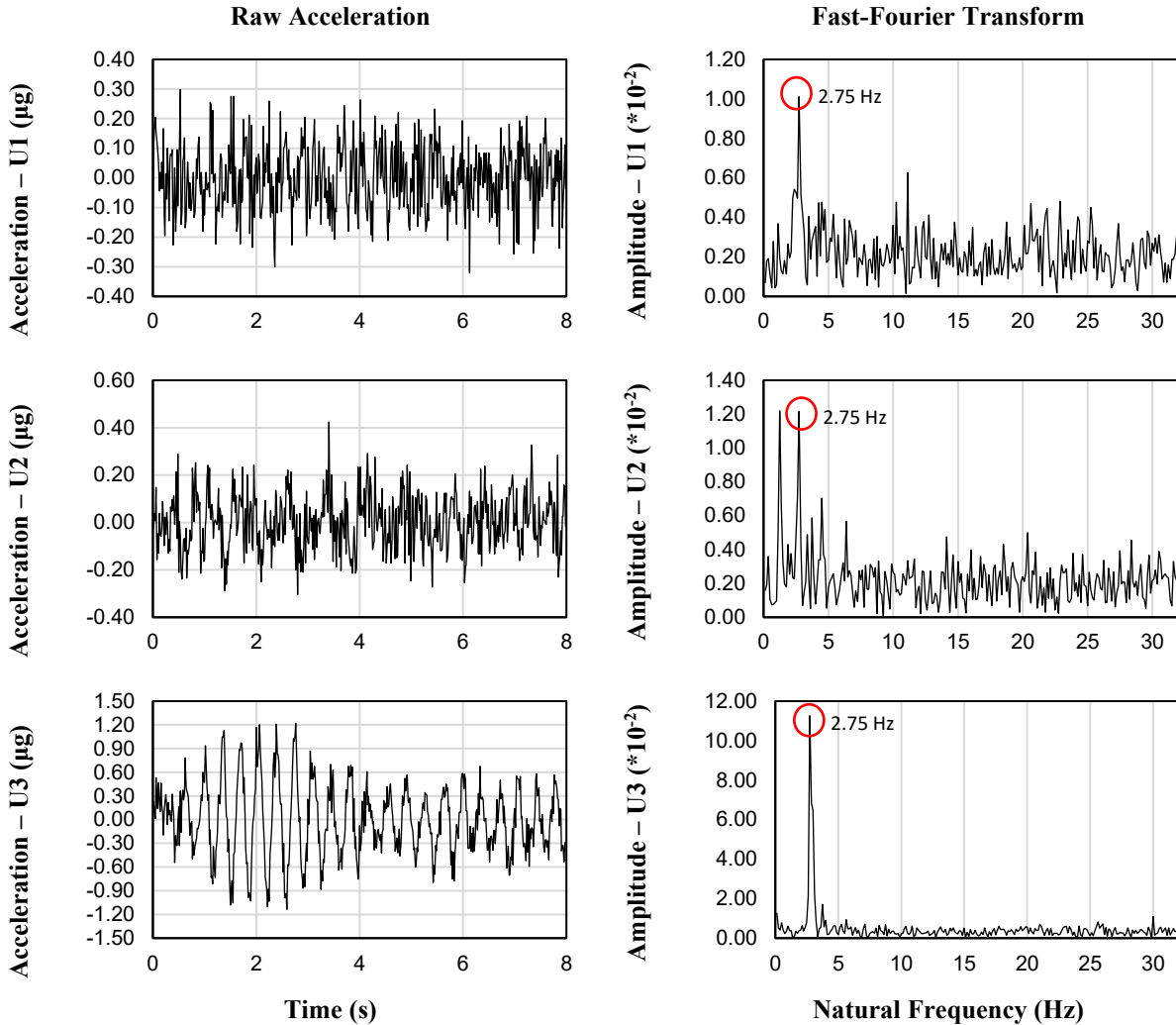
Figure 4.3. Raw acceleration and FFT result for sample taken on September 23, 2020, from the Location 4 Position 3 sensor showing vibration from power tools.

4.2.2 Comparison of Modal Properties

Mode shapes were calculated for the U3 (vertical) direction using an SSI-Cov MATLAB script developed by Cheynet, 2020. In lieu of acceleration data, accelerations of 0g were assumed at support locations due to the boundary conditions present at those locations. However, the same assumption cannot be made for the U1 (longitudinal) and U2 (transverse) directions since the boundary conditions at Pier 1 and Pier 3 are intended to only restrict movements in the vertical direction.

Tables 4-2 and 4-3 show the natural frequencies report by the SSI-Cov method for each day and each sensor position. Figure 4.4 shows a set of mode shapes for Position 1 sensors for Span 1 and Span 2. Natural frequencies around 0.125 Hz and 3.500 Hz appeared most frequently which may be evidence that they represent actual natural frequencies of the bridge. Most of the reported

natural frequencies and mode shapes do not appear consistently. This may be due to varying conditions on site during each site visit (e.g., wind speeds and/or construction activities), or excessive noise measured. Figure 4.5 shows three modes that were reported with very similar mode shapes and natural frequencies close together on the same day. This may be evidence that spurious modes were reported since true mode shapes for modes with natural frequencies close together should still be unique. Overall, it appears that more data collection is required for effectively measuring modal properties of the bridge under ambient excitation from moderate environmental loads and construction activities. It is notable that data was limited, and samples were coincidentally not taken during more severe environmental loading (e.g., intense wind speeds and/or storm events) which may have provided sufficient excitation for measuring modal properties.

Table 4.2. Span 1 Natural frequencies from SSI-Cov algorithm (U3 direction)

Day	Position #	Mode Number (Hz)				
		1	2	3	4	5
20210629	1	0.195	21.865	38.152	-	-
	2	1.079	9.742	12.780	14.932	14.948
	3	10.531	12.669	14.031	-	-
20210720	1	3.529	-	-	-	-
	2	1.330	3.485	10.499	12.234	-
	3	10.531	12.669	14.031	-	-
20210923	1	1.225	8.389	9.101	9.221	23.637
	2	1.365	1.366	3.516	14.773	-
	3	1.323	3.507	9.653	10.611	-
20210930	1	0.125	20.665	30.036	-	-
	2	5.967	6.543	10.419	30.022	-
	3	5.996	6.548	10.757	29.950	-
20211007	1	0.125	3.475	20.958	26.624	-
	2	3.461	15.415	-	-	-
	3	3.495	6.295	6.297	6.740	19.099
20211029	1	3.504	3.967	24.181	-	-
	2	1.964	3.480	9.462	10.314	-
	3	2.034	-	-	-	-
20211104	1	0.125	4.003	6.255	-	-
	2	3.528	15.091	29.722	-	-
	3	3.546	23.766	-	-	-

Table 4.3. Span 2 Natural frequencies from SSI-Cov algorithm (U3 direction)

Day	Position #	Mode Number (Hz)				
		1	2	3	4	5
20210629	1	0.125	19.206	29.854	-	-
	2	3.118	4.220	13.240	-	-
	3	5.753	14.620	17.300	18.486	-
20210720	1	2.991	3.761	-	-	-
	2	3.853	4.862	5.722	9.383	-
	3	5.753	14.620	17.300	18.486	-
20210923	1	2.804	-	-	-	-
	2	3.102	29.959	-	-	-
	3	1.205	2.810	30.015	-	-
20210930	1	14.299	-	-	-	-
	2	1.051	13.653	14.303	14.333	14.589
	3	13.730	14.303	-	-	-
20211007	1	8.710	8.948	21.118	21.173	-
	2	8.939	21.162	-	-	-
	3	2.793	5.750	8.835	21.154	21.160
20211029	1	0.125	2.774	31.183	-	-
	2	2.799	9.680	-	-	-
	3	8.505	10.524	23.256	-	-
20211104	1	5.336	-	-	-	-
	2	1.407	5.267	5.447	9.154	-
	3	2.748	5.426	5.735	8.367	-
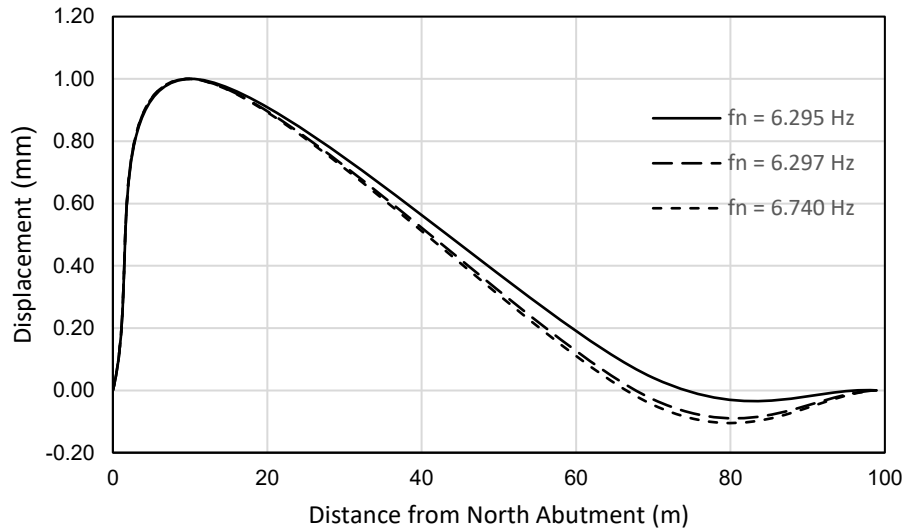
Figure 4.4. Span 1 mode shapes from October 7, 2021, showing possible spurious modes.

Comparing results of multiple analysis methods can be useful for providing redundancy and to help determine any potential issues with the data. The results of the Peak-Picking FFT method are provided in Table 4-4 and 4-5 for Location 1 and Location 4 sensors, respectively. Data is reported to three decimal places due to the FFT resolution of 0.125 Hz. A MATLAB script was used to pick the three peaks with the highest amplitudes for each FFT result and verified visually. Many of the FFT plots showed no peaks or the peaks were difficult to identify as shown by the modes with no natural frequencies reported. There appeared to be some agreements between the natural frequencies reported by the FFT and SSI-Cov methods. However, many natural frequencies did not match which may further indicate that spurious modes were reported, and/or excessive noise was present in the data.

Table 4.4. Span 1 Natural Frequencies from Location 1 using FFT (U3 direction). Bold indicates agreement with SSI-Cov results

Day	Position	Mode Number		
		1	2	3
20210629	1	17.900	20.400	24.600
	2	**12.900**	-	-
	3	-	-	-
20210720	1	14.000	22.600	29.100
	2	**1.500**	-	-
	3	-	-	-
20210923	1	**9.250**	-	-
	2	**3.620**	-	-
	3	**9.750**	-	-
20210930	1	**20.800**	23.800	**30.100**
	2	**6.620**	**30.100**	
	3	3.500	**6.620**	**30.100**
20211007	1	**21.100**		
	2	**3.620**	6.500	19.600
	3	**3.620**	6.380	
20211029	1	0.250	5.880	24.200
	2	**3.620**	-	-
	3	-	-	-
20211104	1	**4.120**	-	-
	2	-	-	-
	3	**3.620**	18.500	-

Table 4.5. Span 2 Natural Frequencies from Location 3 using FFT (U3 direction). Bold indicates agreement with SSI-Cov results

Day	Position	Mode Number		
		1	2	3
20210629	1	3.250	12.400	**19.400**
	2	**3.250**	-	-
	3	-	-	-
20210720	1	3.120	**3.880**	20.100
	2	3.120	**3.880**	-
	3	1.120	3.880	-
20210923	1	**2.880**	-	-
	2	2.880	-	-
	3	**2.880**	-	-
20210930	1	14.100	**14.250**	-
	2	**1.120**	2.880	**14.400**
	3	1.120	5.880	-
20211007	1	**9.000**	**21.200**	-
	2	**9.000**	**21.200**	-
	3	**21.200**	-	-
20211029	1	**2.880**	10.200	19.000
	2	**2.880**	-	-
	3	**2.880**	8.000	10.600
20211104	1	0.250	1.380	**5.500**
	2	**1.500**	**5.500**	**9.250**
	3	**2.880**	**5.500**	**5.880**
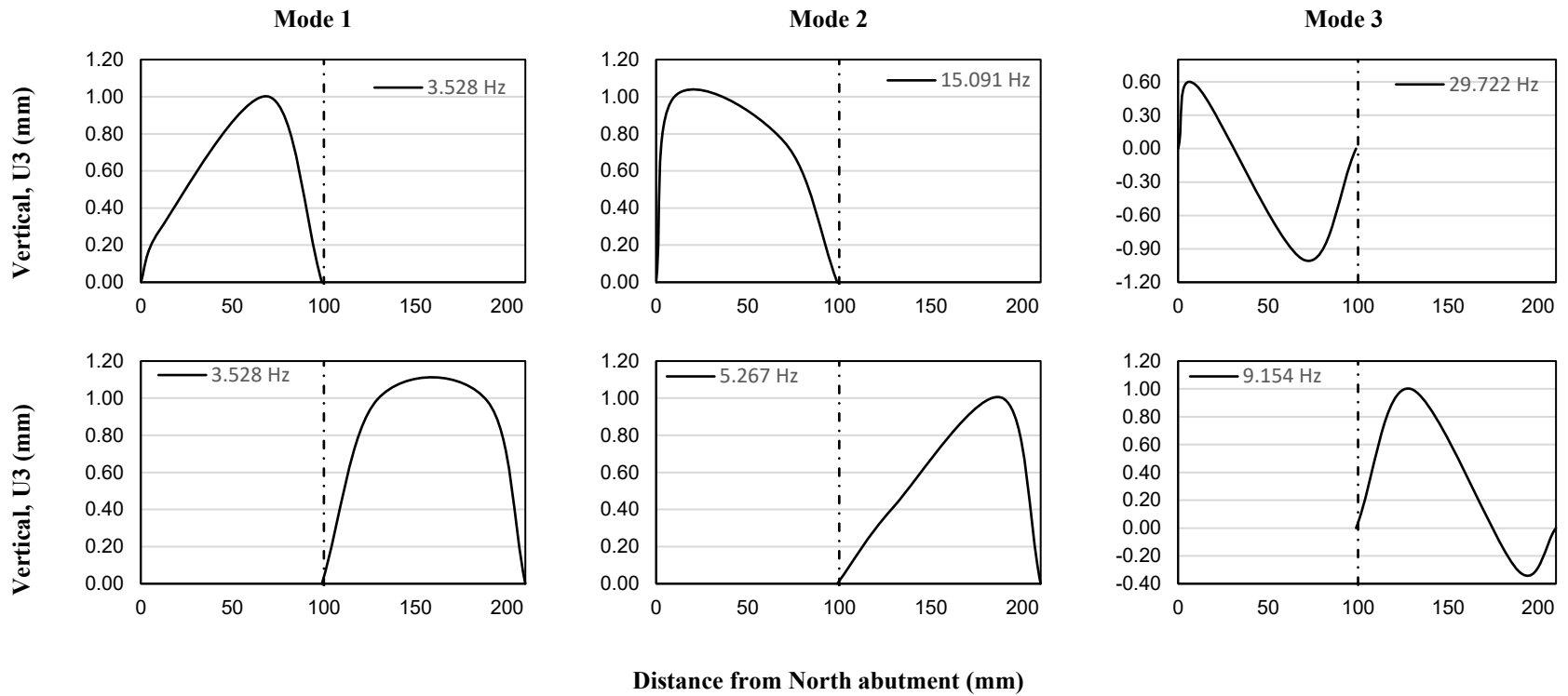
Figure 4.5. Span 1 and span 2 mode shapes from November 4, 2021 with vertical dashed line representing Pier 1

4.3   Dynamic Excitation

Dynamic excitation data was collected as a continuous measurement over the span of two hours with a measurement frequency of 32 Hz. Dynamic testing was performed on Span 2 only and consisted of five joggers running at specified frequencies, and two joggers running at unspecified slow, medium, and fast running paces. Figure 4.7 shows the notable test events in the acceleration response from Location 3, Position 1. Sensors in Location 3 had the greatest FFT amplitudes (see Section 4.3.1). The acceleration events were separated into seven different events for analysis. Events 1 and 2 were caused by a skid-steer crossing the SUP while events 2-7 were caused by the dynamic testing. It is unclear which events are related to which test from the acceleration response and modal properties alone, so a distinction could not be made. Each dynamic excitation event was analyzed separately using FFT for preliminary analysis and the SSI-Cov MATLAB script to find the modal properties of the bridge. A Blackman filter was applied to the data in both cases. Due to complications while retrieving some sensors, only those in Position 1 are analyzed and discussed.
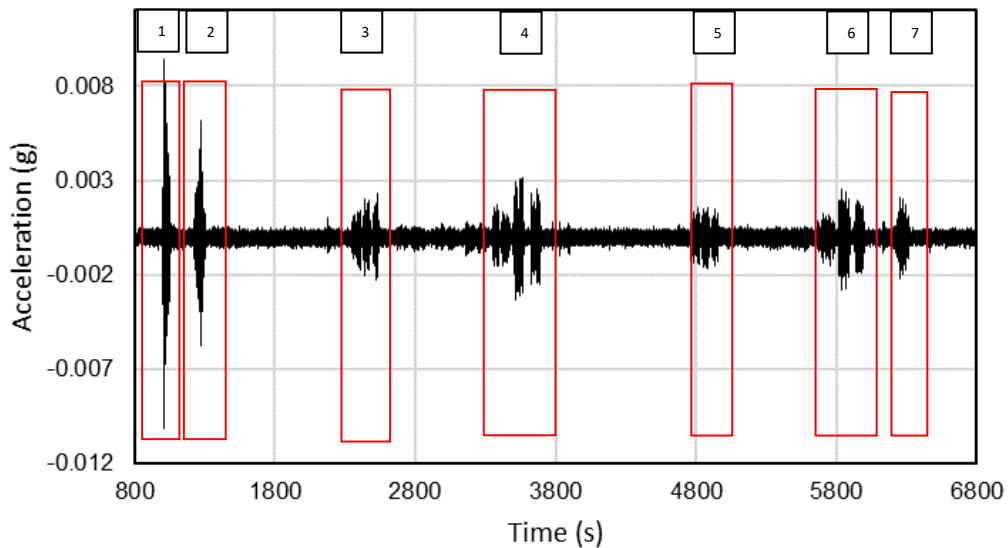
Figure 4.6. Raw dynamic testing acceleration response showing excitation events.

4.3.1 Preliminary Analysis with FFT

Figure 4.8 shows the raw accelerations and FFT results for the Position 1 sensors from dynamic testing Event 4. In general, the most prominent FFT peaks occur around 3.00 Hz for dynamic testing events with evidence of other peaks at relatively lower amplitudes. While there appear to be peaks in the FFT for Span 1 sensors, their amplitudes are much lower than those of the Span 2 sensors and appear to have more noise. The SNR for the Span 1 sensors are around 15.0 dB, while the SNR for the Span 2 sensors are around 24.5 dB. This shows the limitations of damage detection schemes focused on measuring global properties since accelerations can be very localized. FFT results at Location 3 had the greatest amplitudes which is likely due to it being the closest to midspan and experiencing the greatest deflections.

Figure 4.9 shows the raw accelerations and FFT results for the Position 1 sensors from skid steer Event 1. Like the dynamic testing events, the amplitudes of both the raw acceleration and FFT results for Span 1 were considerably smaller than those of Span 2. Overall, the peak amplitudes for the FFT responses due to skid steer events tended to be lower than those of the dynamic testing events and showed more noise despite having the greatest peak accelerations with SNRs ranging from approximately 4.8 dB to 7.8 dB. It appears the skid steer induces significant noise and is likely more representative of a typical ambient acceleration as compared to the dynamic tests which involved synchronized jogging.
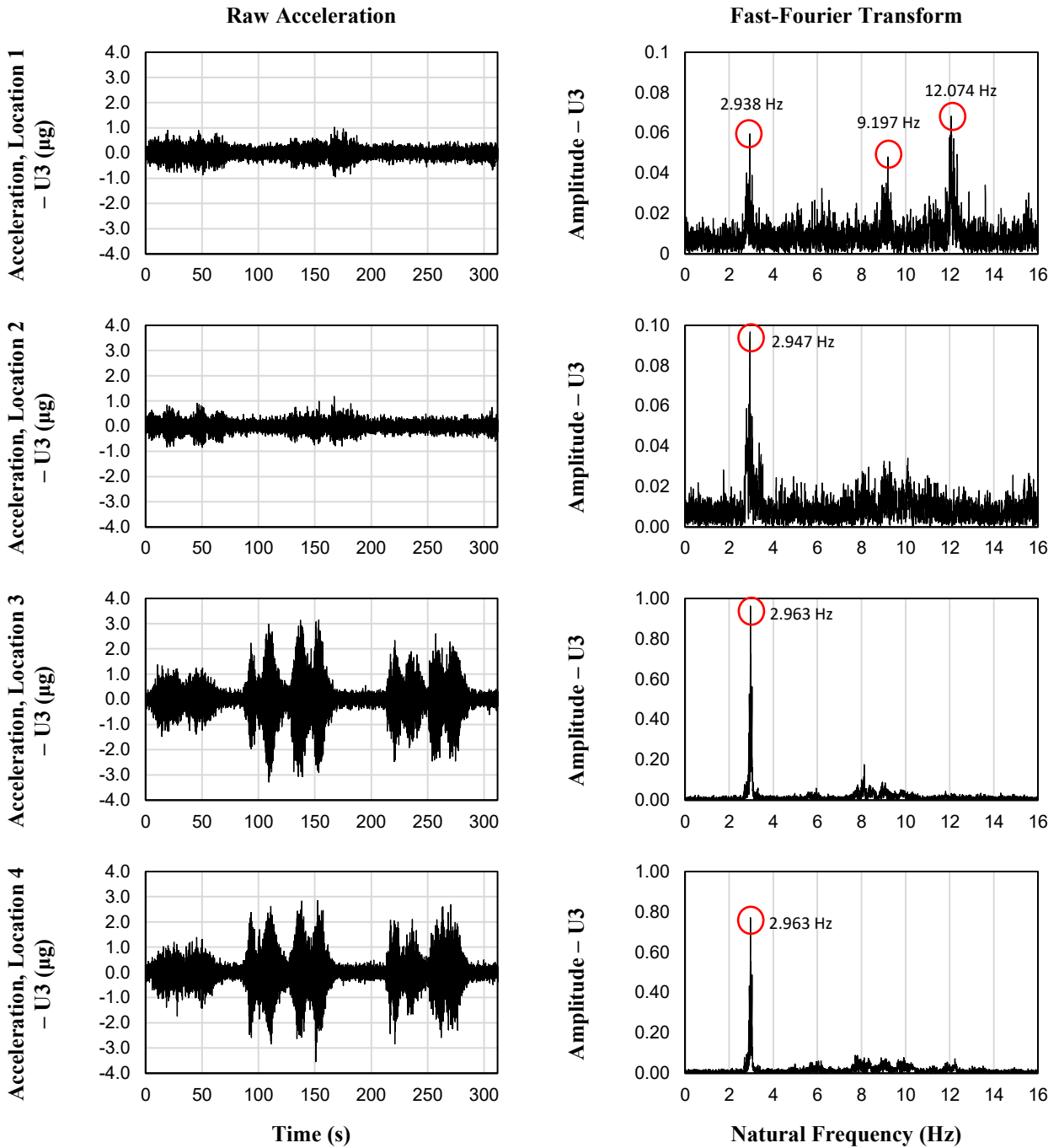
Figure 4.7. Raw acceleration and FFT result for dynamic testing event 4 from the Position 1 sensors with peaks shown
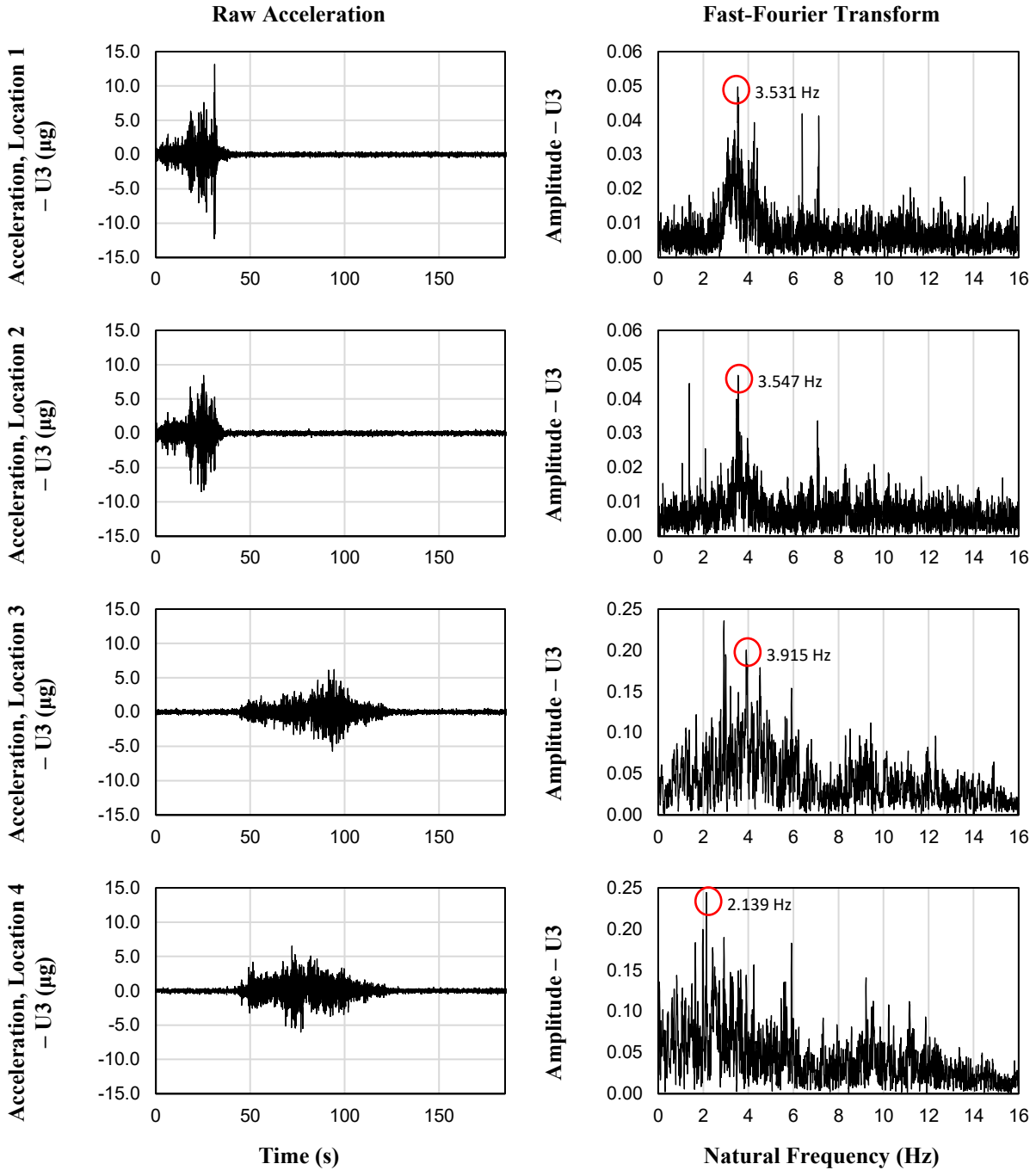
Figure 4.8. Raw acceleration and FFT result for skid-steer event 2 from the Position 1 sensors with peaks shown

4.3.2 Comparison of Modal Properties

Mode shapes were calculated for the U3 (vertical) direction using an SSI-Cov MATLAB script. Like the ambient excitation data, accelerations of 0g were assumed at support locations in lieu of sensors at those locations and mode shapes in the U1 (longitudinal) and U2 (transverse) directions were not considered.

Tables 4-6 and 4-7 show the natural frequencies reported by the SSI-Cov method for each dynamic excitation event. The results of the Peak-Picking FFT method are also provided in Tables 4-8 and 4-9 for Position 1 Sensors on Spans 1 and 2, respectively.

Using the SSI-Cov method, natural frequencies around 2.900-3.000 Hz and 11.900-12.000 Hz appeared the most frequently which could imply these represent actual natural frequencies of the bridge. Recurring natural frequencies were much more evident compared to the ambient excitation data which show the dynamic testing is effective in exciting different modes of the bridge. However, a closer look at the mode shapes shows poor matches even for mode shapes with very close natural frequencies as shown on Figure 4.9. This implies that the sensors may not be properly synchronized, and therefore the reported mode shapes for the dynamic testing events are likely inaccurate. Even a slight difference in synchronization (one hundredth or one thousandth of a second) can lead to misrepresented mode shapes. As a result, accurate mode shapes cannot be determined using the data collected.

A MATLAB script was used to pick the five peaks with the largest amplitudes for each FFT result and verified visually to remove false peaks. There appears to be some agreement between the FFT and SSI-Cov methods with over half of the natural frequencies reported by the FFT method agreeing with the SSI-Cov method. The agreement implies that the proposed sensor layout is effective in detecting the natural frequencies of the bridge when subject to forced excitation events, which could also imply that the proposed sensor layout may be effective in measuring the modal shapes under the same conditions if the data is properly synchronized. However, it is notable that for some results (particularly in Span 1) no peaks were evident in the FFT. This shows the limitations of sensor layouts focused on global modal responses when excitation does not occur close to a sensor.

Table 4.6. Dynamic testing span 1 natural frequencies from SSI-Cov algorithm (Position 1; U3 direction)

Mode	Event						
	1	2	3	4	5	6	7
1	3.555	1.378	3.197	2.803	2.937	2.934	2.787
2	3.8	3.137	3.208	2.939	3.547	3.447	2.909
3	10.547	3.348	3.561	12.114	3.552	9.21	3.033
4	11.367	3.469	5.1	12.334	5.072	9.212	3.452
5	-	3.549	6.435	-	12.108	11.247	6.202
6	-	3.685	6.737	-	12.133	11.997	13.608
7	-	3.983	9.495	-	12.871	11.998	-
8	-	4.243	10.098	-	-	12.256	-
9	-	4.361	12.164	-	-	-	-
10	-	7.118	12.888	-	-	-	-

Table 4.7. Dynamic testing span 2 natural frequencies from SSI-Cov algorithm (Position 1; U3 direction)

Mode	Event						
	1	2	3	4	5	6	7
1	11.013	1.989	2.933	2.912	2.867	2.879	2.716
2	11.381	2.137	7.798	2.971	2.917	2.942	2.894
3	11.751	2.913	8.096	3.039	3.021	3.026	2.93
4	12.31	3.549	8.097	7.824	3.143	3.037	3.038
5	-	3.922	9.841	8.118	7.988	6.05	5.901
6	-	4.508	-	8.339	8.229	6.075	11.9
7	-	-	-	8.919	8.41	8.459	11.939
8	-	-	-	-	9.848	8.86	-
9	-	-	-	-	-	-	-
10	-	-	-	-	-	-	-

Table 4.8. Dynamic testing span 1 natural frequencies using FFT (Location 2, Position 1; U3 direction). Bold indicates agreement with SSI-Cov results

Day	Mode Number				
	1	2	3	4	5
Event1	**3.563**	**11.397**	11.984	-	-
Event2	**1.381**	**3.568**	**7.077**	-	-
Event3	-	-	-	-	-
Event4	**2.941**	9.917	**12.074**	-	-
Event5	-	-	-	-	-
Event6	**2.954**	**3.434**	6.208	9.094	11.981
Event7	**2.912**	**3.477**	-	-	-

Table 4.9. Dynamic testing span 2 natural frequencies using FFT (Location 3, Position 1; U3 direction). Bold indicates agreement with SSI-Cov results

Day	Mode Number				
	1	2	3	4	5
Event1	5.861	**11.296**	**12.224**	13.109	14.667
Event2	**2.139**	5.915	9.546	-	-
Event3	**2.928**	5.819	**7.797**	8.405	9.648
Event4	**2.963**	**8.122**	9.078	-	-
Event5	**2.917**	6.096	**8.235**	**9.941**	11.920
Event6	**2.950**	**6.045**	8.902	11.875	12.966
Event7	**2.917**	**5.883**	**11.968**	12.629	-
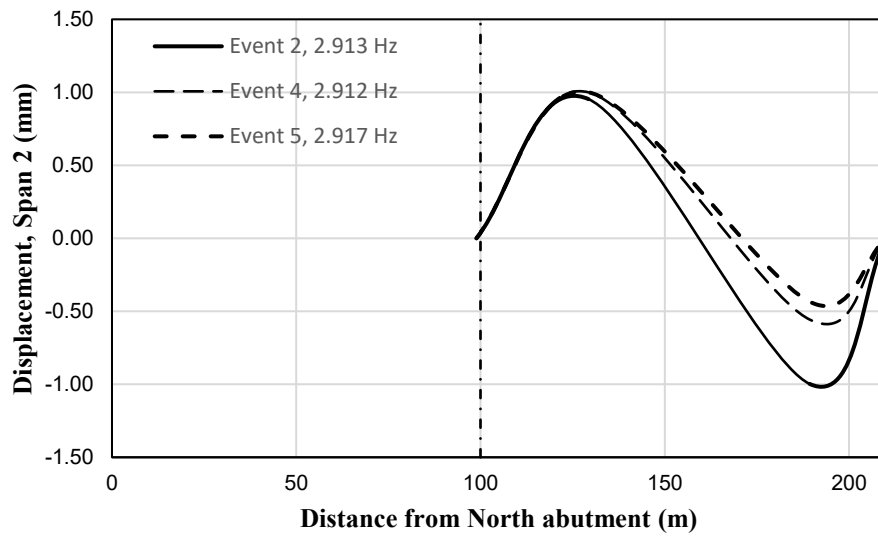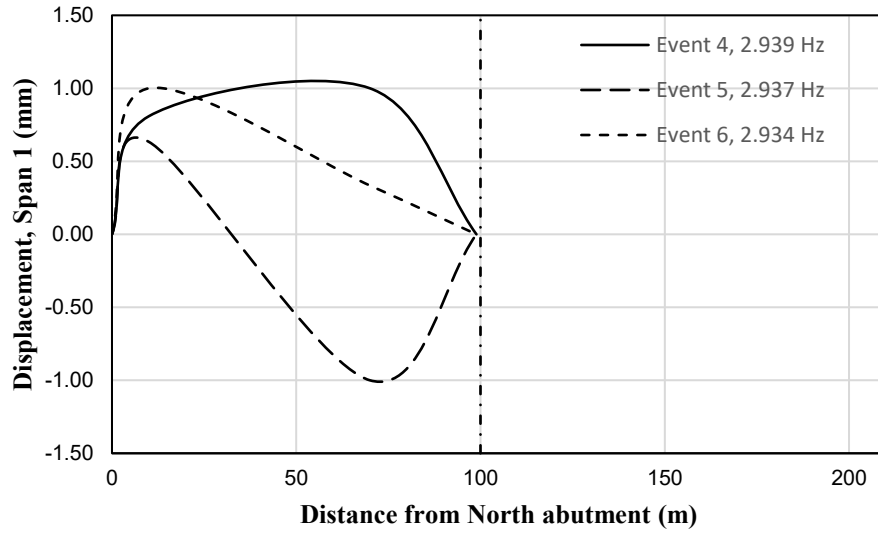
Figure 4.9. Mode shapes with close natural frequencies showing disagreement which could imply accelerometer syncing issues. Vertical dashed line represents Pier 1

4.4 Limitations and Recommendations

The proposed sensor layout was not as effective in measuring mode shapes in some cases as noted throughout Sections 4.2 and 4.3. Mode shapes were only calculated in the U3 direction since sensors were not installed at support locations, making it impossible to determine mode shapes in the U2 and U1 directions. FFT results for the ambient testing may have had insufficient resolution to accurately determine natural frequencies due to the frequency and length for each vibration sample. Additionally, restrictions imposed by the government during the COVID-19 pandemic limited the frequency and duration of site visits for data collection. More data is required to effectively determine a baseline response.

To allow mode shapes to be calculated in the U1 and U2 directions (and remove the need to create assumptions for calculating mode shapes in the U3 direction), sensors can be relocated and placed at supports. Relocating sensors to include the mid-spans of Span 1 and Span 2 also allows for more detailed mode shapes by adding additional data points along the spans. Sensors placed at midspan are likely to show better FFT results (as shown in Section 4.3.1). Figure 4.10 shows an improved sensor layout which relocates the sensors in the original proposed layout and maintains a total of 12 sensors. A drawback of the improved layout is the inability to detect torsion, which could be improved by placing the sensors as shown in Figure 4.11.
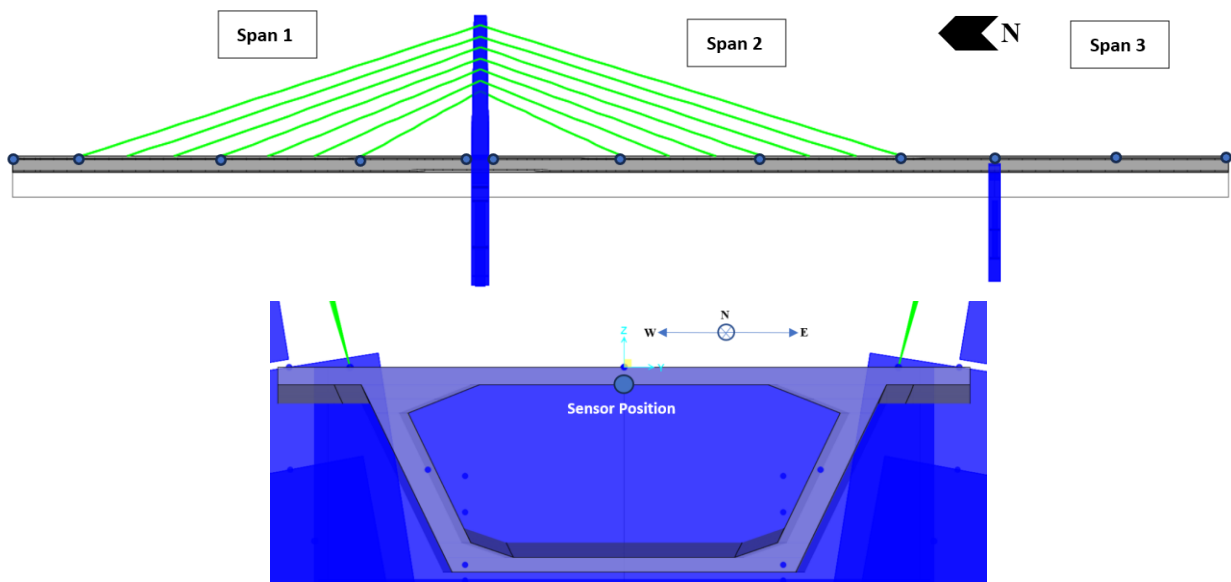
Figure 4.10. Improved sensor layout with sensors placed at supports, midspans, and including span 3
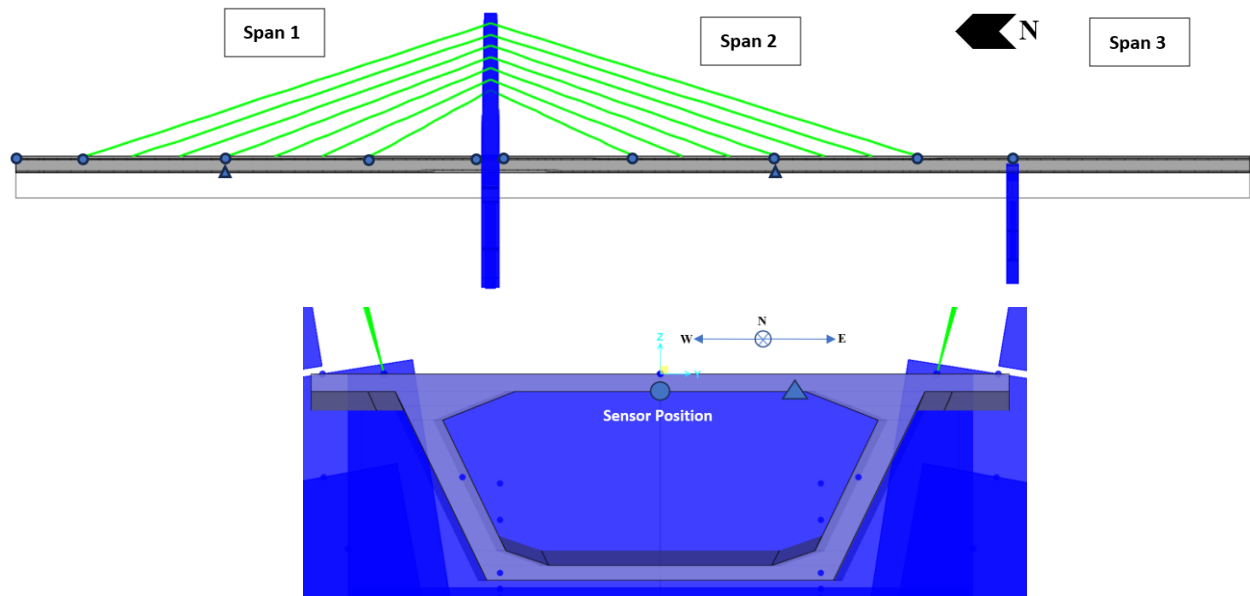
Figure 4.11. Improved sensor layout allowing for torsion measurements

Additional improvements include developing an analytical model and performing modal analysis to determine the critical points of the structure for sensor placement. Issues also arose due to the frequency of testing which limited the data collected and resulted in poor FFT resolution. The addition of two or more data acquisition units permanently installed on the bridge and connected to a wireless network would allow for more remote data collection and improved data synching. This would resolve the issues found in Sections 4.2 and 4.3 where mode shapes could only be measured at each span separately due to syncing issues. Allowing remote data collection would also increase the frequency of data collection and length of samples for improved resolution. A remote data collection system which stores data using online data storage allows for the possibility of automatic model updating.

Other types of sensors which could be use under unconstrained circumstances (e.g., budget, duration of monitoring, and access to site) include input measurement devices such as WIM sensors, and anemometers. WIM sensors can be placed at both the north and south bridge approaches to measure train loads. Anemometers can be placed at deck level and at the top of the stay tower to measure wind loads. A means of measuring the structural input can help provide context to the modal properties measured and allow users to better understand the behaviour of the structure under various loads. Input measurements could also help rule out false positives that may be detected as anomalies.

4.5 Chapter Summary

This chapter discussed the results of ambient and dynamic testing on the Tawatinâ Bridge and presented a framework, through recommendations, for future monitoring of the bridge. Ambient testing refers to data collected during the construction of the shared-use-pathway (SUP) over ten site visits where the bridge was subject to excitation from construction activities and environmental loads such as wind. Dynamic testing refers to data collected during dynamic tests where the bridge was subject to excitation from synchronized runners jogging at various speeds. Accelerometers were deployed according to the proposed sensor layout discussed in Chapter 3. Acceleration data was processed using a Peak-Picking Fast-Fourier Transform (FFT) method to determine the natural frequencies of the bridge and an SSI-Cov MATLAB script was used to determine both the natural frequencies and mode shapes of the bridge. The natural frequency results of the FFT and SSI-Cov methods were compared to validate the reported natural frequencies.

The data collected from the ambient testing appeared to have considerable noise. While some samples showed prominent peaks in the FFT plots, many of the samples showed no peaks or the peaks were difficult to identify. The modal properties reported by the SSI-Cov method also showed very few mode shapes that appear consistently between different days which may be a result of the limitations of the proposed sensor layout, limitations of the analysis methods, or varying conditions on site during each site visit. It also appears that some spurious modes were reported since multiple modes reported on the same had very similar modal properties. Based on the results of the ambient testing, more data collection is required for effectively measuring the modal properties of the bridge under ambient excitation from environmental loads and construction activities.

The analysis results from the dynamic testing showed more recurring natural frequencies as compared to the ambient testing. There also appeared to be good agreement between the natural frequencies reported by the FFT method and the SSI-Cov method with many of the natural frequencies reported by the FFT method agreeing with the SSI-Cov method. Issues with the synchronization of the sensors make it infeasible to report accurate mode shapes for the bridge. However, the forced excitation appeared to be effective in exciting some of the natural frequencies of the bridge which implies the mode shapes of the bridge could be measured under the same conditions if the data is properly synchronized.

Overall, a baseline response could not be accurately measured in part due to limitations of the sensor layout and data collection methods which were made evident in Sections 4.2 and 4.3. Some of these limitations were also discussed in Section 4.4 and recommendations were provided for future study. Additional data collection, even with the used sensor layout, could reduce the impacts of noise and help establish a baseline for future monitoring. Relocating some of the sensors along the bridge would create more detailed mode shapes and reduce the required assumptions. Developing an analytical model of the bridge could assist with identifying potential sensor locations. Improvements to the data acquisition system would also improve the synchronization of the sensors and allow for easier data collection and better resolutions. Finally, a data collection system which takes advantage of online data storage would allow for automatic updating of an analytical model.

Chapters 5 and 6 investigate the damage detection applications of a vibration-based structural health monitoring scheme. An analytical model developed using CSiBridge is analyzed using an eigenvector analysis in Chapter 5 to determine the possible mode shapes of the bridge. Chapter 6 discusses the analysis of the same model using a linear modal time history analysis to collect acceleration data from a simulated train load and determine the mode shapes using similar methods used in this chapter. In both cases, baseline mode shapes are determined from a healthy structure and compared with various simulated damage cases. The models also incorporate the proposed sensor layout discussed in this chapter with additional sensor locations added.

CHAPTER 5.   EIGENVECTOR ANALYSIS

This chapter investigates the effects of different damage scenarios on the natural frequencies and mode shapes (modal properties) of the Tawatinâ Bridge (Figure 5.1) modelled using CSiBridge. The modal properties were determined using an Eigenvector Analysis in CSiBridge. Natural frequencies and mode shapes were compared between a baseline case and each damage case. The mode shapes of each sensor position (Figure 5.2) were compared in the U3 (vertical), U2 (transverse), and U1 (longitudinal) directions. Dynamic analysis was also performed using an estimate of the expected real-life train loads and modal properties were calculated using a Covariance-Driven Stochastic Subspace Integration (SSI-Cov) MATLAB script developed by Cheynet (2020). The dynamic analysis case is discussed further in Chapter 6.

5.1   Baseline Model

Before performing damage simulation, the modal properties of the baseline model were calculated using CSiBridge to determine the properties of a healthy structure. Three baseline models with varying nodes in the stay tower were compared to determine the most stable modes. Sixteen modes were calculated for each model and compared using the Modal Assurance Criterion (MAC). Ten Modes matched with MAC values of 1.000 while the remaining six modes were rejected for low MAC values. The natural frequencies and deformed shapes of the ten useful modes are shown in Figure 5.3. Modal properties of each damage case were compared with the modal properties of the baseline case to determine which modal properties, if any, are sensitive to each type of damage.
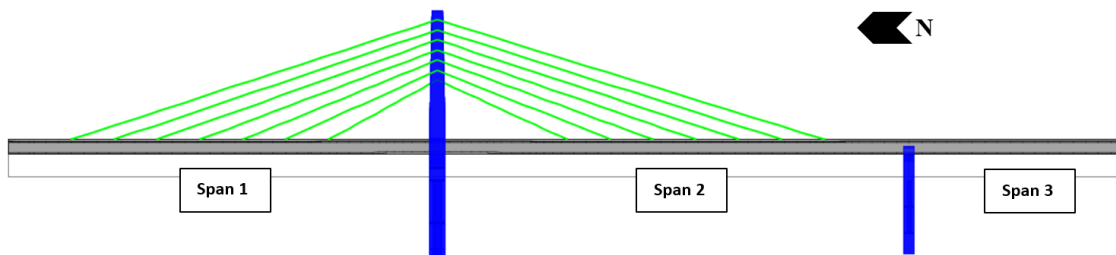
Figure 5.1. Tawatinâ bridge profile view showing span labels
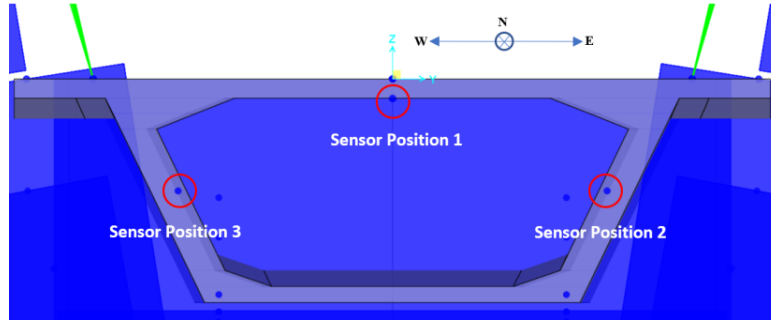
Figure 5.2. Box girder cross section showing sensor positions

Mode 1: T=1.077 s, f=0.928 Hz
(Bending)

Mode 2: T=0.837 s, f=1.195 Hz
(Bending)

Mode 3: T=0.837 s, f=0.957 Hz
(Transverse Bending)

Mode 4: T=0.837 s, f=1.195 Hz
(Longitudinal/Bending)

Mode 5: T=0.762 s, f=1.313 Hz
(Torsion/Transverse Bending)

Mode 6: T=0.675 s, f=1.482 Hz
(Bending)

Mode 7: T=0.569 s, f=1.756 Hz
(Transverse Bending)

Mode 8: T=0.473 s, f=2.116 Hz
(Second Order Bending)

Mode 9: T=0.386 s, f=2.590 Hz
(Second Order Bending)

Mode 11: T=0.317 s, f=3.154 Hz
(Tower Bending)
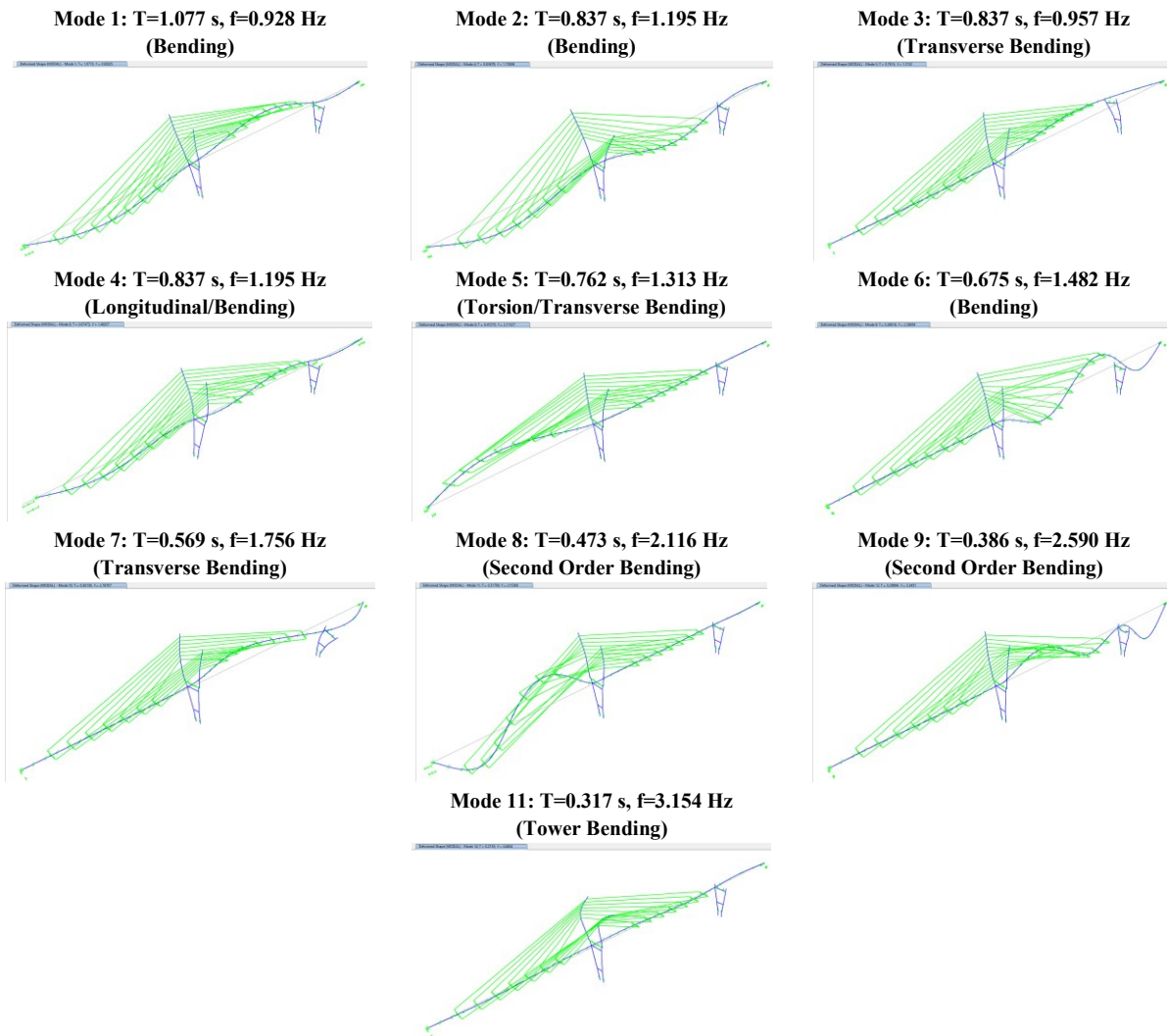
Figure 5.3. Baseline mode shapes for the ten modes with MAC = 1.000 with period, T, and natural frequency, f

5.2 Damage Simulation

The damage cases are divided into four categories: bearing damage, stay cable damage, girder damage, and tower damage. Reasoning for each damage case category is discussed in following sections. A summary of the considered damage cases is shown in Table 5-1 and Figure 5.4. The MAC was calculated and used to compare each mode shape of the damaged case to each mode shape of the baseline case. Mode shapes were moved around accordingly to ensure the most similar mode shapes were being compared between the damaged and baseline cases. The MAC was also used as an objective measure of which mode shapes were the most sensitive to damage.

Table 5.1. Damage simulation scheme

Damage ID	Category	Location	Change
BD	Bearing Damage	North Abutment; Pier 2 Support	Change roller supports to pin supports.
CD-1*	Stay Cable Damage	Cable 7	Tension reduction: 25%, 50% and 75%
CD-2*	Stay Cable Damage	Cables 1-6	Tension reduction: 25%, 50% and 75%
CD-3	Stay Cable Damage	All Cables	Tension reduction: 25%, 50% and 75%
GD-1	Girder Damage	Segment SP1 and NP1	Stiffness reduction: 25% and 75%
GD-2	Girder Damage	Segment SP1, NP1, SQ12, and NQ12	Stiffness reduction: 25% and 75%
TD	Tower Damage	Stay Tower at deck level	Stiffness reduction: 25% and 75%

*: Not found to have significant impacts on modal properties and is therefore not discussed in detail in this chapter.
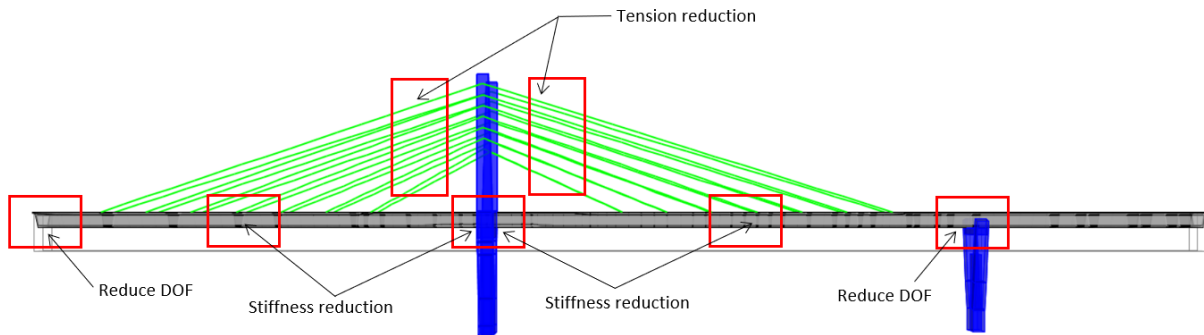
Figure 5.4. Damage simulation scheme

5.2.1 Bearing Damage (BD)

Bearing damage was simulated by replacing the roller bearings with pin supports in order to reduce the degrees of freedom. The additional restraints represent damage due to debris or wearing on the bearing surfaces leading to increased friction between the bridge and the bearings. Changes in modal properties for this damage case are expected to have a notable impact on global behaviour since it creates a change in boundary conditions.

Modes with average MAC values close to zero were omitted (modes 4, 10, and 12). Figure 5.5 shows the natural frequency changes between the baseline and damaged case. Due to the increased stiffness from restricting degrees of freedom at the supports, the natural frequency of most mode shapes also increased. Mode 5 sees the greatest natural frequency increase of 36%.

Tables 5-2 to 5-4 show the natural frequencies for each mode and the MAC values for each sensor position and direction. All mode shapes are affected by the change in boundary conditions with the average MAC value (averaged between the U1, U2, and U3 directions) for most modes being 0.8000 or larger. In position 1, modes 3 (transverse bending), 5 (torsion/lateral bending), and 11 (tower bending) show the most sensitivity to damage in the U3 direction with MAC values of 0.4742, 0.3656, and 0.5914 respectively. The rest of the MAC values for position 1 in the U3 direction were around 0.8000 or greater. Position 2 and 3 had nearly identical mode shapes and MAC values. The most sensitive modes in the U3 direction were modes 2 (bending), 8 (span 1 second order bending), and 11 (tower bending) with MAC values of 0.8866, 0.8497 and 0.7559 respectively. For all positions, mode shapes in the U2 direction have MAC values of 0.8000 or greater with the exception of mode 8 which consistently had MAC values of around 0.3600 or lower for all positions. Mode shapes in the U1 direction were generally the most affected with a majority of the MAC values being around 0.6000 or lower with some values being close to zero.

The sensitivity of the mode shapes in the U1 direction is likely due to the original bearings consisting of guided and sliding pot bearings where movement in the U1 direction is not restricted. Upon investigating all mode shapes, mode 8 (Figure 5.6) seems to be the most sensitive to this damage case overall. It seems the additional restraints to both the longitudinal and transverse directions cause additional second order bending to span 2 and an increase of midspan transverse deflections. However, this damage could also be easily detected across any mode as it appears to have a drastic change to all mode shapes along with noticeable differences in natural frequencies.
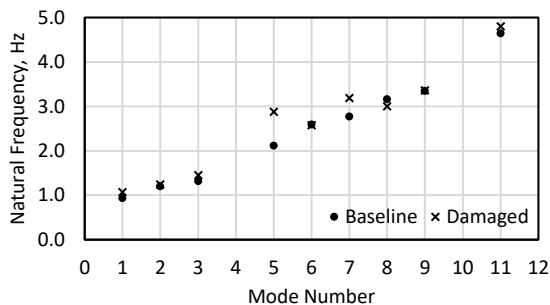
Mode	Baseline	Damaged	Percent difference
1	0.9282	1.0705	15%
2	1.1951	1.2422	4%
3	1.3132	1.4468	10%
5	2.1153	2.8732	36%
6	2.5896	2.5722	-1%
7	2.7671	3.1821	15%
8	3.1537	2.9981	-5%
9	3.3451	3.3548	0%
11	4.6404	4.7949	3%

Figure 5.5. Natural frequency comparison with percent differences (BD). Modes 4, 10, and 11 were omitted.

Table 5.2. BD Position 1 MAC Comparison (Top of Girder).

Mode Shape	Natural Frequency (Hz)		MAC Values			
	Baseline	Damaged	U3	U2	U1	Average
1	0.9282	1.0705	0.8866	0.8729	0.0297	0.5964
2	1.1951	1.2422	0.8498	0.8524	0.0347	0.5790
3	1.3132	1.4468	0.4742	0.9542	0.6377	0.6887
4	-	-	-	-	-	-
5	2.1153	2.8732	0.3656	0.9426	0.2845	0.5309
6	2.5896	2.5722	0.9961	0.8747	0.2344	0.7017
7	2.7671	3.1821	0.7922	0.9270	0.1209	0.6134
8	3.1537	2.9981	0.8111	0.3674	0.2431	0.4738
9	3.3451	3.3548	0.9808	0.8949	0.2060	0.6939
10	-	-	-	-	-	-
11	4.6404	4.7949	0.5914	0.8582	0.4097	0.6197
12	-	-	-	-	-	-

Table 5.3. BD Position 2 MAC Comparison (East Girder Wall)

Mode Shape	Natural Frequency (Hz)		MAC Values			
	Baseline	Damaged	U3	U2	U1	Average
1	0.9282	1.0705	0.8866	0.9459	0.0551	0.6292
2	1.1951	1.2422	0.8499	0.9373	0.3890	0.7254
3	1.3132	1.4468	0.9987	0.9519	0.7553	0.9020
4	-	-	-	-	-	-
5	2.1153	2.8732	0.9875	0.9398	0.4788	0.8020
6	2.5896	2.5722	0.9961	0.8091	0.0250	0.6101
7	2.7671	3.1821	0.9842	0.9235	0.6155	0.8411
8	3.1537	2.9981	0.8111	0.2807	0.5355	0.5424
9	3.3451	3.3548	0.9808	0.8355	0.1100	0.6421
10	-	-	-	-	-	-
11	4.6404	4.7949	0.7651	0.8592	0.5783	0.7342
12	-	-	-	-	-	-

Table 5.4. BD Position 3 MAC Comparison (West Girder Wall)

Mode Shape	Natural Frequency (Hz)		MAC Values			
	Baseline	Damaged	U3	U2	U1	Average
1	0.9282	1.0705	0.8866	0.9459	0.0553	0.6293
2	1.1951	1.2422	0.8497	0.9373	0.3914	0.7261
3	1.3132	1.4468	0.9755	0.9519	0.7566	0.8947
4	-	-	-	-	-	-
5	2.1153	2.8732	0.9863	0.9398	0.4772	0.8011
6	2.5896	2.5722	0.9961	0.8091	0.0250	0.6101
7	2.7671	3.1821	0.9836	0.9235	0.6147	0.8406
8	3.1537	2.9981	0.8111	0.2807	0.5357	0.5425
9	3.3451	3.3548	0.9808	0.8355	0.1100	0.6421
10	-	-	-	-	-	-
11	4.6404	4.7949	0.7559	0.8592	0.5769	0.7307
12	-	-	-	-	-	-
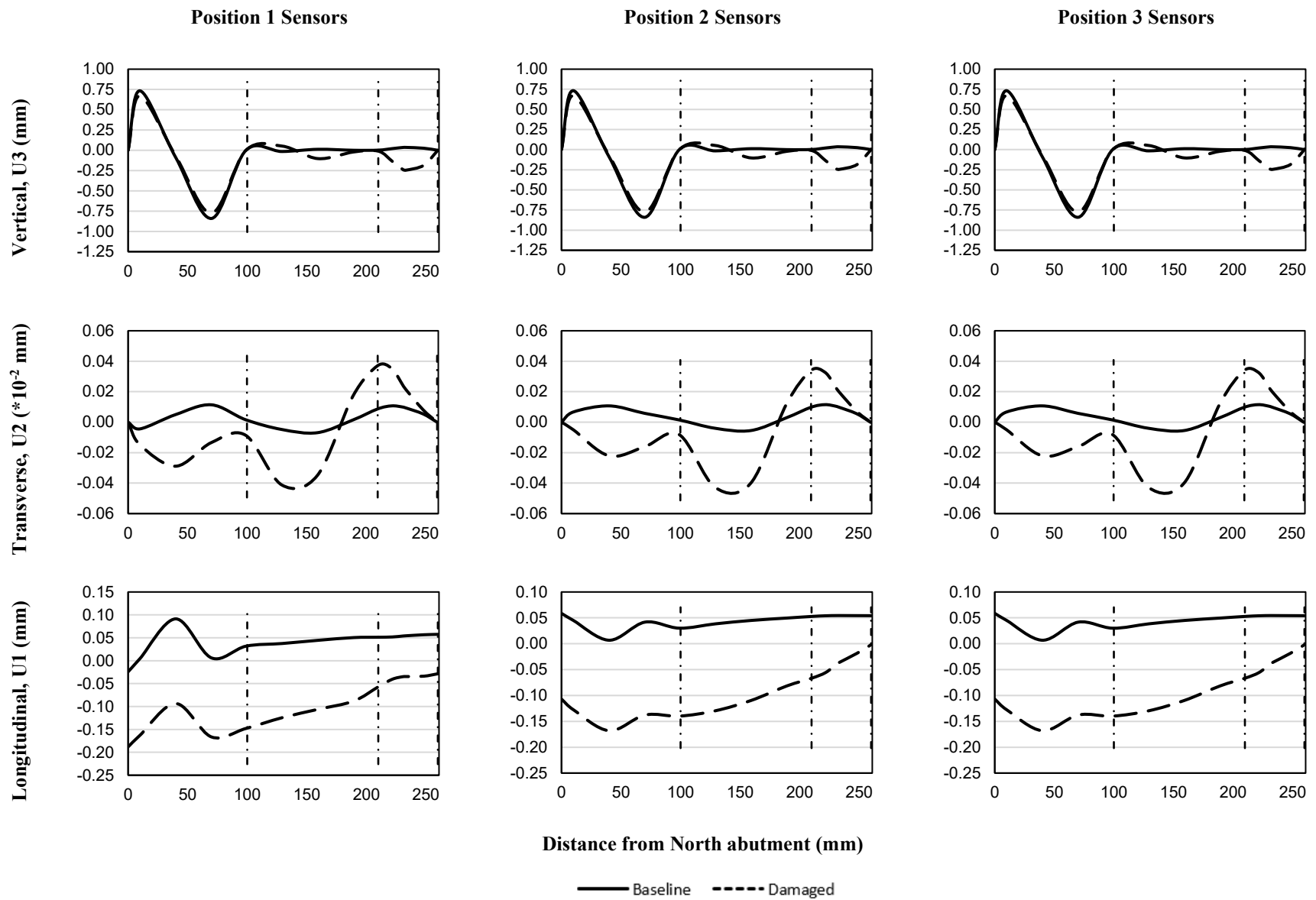
Figure 5.6. Mode shape 8 comparison (BD). Vertical dashed lines indicate the location of the supports.

5.2.2 Stay Cable Damage (CD-3)

Stay cables can be damaged from corrosion or wearing of materials due to fatigue over time which could lead to relaxation. Each set of stay cables is labelled from 1 to 7 as shown on Figure 5.7. The bridge is statically indeterminant due to the redundancy from the stay cables. This means that loads have various possible paths to transfer into the supports. Due to this redundancy, the removal of one cable is not expected to have much effect on the global behaviour of the bridge. From preliminary modal analysis, it was found that no set of cables had a notable impact on modal properties on their own. CD-1 and CD-2 were found to have almost no changes to modal properties but is still considered for dynamic analysis (Chapter 6). Therefore, damage case CD-3 is shown and involves simulating damage to all stay cables by applying tension reductions of 25%, 50%, and 75%.
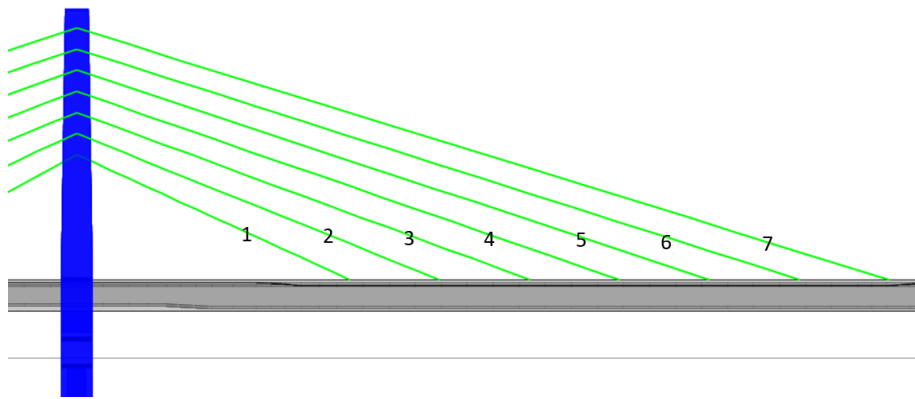
Figure 5.7. Layout of stay cables with labels shown

Decreasing tension in the cables reduces redundancy of the structure. A significant reduction in girder stiffness is also expected since the cables in an extradosed bridge provide external post-tensioning effects (refer to Section 2.8). Therefore, a notable impact is expected on the modal properties of the bridge.

Figure 5.8 shows the change in natural frequencies, and Tables 5-5 to 5-7 show the average MAC for each mode shape. Mode 1 (bending) shows the greatest change in natural frequency with percent differences ranging from -0.2% to -0.5% as damage increases, but the change is very small and would be difficult to detect in practice. Modes 1 and 3 show slight sensitivity to the damage case based on their MAC values. Mode 1 shows the greatest decrease in MAC value for all 3 sensor positions. For all 3 positions, the decrease in average MAC value is identical and ranges from 1.000 to 0.9929 as damage increases.

Figure 5.9 shows the deflected shape of mode 1 for CD. Inspection of the deflected shapes show a slight increase in transverse deflections at 75% damage, but no notable differences elsewhere. The lack of change to the vertical deflected shapes is likely due to redundancies from the box girder and the post-tensioning effects which reduce vertical deflections. Reducing tension in the cables may cause a reduction in stiffness for the U2 direction which explains the change in transverse deflections. However, changes due to this damage case are very slight even at large levels of damage, which implies this damage case may not be detectable using modal identification methods.

Mode	25% Damage	50% Damage	75% Damage
1	-0.2%	-0.3%	-0.5%
2	-0.1%	-0.2%	-0.3%
3	-0.1%	-0.1%	-0.2%
4	0.0%	0.0%	0.0%
5	0.0%	-0.1%	-0.1%
6	0.0%	0.0%	0.0%
7	0.0%	0.0%	0.0%
8	0.0%	0.0%	0.0%
9	0.0%	0.0%	0.0%
10	-	-	-
11	0.0%	0.0%	0.0%
12	-	-	-
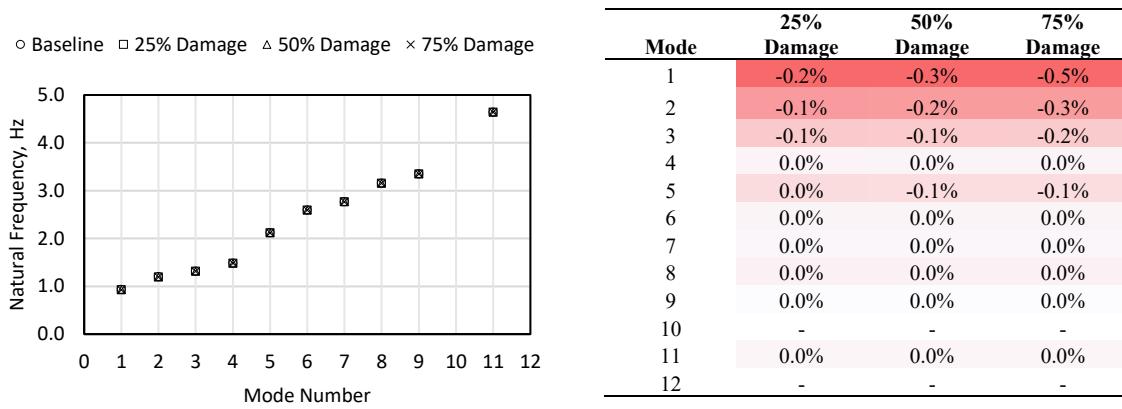
Figure 5.8. Natural frequency comparison with percent differences (CD-3)

Table 5.5. CD-3 Position 1 MAC Comparison (Top of Girder)

Mode Shape	Natural Frequency (Hz)				MAC (Average of U1, U2 and U3)		
	Baseline	25% Damage	50% Damage	75% Damage	25% Damage	50% Damage	75% Damage
1	0.9282	0.9266	0.9249	0.9233	1.0000	0.9989	0.9929
2	1.1951	1.1936	1.1922	1.1907	1.0000	1.0000	1.0000
3	1.3132	1.3122	1.3112	1.3103	1.0000	1.0000	1.0000
4	1.4821	1.4819	1.4816	1.4814	1.0000	1.0000	1.0000
5	2.1153	2.1144	2.1135	2.1125	0.9999	1.0000	1.0000
6	2.5896	2.5892	2.5888	2.5884	1.0000	1.0000	1.0000
7	2.7671	2.7668	2.7665	2.7662	0.9999	1.0000	1.0000
8	3.1537	3.1531	3.1526	3.1520	0.9999	1.0000	1.0000
9	3.3451	3.3449	3.3448	3.3446	1.0000	1.0000	1.0000
10	-	-	-	-	-	-	-
11	4.6404	4.6397	4.6390	4.6382	1.0000	1.0000	1.0000
12	-	-	-	-	-	-	-

Table 5.6. CD-3 Position 2 MAC Comparison (East Girder Wall)

Mode Shape	Natural Frequency (Hz)				MAC (Average of U1, U2 and U3)		
	Baseline	25% Damage	50% Damage	75% Damage	25% Damage	50% Damage	75% Damage
1	0.9282	0.9266	0.9249	0.9233	1.0000	0.9989	0.9929
2	1.1951	1.1936	1.1922	1.1907	1.0000	1.0000	1.0000
3	1.3132	1.3122	1.3112	1.3103	1.0000	1.0000	1.0000
4	1.4821	1.4819	1.4816	1.4814	1.0000	1.0000	1.0000
5	2.1153	2.1144	2.1135	2.1125	1.0000	1.0000	1.0000
6	2.5896	2.5892	2.5888	2.5884	1.0000	1.0000	1.0000
7	2.7671	2.7668	2.7665	2.7662	1.0000	1.0000	1.0000
8	3.1537	3.1531	3.1526	3.1520	0.9999	1.0000	1.0000
9	3.3451	3.3449	3.3448	3.3446	1.0000	1.0000	1.0000
10	-	-	-	-	-	-	-
11	4.6404	4.6397	4.6390	4.6382	1.0000	1.0000	1.0000
12	-	-	-	-	-	-	-

Table 5.7. CD-3 Position 3 MAC Comparison (West Girder Wall)

Mode Shape	Natural Frequency (Hz)				MAC (Average of U1, U2 and U3)		
	Baseline	25% Damage	50% Damage	75% Damage	25% Damage	50% Damage	75% Damage
1	0.9282	0.9266	0.9249	0.9233	1.0000	0.9989	0.9929
2	1.1951	1.1936	1.1922	1.1907	1.0000	1.0000	1.0000
3	1.3132	1.3122	1.3112	1.3103	1.0000	1.0000	1.0000
4	1.4821	1.4819	1.4816	1.4814	1.0000	1.0000	1.0000
5	2.1153	2.1144	2.1135	2.1125	1.0000	1.0000	1.0000
6	2.5896	2.5892	2.5888	2.5884	1.0000	1.0000	1.0000
7	2.7671	2.7668	2.7665	2.7662	1.0000	1.0000	1.0000
8	3.1537	3.1531	3.1526	3.1520	0.9999	1.0000	1.0000
9	3.3451	3.3449	3.3448	3.3446	1.0000	1.0000	1.0000
10	-	-	-	-	-	-	-
11	4.6404	4.6397	4.6390	4.6382	1.0000	1.0000	1.0000
12	-	-	-	-	-	-	-

Figure 5.9. Mode shape 1 comparison (CD-3)

5.2.3 Girder Damage

Girder damage was simulated by applying stiffness reductions of 25% and 75% to the segments adjacent to the stay tower (NP1 and SP1) and the two segments adjacent to stay cable 4 (roughly midspan). Damage to the concrete can occur from crack propagation or corrosion of the reinforcing steel. Segments close to a fixed support experience the greatest bending moment and shear force while the midspan segments tend to experience the greatest deflection. Therefore, these segments are very critical to the structure and should be investigated.

5.2.3.1 Case 1: NP1 and SP1 Segment Damage (GD-1)

The first girder damage case investigates damage occurring to the NP1 and SP1 segments only. For general members where the positive moment resistance is greater than the negative moment resistance, plastic hinges tend to develop close to fixed supports before developing at midspan. The effects of these plastic hinges are expected to affect the global behaviour of the structure since they effectively change the boundary conditions at fixed supports and cause them to act more like pin supports.

Damage was simulated by applying stiffness reductions of 25% and 75% to segments NP1 and SP1 only. Figure 5.10 shows the changes in natural frequency while Tables 5-8 to 5-10 show the average MAC values for each mode shape. At 25% damage, Modes 1 to 9 all experience decreases in natural frequency with percent differences ranging from -0.5% to -1.2% with Modes 5 (torsion) and 8 (second order bending) having the greatest percent differences of -1.2%. At 75% damage, Modes 1 to 8 show percent differences ranging from -2.7% to -6.6% with Modes 5 and 8 showing the greatest percent differences of -6.6% and -5.7% respectively. Mode 6 (bending) shows the lowest MAC for positions 2 and 3 with identical values of 0.9546 (25% damage) and 0.8557 (75%) damage.

Figure 5.11 shows the deflected shape of Mode 6 for each sensor position and each direction. The change in the U3 deflected shapes are essentially negligible. The U2 deflected shape inverts for spans 2 and 3 as damage increases. The U1 deflected shapes show little change for low damage percentages, but notable changes at 75% damage with the deflected shape shifting towards the positive direction.

The most sensitive mode shapes appear to be those with transverse movements and second order bending. In particular, mode 6 consistently shows low MAC values. The deterioration does not seem to change the deflected shape in the U3 direction a significant amount, but the greatest

71

damage effects are seen in the U2 and U1 direction. The sensitivity of the U2 deflections and not the U3 deflections could be due to the redundancy in the vertical direction from the stay cables, whereas the cables apply the same bracing effect in the U2 direction.

Despite having changes in natural frequency across several modes, the percent differences in natural frequency are still difficult to detect at a low level of damage. However, the relatively low MAC values of particular modes even at a low damage level, as well as characteristic changes in certain mode shapes indicate this damage case could be detected using modal identification methods.

Mode	25% Damage	75% Damage
1	-0.8%	-4.4%
2	-1.0%	-5.3%
3	-0.9%	-4.8%
4	-0.7%	-3.6%
5	-1.2%	-6.6%
6	-0.9%	-4.6%
7	-0.5%	-2.7%
8	-1.2%	-5.8%
9	-0.4%	-1.6%
10	-	-
11	0.0%	-0.1%
12	-	-
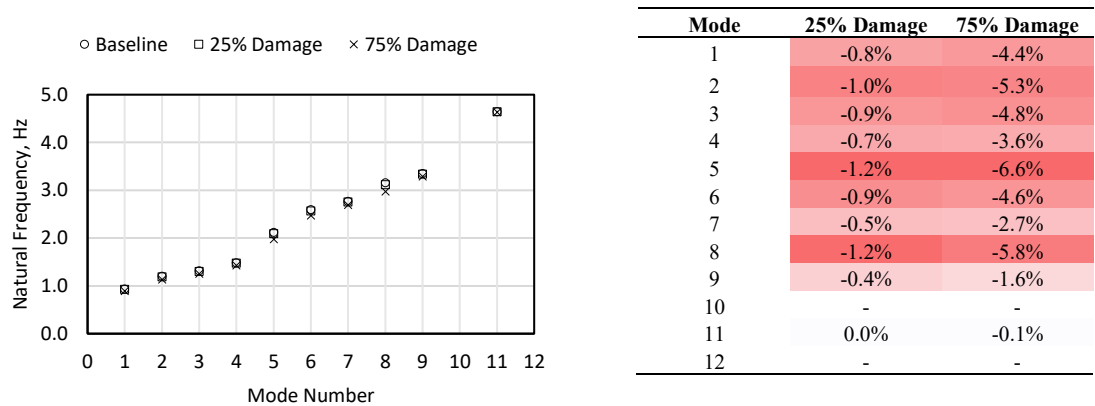
Figure 5.10. Natural frequency comparison with percent differences (GD-1)

Table 5.8. GD-1 Position 1 MAC Comparison (Top of Girder)

Mode Shape	Natural Frequency (Hz)			MAC (Average of U1, U2 and U3)	
	Baseline	25% Damage	75% Damage	25% Damage	75% Damage
1	0.9282	0.9212	0.8871	1.0000	0.9990
2	1.1951	1.1827	1.1316	0.9998	0.9941
3	1.3132	1.3019	1.2503	0.9999	0.9964
4	1.4821	1.4715	1.4282	0.9999	0.9963
5	2.1153	2.0890	1.9763	0.9966	0.9077
6	2.5896	2.5656	2.4695	0.9864	0.9501
7	2.7671	2.7523	2.6921	0.9910	0.9260
8	3.1537	3.1156	2.9723	0.9993	0.9864
9	3.3451	3.3325	3.2899	0.9985	0.9713
10	-	-	-	-	-
11	4.6404	4.6396	4.6352	0.9990	0.9762
12	-	-	-	-	-

Table 5.9. GD-1 Position 2 MAC Comparison (East Girder Wall)

Mode Shape	Natural Frequency (Hz)			MAC (Average of U1, U2 and U3)	
	Baseline	25% Damage	75% Damage	25% Damage	75% Damage
1	0.9282	0.9212	0.8871	1.0000	0.9992
2	1.1951	1.1827	1.1316	0.9999	0.9973
3	1.3132	1.3019	1.2503	0.9999	0.9971
4	1.4821	1.4715	1.4282	0.9999	0.9960
5	2.1153	2.0890	1.9763	0.9998	0.9955
6	2.5896	2.5656	2.4695	0.9546	0.8557
7	2.7671	2.7523	2.6921	0.9998	0.9942
8	3.1537	3.1156	2.9723	0.9979	0.9759
9	3.3451	3.3325	3.2899	0.9986	0.9562
10	-	-	-	-	-
11	4.6404	4.6396	4.6352	1.0000	0.9998
12	-	-	-	-	-

Table 5.10. GD-1 Position 3 MAC Comparison (West Girder Wall)

Mode Shape	Natural Frequency (Hz)			MAC (Average of U1, U2 and U3)	
	Baseline	25% Damage	75% Damage	25% Damage	75% Damage
1	0.9282	0.9212	0.8871	1.0000	0.9992
2	1.1951	1.1827	1.1316	0.9999	0.9973
3	1.3132	1.3019	1.2503	0.9999	0.9970
4	1.4821	1.4715	1.4282	0.9999	0.9960
5	2.1153	2.0890	1.9763	0.9998	0.9953
6	2.5896	2.5656	2.4695	0.9546	0.8557
7	2.7671	2.7523	2.6921	0.9998	0.9941
8	3.1537	3.1156	2.9723	0.9979	0.9759
9	3.3451	3.3325	3.2899	0.9986	0.9565
10	-	-	-	-	-
11	4.6404	4.6396	4.6352	1.0000	0.9998
12	-	-	-	-	-

Position 1 Sensors

Position 2 Sensors

Position 3 Sensors

Vertical, U3 (mm)

Transverse, U2 (*10⁻² mm)

Longitudinal, U1 (mm)

Distance from North abutment (mm)

Baseline — — 25% ········· 75%
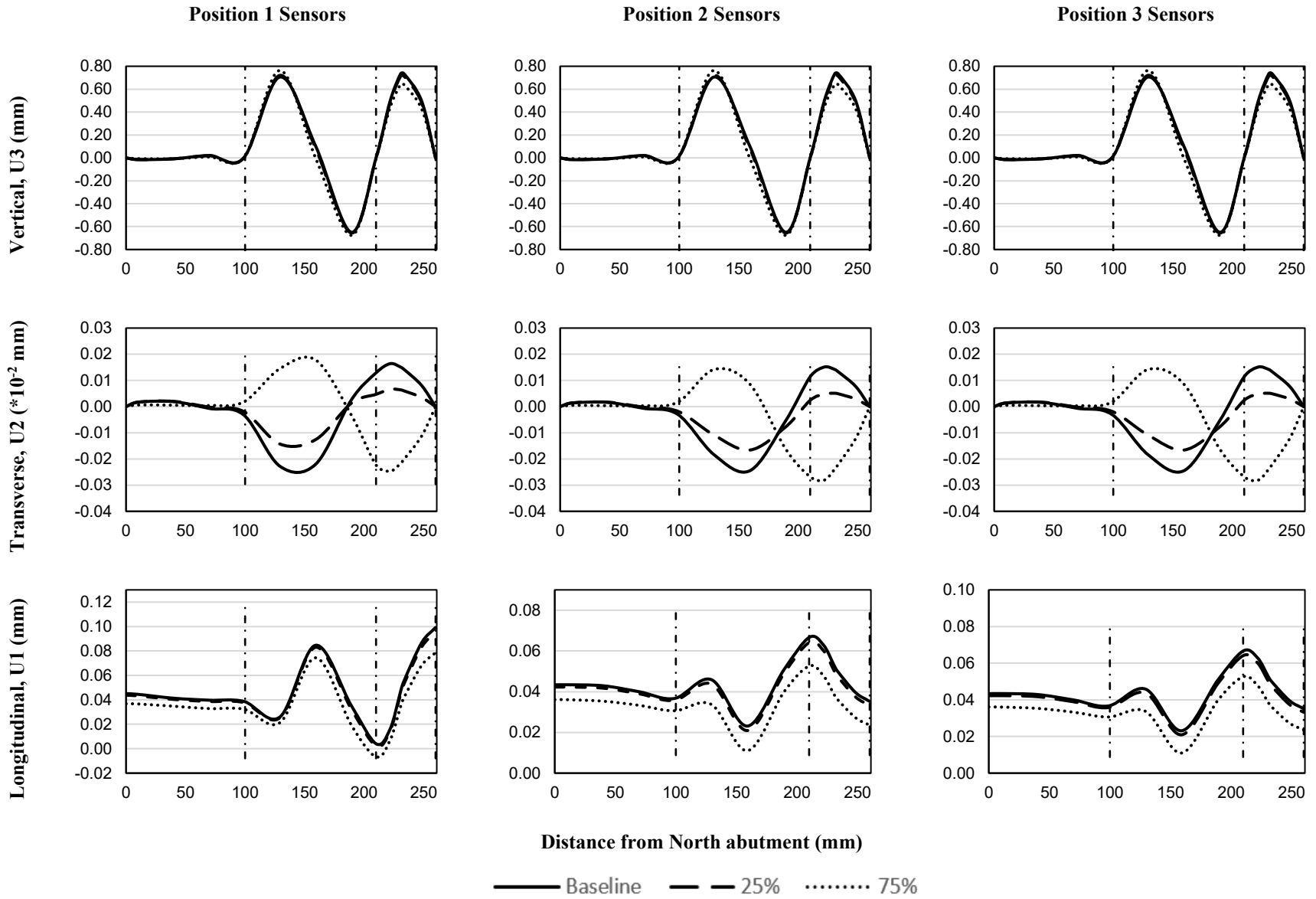
Figure 5.11. Mode shape 6 comparison (GD-1)

5.2.3.2 Case 2: NP1, SP1 NQ12 and SQ12 Segment Damage

The second girder damage case investigates damage to the midspan segments in addition to the NP1 and SP1 segments. A typical concrete collapse mechanism occurs when a plastic hinge forms near a fixed support and an additional plastic hinge forms near midspan after sufficient damage is reached. This damage case is expected to have a noticeable impact on global behaviour since a plastic hinge at midspan can behave like an internal hinge under additional loading and cause structural instability.

Damage was simulated by decreasing the stiffness of each segment by 25% and 75%. Figure 5.12 shows the change in natural frequencies and Tables 5-11 to 5-13 show the average MAC values for each mode shape. At 25% damage, mode shape 5 (torsion/transverse bending) shows the greatest decrease in natural frequency with a percent difference of -2.6%. Mode shapes 1 (bending) and 2 (bending) show percent differences just below -2% at the same damage. At 75% damage, dramatic changes in natural frequencies occur across modes 1, 2, 3, 5, 7, and 8. The largest differences occur in mode shapes 5, 1, and 2 with percent differences of -16.3%, -10.8%, and -9.8% respectively. At 25% damage, MAC values for position 1 are all close to 1. For positions 2 and 3 at 25% damage, mode 6 (bending) shows the greatest sensitivity with a MAC value of 0.9680 for both sensor positions. At 75% damage, Modes 7 and 11 show the greatest sensitivity to damage in position 1 with MAC values of 0.8936 and 0.7450 respectively. Mode 6 (second order bending) shows the greatest sensitivity for positions 2 and 3 with a MAC value of 0.8882 for both sensor positions.

The mode shapes corresponding to second order bending and transverse bending show the greatest sensitivity to this damage case, particularly in positions 2 and 3. Upon inspecting all of the mode shapes, deflections in the U2 direction seem to be most commonly impacted across all modes, but there are notable changes in the U3 deflected shape for modes 4 and 5.

Figure 5.13 shows the deflected shape of Mode 6 for damage case GD-2. The mode shapes for GD-2 are like those of GD-1 with the change in U2 direction being slightly more dramatic. The changes in natural frequency are larger compared to GD-1, but still may be difficult to detect at low damage levels. Relatively low MAC values and more obvious changes in mode shapes at a higher damage level indicate this damage case could be detected using modal identification methods.
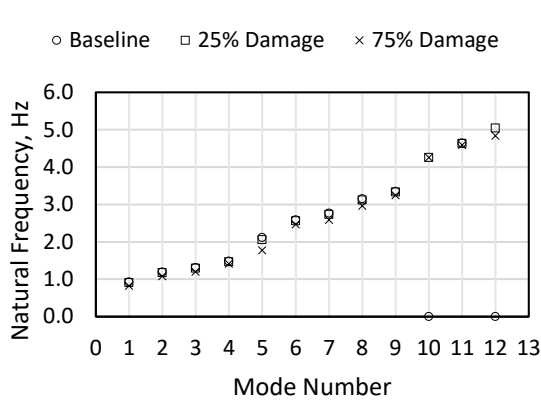
Mode	25% Damage	75% Damage
1	-1.7%	-10.8%
2	-1.8%	-9.8%
3	-1.3%	-8.3%
4	-0.9%	-4.4%
5	-2.6%	-16.3%
6	-0.9%	-4.8%
7	-1.1%	-6.6%
8	-1.2%	-6.0%
9	-0.5%	-2.9%
10	-	-
11	-0.2%	-1.2%
12	-	-

Figure 5.12. Natural frequency comparison with percent differences (GD-2)

Table 5.11. GD-2 Position 1 MAC Comparison (Top of Girder)

Mode Shape	Natural Frequency (Hz)			MAC (Average of U1, U2 and U3)	
	Baseline	25% Damage	75% Damage	25% Damage	75% Damage
1	0.9282	0.9127	0.8276	0.9999	0.9970
2	1.1951	1.1734	1.0781	0.9991	0.9616
3	1.3132	1.2967	1.2044	0.9995	0.9885
4	1.4821	1.4688	1.4171	0.9998	0.9875
5	2.1153	2.0610	1.7714	0.9982	0.9618
6	2.5896	2.5652	2.4662	0.9920	0.9499
7	2.7671	2.7362	2.5838	0.9921	0.8936
8	3.1537	3.1149	2.9649	0.9991	0.9835
9	3.3451	3.3280	3.2495	0.9989	0.9787
10	-	-	-	-	-
11	4.6404	4.6327	4.5867	0.9951	0.7450
12	-	-	-	-	-

Table 5-5.12. GD-2 Position 2 MAC Comparison (East Girder Wall)

Mode Shape	Natural Frequency (Hz)			MAC (Average of U1, U2 and U3)	
	Baseline	25% Damage	75% Damage	25% Damage	75% Damage
1	0.9282	0.9127	0.8276	0.9999	0.9976
2	1.1951	1.1734	1.0781	0.9998	0.9859
3	1.3132	1.2967	1.2044	0.9997	0.9886
4	1.4821	1.4688	1.4171	0.9997	0.9847
5	2.1153	2.0610	1.7714	0.9999	0.9968
6	2.5896	2.5652	2.4662	0.9680	0.8882
7	2.7671	2.7362	2.5838	0.9993	0.9769
8	3.1537	3.1149	2.9649	0.9976	0.9651
9	3.3451	3.3280	3.2495	0.9988	0.9669
10	-	-	-	-	-
11	4.6404	4.6327	4.5867	0.9997	0.9903
12	-	-	-	-	-

Table 5.13. GD-2 Position 3 MAC Comparison (West Girder Wall)

Mode Shape	Natural Frequency (Hz)			MAC (Average of U1, U2 and U3)	
	Baseline	25% Damage	75% Damage	25% Damage	75% Damage
1	0.9282	0.9127	0.8276	0.9999	0.9976
2	1.1951	1.1734	1.0781	0.9997	0.9859
3	1.3132	1.2967	1.2044	0.9997	0.9884
4	1.4821	1.4688	1.4171	0.9997	0.9847
5	2.1153	2.0610	1.7714	0.9999	0.9967
6	2.5896	2.5652	2.4662	0.9680	0.8882
7	2.7671	2.7362	2.5838	0.9993	0.9776
8	3.1537	3.1149	2.9649	0.9976	0.9651
9	3.3451	3.3280	3.2495	0.9988	0.9672
10	-	-	-	-	-
11	4.6404	4.6327	4.5867	0.9997	0.9889
12	-	-	-	-	-
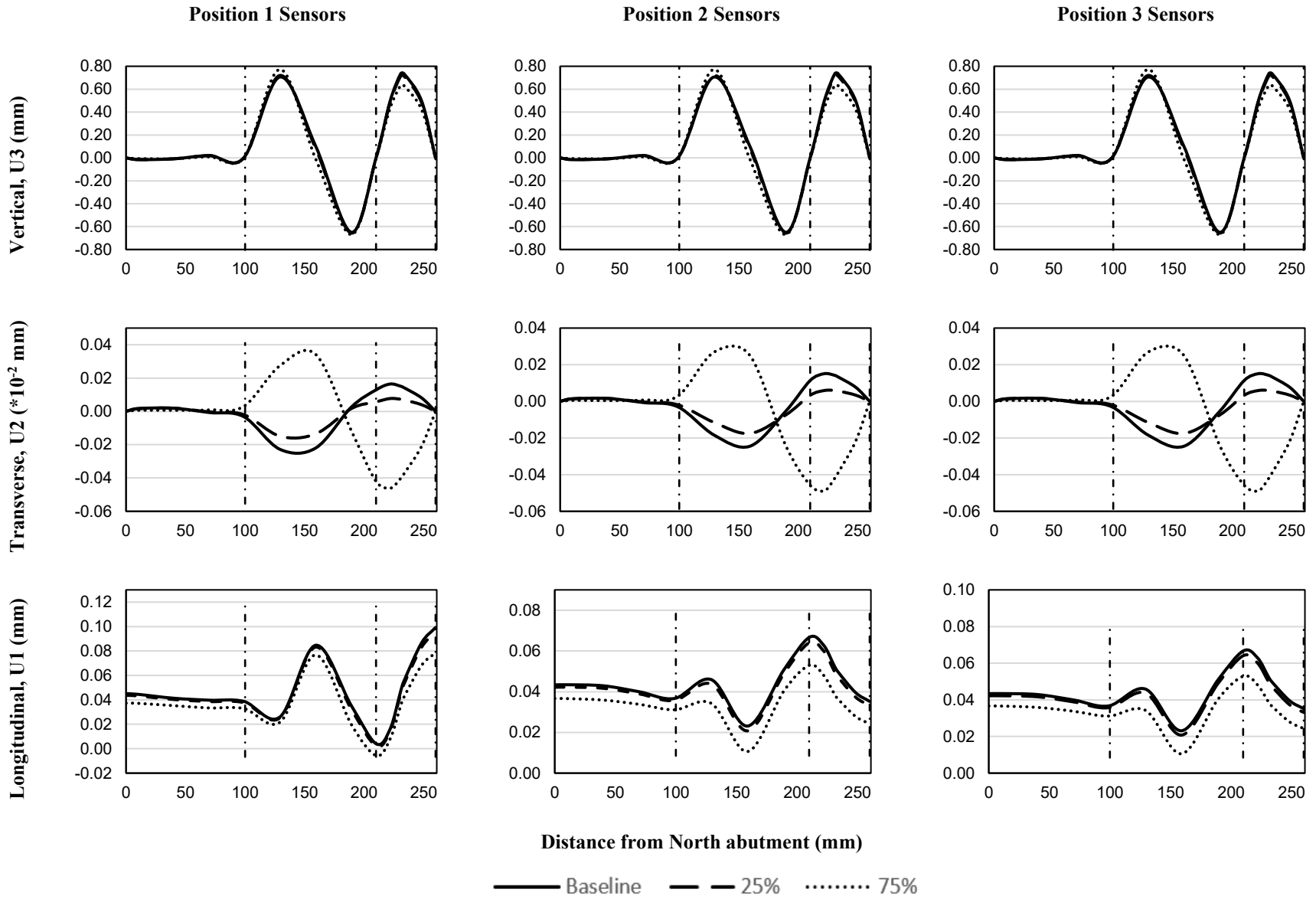
Figure 5.13. Mode shape 6 comparison (GD-2)

5.2.4 Post-tensioning Tendon Damage

Additional cases involving a 75% and 100% reduction in the tension of the draped tendons were also investigated. However, there was found to be virtually no change in modal properties from this damage case which implies this damage case may not be detectable using modal identification methods. A recommendation for detecting damage to post-tensioning tendons would be the installation of fibre-optic or vibrating-wire strain gauges to the tendons near the jacking point. Fibre-optic and vibrating-wire strain gauges are good for long-term monitoring applications and are discussed further in Section 2.5.2.

5.2.5 Tower Damage (TD)

Similar to the girder damage cases, a damage case simulating damage to the stay cable tower was investigated. Due to the height of the stay tower elements, they are exposed to environmental effects such as high winds which could apply significant lateral loads. The base of the stay tower just above the deck was chosen as this would be the point along the elements that experience the highest internal shear and bending moments. This damage case is not expected to have a major impact on the mode shapes of the girder due to the redundancies from the stay cables and post-tensioning tendons. Additionally, the cables apply significant normal force on the stay tower elements which would aid in decreasing deflections by limiting the formation and propagation of cracks.

Damage was simulated by applying a 25%, 50%, and 75% stiffness reduction to the base of the stay tower just above deck level. The stiffness reduction was applied to a length of $d_v \cot(\theta)$ (the length of a shear crack in a typical concrete element) for simplicity. Figure 5.14 shows the changes in natural frequency along with percent differences and Tables 5-14 to 5-16 show the average MAC values for each mode shape. Almost all of the natural frequencies have a percent difference close to 0.0% for each damage level except for mode 4 (longitudinal/bending) and mode 11 (tower bending) which have percent differences of -1.6% and -3.0%, respectively. It would seem Mode 1 for the TD case does not match well with Mode 1 from the baseline case as an odd pattern is detected where MAC value is closer to 1 as damage increases. However, this is an isolated case and the rest of the modes appear to follow the predicted pattern of decreasing MAC with increasing damage. The MAC values are all very close to 1, with the lowest value occurring for mode 11 (tower bending) in position 1 which has an average MAC of 0.9866 at 75% damage.

Upon inspecting the mode shapes, there do not seem to be any notable changes across all mode shapes for this damage case except for modes 4 (longitudinal/bending) and 11 (tower bending). Although this damage case seems to have characteristic and detectable changes to mode shape 11 at high damage levels (Figure 5.15), the low MAC values and small changes in natural frequency at would make this damage case difficult to detect with modal identification methods for low damage levels.

Mode	25% Damage	50% Damage	75% Damage
1	-0.2%	-0.4%	-0.7%
2	-0.1%	-0.1%	-0.2%
3	0.0%	0.0%	-0.1%
4	-0.5%	-0.9%	-1.6%
5	0.0%	0.0%	0.0%
6	0.0%	0.0%	-0.1%
7	0.0%	0.0%	0.0%
8	0.0%	0.0%	-0.1%
9	0.0%	0.0%	0.0%
10	-	-	-
11	0.0%	-0.8%	-3.0%
12	-	-	-
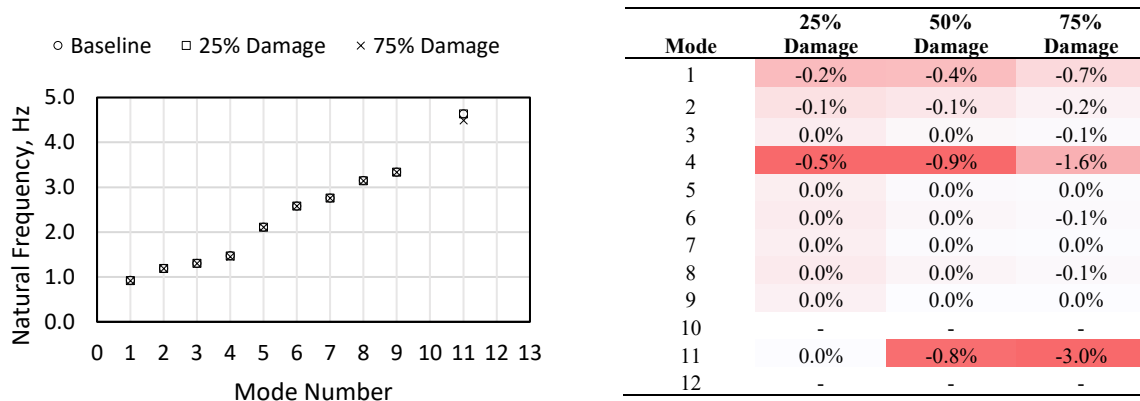
Figure 5.14. Natural frequency comparison with percent differences (TD)

Table 5.14. TD Position 1 MAC Comparison (Top of Girder)

Mode Shape	Natural Frequency (Hz)			MAC (Average of U1, U2 and U3)	
	Baseline	25% Damage	75% Damage	25% Damage	75% Damage
1	0.9282	0.9264	0.9216	0.9238	0.9996
2	1.1951	1.1944	1.1925	1.0000	0.9998
3	1.3132	1.3130	1.3125	1.0000	0.9999
4	1.4821	1.4745	1.4590	1.0000	0.9998
5	2.1153	2.1151	2.1147	0.9999	0.9996
6	2.5896	2.5891	2.5880	1.0000	0.9999
7	2.7671	2.7668	2.7667	1.0000	0.9999
8	3.1537	3.1530	3.1511	1.0000	0.9998
9	3.3451	3.3451	3.3450	1.0000	1.0000
10	-	-	-	-	-
11	4.6404	4.6424	4.4999	1.0000	0.9866
12	-	-	-	-	-

Table 5.15. TD Position 2 MAC Comparison (East Girder Wall)

Mode Shape	Natural Frequency (Hz)			MAC (Average of U1, U2 and U3)	
	Baseline	25% Damage	75% Damage	25% Damage	75% Damage
1	0.9282	0.9264	0.9216	0.9274	0.9996
2	1.1951	1.1944	1.1925	1.0000	1.0000
3	1.3132	1.3130	1.3125	1.0000	1.0000
4	1.4821	1.4745	1.4590	1.0000	0.9998
5	2.1153	2.1151	2.1147	1.0000	1.0000
6	2.5896	2.5891	2.5880	1.0000	0.9999
7	2.7671	2.7668	2.7667	1.0000	1.0000
8	3.1537	3.1530	3.1511	1.0000	0.9994
9	3.3451	3.3451	3.3450	1.0000	1.0000
10	-	-	-	-	-
11	4.6404	4.6424	4.4999	1.0000	0.9953
12	-	-	-	-	-

Table 5.16. TD Position 3 MAC Comparison (West Girder Wall)

Mode Shape	Natural Frequency (Hz)			MAC (Average of U1, U2 and U3)	
	Baseline	25% Damage	75% Damage	25% Damage	75% Damage
1	0.9282	0.9264	0.9216	0.9274	0.9996
2	1.1951	1.1944	1.1925	1.0000	1.0000
3	1.3132	1.3130	1.3125	1.0000	1.0000
4	1.4821	1.4745	1.4590	1.0000	0.9998
5	2.1153	2.1151	2.1147	1.0000	1.0000
6	2.5896	2.5891	2.5880	1.0000	0.9999
7	2.7671	2.7668	2.7667	1.0000	1.0000
8	3.1537	3.1530	3.1511	1.0000	0.9994
9	3.3451	3.3451	3.3450	1.0000	1.0000
10	-	-	-	-	-
11	4.6404	4.6424	4.4999	1.0000	0.9953
12	-	-	-	-	-

Figure 5.15. Mode shape 11 comparison (TD)

5.3 Chapter Summary

This chapter discussed the results of an eigenvector analysis performed using CSiBridge. The eigenvector analysis was used to determine the natural frequencies and mode shapes (modal properties) of the Tawatinâ bridge. A baseline case was modelled to represent a healthy structure and compared with various damage cases. Each damage case simulated damage to specific components of the bridge by reducing either the stiffness or tension of the component. In general, it seems that comparing mode shapes and MAC values is a more effective way of detecting damage than relying on natural frequency changes alone.

Stay cable damage (CD-3) and tower damage (TD) were found to have the least impact on the modal properties of the bridge. CD-3 had a slight impact on mode shape 1 (bending) in the U2 (transverse) direction. TD had a slight impact on mode 11 (tower bending) in all 3 directions. In both cases, the changes in mode shape may be difficult to detect even at high damage levels due to relatively minor changes in MAC and natural frequency values. This implies that other methods may be required to detect damage to these components (e.g., strain gauges on stay cables or additional accelerometers along stay towers).

Bearing damage (BD) and girder damage (GD-1 and GD-2) were found to have notable impacts on the modal properties of the bridge. BD had notable impacts on modal properties for all modes. In particular, deflections in the U1 (longitudinal) direction were the most sensitive due to the change in boundary conditions. GD-1 appeared to have the most impact on mode shapes with large transverse deflections and second order bending. GD-2 displayed a similar effect to GD-1 where the most notable impacts are in the U2 (transverse) direction for torsional and second-order bending modes. GD-2 also showed changes in mode shapes in the U3 (vertical) direction in the longitudinal and torsional modes. These cases had a relatively noticeable change in both MAC and natural frequency values which imply they would be easy to detect using a modal identification scheme.

Chapter 6 further investigates the damage cases discussed in this chapter with a dynamic analysis. A linear modal time history analysis with CSiBridge is used with the expected train loads. The accelerations at each sensor location are obtained and modal properties are determined using an SSI-Cov MATLAB script.

CHAPTER 6.   VEHICLE LOADING ANALYSIS

This chapter investigates the effects of different damage scenarios on the modal properties (e.g., mode shape and natural frequencies) of the Tawatinâ Bridge (Figure 6.1) under train loading. The train model used is discussed further in Section 6.1 and was applied to the model using a linear modal time-history analysis. The accelerations and displacements in the U3 (vertical), U2 (transverse), and U1 (longitudinal) directions were collected at various locations along the bridge which correspond to possible sensor locations (Figure 6.2). The mode shapes and natural frequencies of the bridge were calculated from the acceleration data using a Covariance-Driven Stochastic Subspace Integration (SSI-Cov) MATLAB script developed by Cheynet (2020).
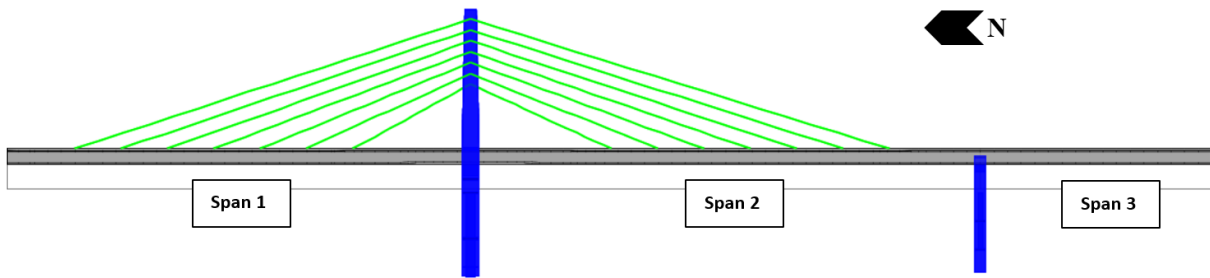
Figure 6.1. Tawatinâ bridge profile view showing span labels
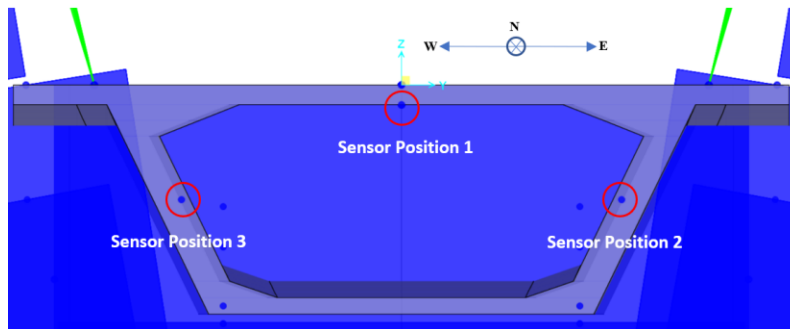
Figure 6.2. Box girder cross section showing sensor positions

6.1   Train Load Definition

The train loads were modelled as shown in Figure 6.3a and based on the Bombardier Flexity Freedom train specified for the Valley Line LRT (Figure 6.3b). Loads were estimated for an empty train with the assumption that empty trains would be used for testing in the field. The train load was applied at a speed of 30 kph (8.333m/s) on the south-bound lane for forty seconds with a time-step of 0.01s (100Hz). The speed was chosen based on the expected street speed of the train. A

forty second duration was chosen to allow the train to drive over the entire bridge, and a time step of 100 Hz was chosen to allow an error of 0.01 Hz.
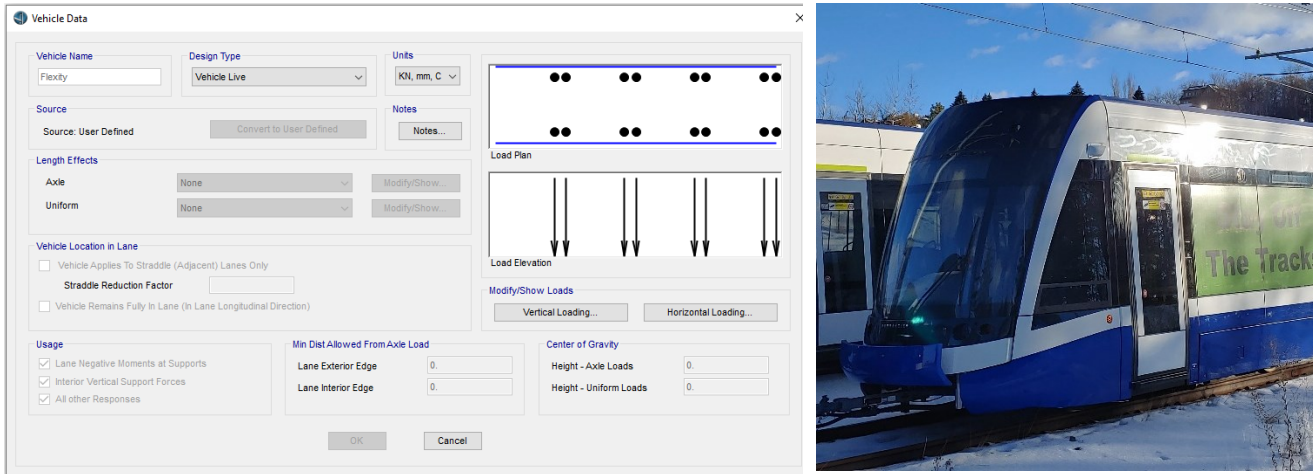
Figure 6.3. Flexity freedom train

6.2 Baseline Model

6.2.1 Modal Analysis

Before performing damage simulation, train loads were applied to three baseline models to determine the properties of a healthy structure. The three models had a varying number of nodes in the stay tower. Mode shapes of each model were compared using the Modal Assurance Criterion (MAC) to determine the most stable modes which could be used for damage detection. The results of the SSI-Cov algorithm implied that different modes and mode shapes were excited in the U3, U2, and U1 directions. Four stable modes each were found for the U3 and U2 directions. There were very low MAC values when comparing the mode shapes in the U1 direction between the three models which imply that the mode shapes detected are spurious and the mode shapes in the U1 direction may not actually be excited under this loading case. Therefore, the mode shapes in the U1 direction will not be considered in this chapter.

The natural frequencies and mode shapes for the baseline model are shown in Table 6-1. The natural frequencies of the detected mode shapes in the U3 direction are lower than those of the U2 direction. It appears that this loading case applies greater energy to the transverse direction compared to the vertical direction since mode shapes with higher natural frequencies are excited in the transverse direction compared to the vertical direction. It is difficult to comment on what the dominant behaviour is for each mode shape since mode shapes in either direction do not correlate with each other.

Table 6.1. Baseline natural frequencies for modes in U3 and U2 direction

Mode	U3 Direction	U2 Direction
1	0.6673	1.3080
2	0.9401	3.4050
3	1.2080	4.7206
4	2.7405	4.8188

6.2.2 Time History Deflections

Displacement envelopes were also generated and compared to illustrate changes in response as damage increases. The displacement envelopes for the Position 1 sensors were representative of the general structural behaviour. Figure 6.4 shows the baseline displacement envelopes for the U3 and U2 directions. In the U3 direction, the max positive displacement is 2.11 mm and occurs on Span 3 while the max negative displacement is -11.36 mm and occurs on Span 2. In the U2 direction, the max positive displacement is essentially zero while the max negative displacement is -0.246 mm and occurs on span 2. It is interesting to note that Pier 2 is much more flexible in the transverse direction compared to Pier 1 as seen on the U2 displacement envelope. This is likely due to the following factors: the support condition on Pier 2 is not fixed, spans 2 and 3 are continuous, and Pier 2 is more flexible than Pier 1.
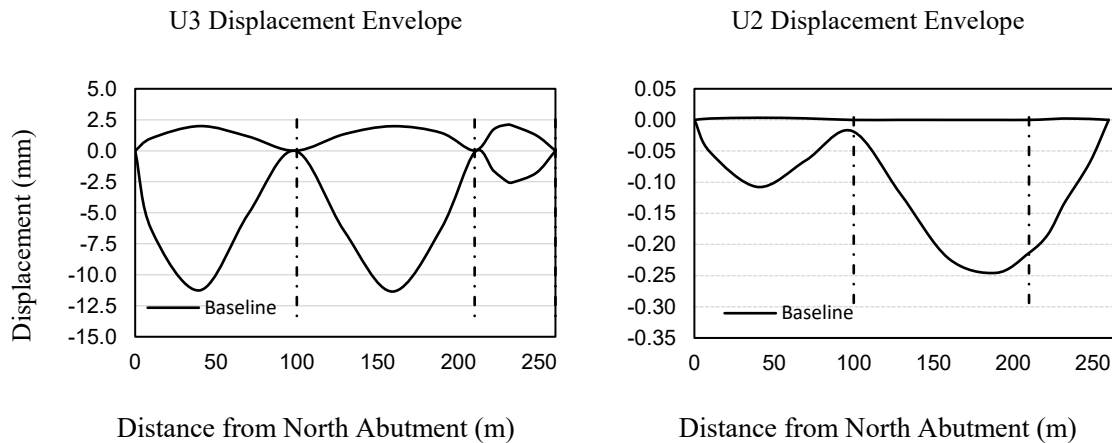
Figure 6.4. Baseline case displacement envelope

6.3 Damage Simulation

The damage cases are discussed in Section 5.2 but repeated here for convenience. Damage cases are divided into four categories: bearing damage, stay cable damage, girder damage, and tower damage. Reasoning for each damage case category was discussed in Chapter 5 but summarized in the following sections. Table 6-2 and Figure 6.5 summarize damage cases considered. Damage cases were compared to the baseline based on natural frequencies, MAC values, mode shapes, and

displacement envelopes. MAC values were used as an objective measure of which mode shapes were the most sensitive to damage.

Table 6.2. Damage simulation scheme

Damage ID	Category	Location	Change
BD	Bearing Damage	North Abutment; Pier 2 Support	Change roller supports to pin supports.
CD-1	Stay Cable Damage	Cable 7	Tension reduction: 25%, 50% and 75%
CD-2	Stay Cable Damage	Cables 1-6	Tension reduction: 25%, 50% and 75%
CD-3	Stay Cable Damage	All Cables	Stiffness reduction: 25%, 50% and 75%
GD-1	Girder Damage	Segment SP1 and NP1	Stiffness reduction: 25% and 75%
GD-2	Girder Damage	Segment SP1, NP1, SQ12, and NQ12	Stiffness reduction: 25% and 75%
TD	Tower Damage	Stay Tower at deck level	Stiffness reduction: 25% and 75%
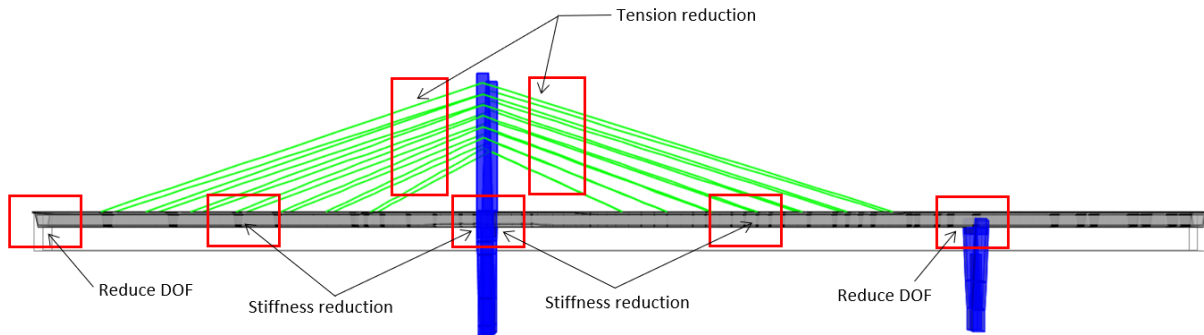
Figure 6.5. Damage simulation scheme

6.3.1 Bearing Damage (BD)

The bearing damage case is described more in Section 5.2.1 but summarized for convenience. Bearings can be damaged over time from debris or wearing on the bearing surfaces which leads to increased friction and potential reductions in degrees of freedom. As such, the damage was simulated by changing roller bearings to pin supports in the model to reduce degrees of freedom.

Figure 6.6 and 6.7 show changes in natural frequency while Tables 6-3 and 6-4 show the average MAC values for each mode shape. The SSI-Cov algorithm detected 7 modes in the U3 (vertical) direction and 8 modes in the U2 (transverse) direction. Due to the relatively low MAC values, modes were matched based on natural frequency which led to 4 useful modes in the U3 direction and 3 useful modes in the U2 direction.

Modes typically showed a slight increase in natural frequency which denotes an increase in stiffness. In the U3 direction, Modes 2 and 3 showed the greatest change in natural frequency with percent differences of 15.0% and 3.8% respectively. In the U2 direction, Mode 1 shows the greatest change in natural frequency with a percent difference of 4.6%. In the U3 direction, average MAC values ranged from 0.7670 to 0.9866 with Mode 3 having the greatest sensitivity to damage. Modes in the U2 direction were much more sensitive to this damage type with average MAC values ranging from 0.1025 to 0.7543.

Figure 6.8 shows the governing mode shapes in the U3 and U2 directions and Figure 6.9 shows the displacement envelopes in the U3 and U2 directions. In the U3 direction, Mode 3 shows a notable change in mode shape for spans 2 and 3. In the U2 direction, all modes appeared to match poorly with the baseline modes likely due to the added restraints in the U1 and U2 directions. The displacement envelope shows a decrease in span 1 and 2 deflections in the U3 direction, and a decrease in deflections at all spans in the U2 direction.

Natural frequency changes tend to be more detectable in the U3 direction than the U2 direction which implies that this damage may affect natural frequencies at lower energy modes most. However, when inspecting the mode shapes and MAC values, the mode shapes in the U2 direction appeared to be significantly more impacted by the additional restraints. This appears to be intuitive since the U2 direction sees additional restraints from this damage case while the U3 direction does not. Overall, the results imply that this damage case has a notable impact on the modal properties of the bridge and could be detected using modal identification methods under this loading scheme.
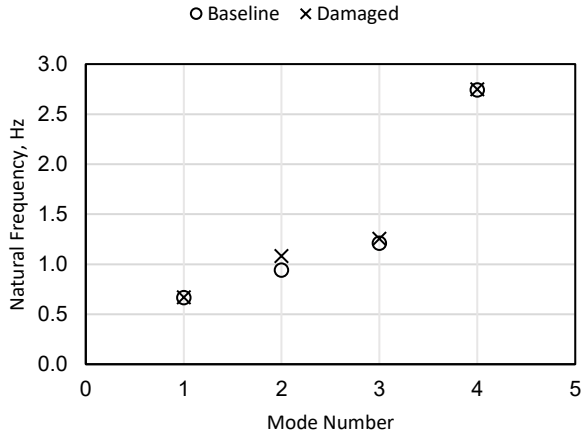
Mode	Baseline	Damaged	Percent difference
1	0.6673	0.6700	0.4%
2	0.9401	1.0811	15.0%
3	1.2080	1.2539	3.8%
4	2.7405	2.7488	0.3%
5	-	-	-
6	-	-	-
7	-	-	-
8	-	-	-
9	-	-	-
10	-	-	-
11	-	-	-
12	-	-	-

Figure 6.6. U3 direction natural frequency comparison with percent differences (BD)
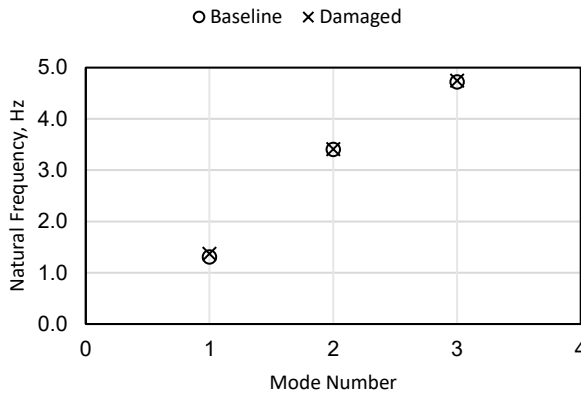
Mode	Baseline	Damaged	Percent difference
1	1.3080	1.3687	4.6%
2	3.4050	3.4074	0.1%
3	4.7206	4.7436	0.5%
4	-	-	-
5	-	-	-
6	-	-	-
7	-	-	-
8	-	-	-
9	-	-	-
10	-	-	-
11	-	-	-
12	-	-	-

Figure 6.7. U2 direction natural frequency comparison with percent differences (BD)

Table 6.3. BD U3 direction MAC comparison

Mode Shape	Natural Frequency (Hz) (Average of P1, P2, P3)		MAC			
	Baseline	Damaged	P1	P2	P3	Average
1	0.6673	0.6700	0.9883	0.9883	0.9892	0.9886
2	0.9401	1.0811	0.9733	0.9739	0.9715	0.9729
3	1.2080	1.2539	0.7662	0.7670	0.7677	0.7670
4	2.7405	2.7488	0.8553	0.8677	0.8360	0.8530
5	-	-	-	-	-	-
6	-	-	-	-	-	-
7	-	-	-	-	-	-
8	-	-	-	-	-	-
9	-	-	-	-	-	-
10	-	-	-	-	-	-
11	-	-	-	-	-	-
12	-	-	-	-	-	-

Table 6.4. BD U2 direction MAC comparison

| Mode Shape | Natural Frequency (Hz) (Average of P1, P2, P3) | | MAC Values | | | |
	Baseline	Damaged	P1	P2	P3	Average
1	1.3080	1.3687	0.7535	0.7548	0.7548	0.7543
2	3.4050	3.4074	0.1541	0.1658	0.1658	0.1619
3	4.7206	4.7436	0.0928	0.1073	0.1073	0.1025
4	4.8188	-	-	-	-	-
5	-	-	-	-	-	-
6	-	-	-	-	-	-
7	-	-	-	-	-	-
8	-	-	-	-	-	-
9	-	-	-	-	-	-
10	-	-	-	-	-	-
11	-	-	-	-	-	-
12	-	-	-	-	-	-

Vertical U3 (mm) (Mode 3)   **Transverse U2 (mm) (Mode 1)**

Figure 6.8. Governing mode shape comparison (BD) with vertical dashed lines indicating support locations.

U3 Displacement Envelope   **U2 Displacement Envelope**

Figure 6.9. Displacement envelope comparisons (BD) with vertical dashed lines indicating support locations.

91

6.3.2　Stay Cable Damage

The stay cable damage case is described in detail in Section 5.2.2 but summarized here for convenience. Stay cables (Figure 6.10) increase redundancy by allowing various possible paths to transfer loads into the supports. However, they can be damaged from corrosion or wearing of materials due to fatigue over time which could lead to relaxation. CD-1 and CD-2 were found to have negligible changes to the modal properties and displacement envelopes so only damage case CD-3 is discussed in this section.
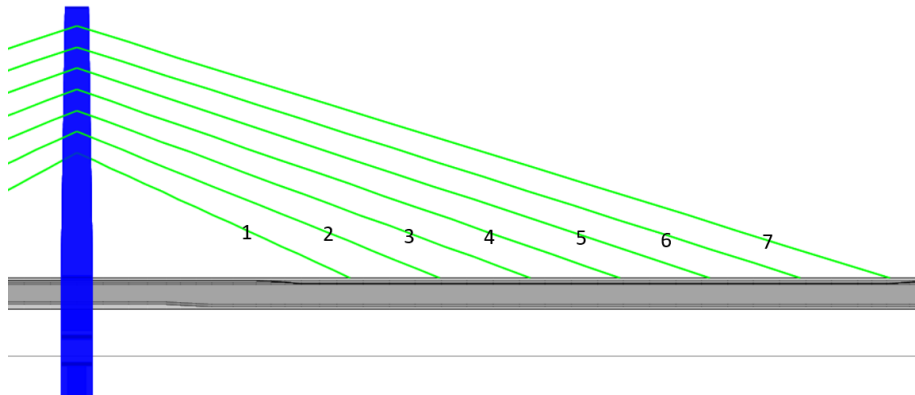
Figure 6.10. Layout of stay cables with labels shown

Damage was simulated by applying tension reductions of 25%, 50%, and 75% (denoted as 25% damage, 50% damage, and 75% damage). Figure 6.11 and 6.12 show changes in natural frequency while Tables 6-5 and 6-6 show the average MAC values for each mode shape. The SSI-Cov algorithm detected 4 modes in the U3 direction and 4 modes in the U2 direction for all damage levels.

All modes show negligible changes in natural frequency in both the U2 and U3 directions. In the U3 direction, mode shape 2 appears to be the most sensitive to this damage type MAC values of 0.9859, 0.9077, and 0.9138 for 25%, 50%, and 75% damage respectively. The rest of the mode shapes, including those in the U2 direction, are all essentially 1.000 which implies they are not sensitive to this damage type.

Figure 6.13 shows the governing mode shapes in the U3 and U2 directions and Figure 6.14 shows the displacement envelopes in the U3 and U2 directions. In the U3 direction, Mode 2 shows a gradual change in span 1 deflection as damage increases. In the U2 direction, mode 1 shows a slight change in span 1 which would be difficult to detect in practice. The displacement envelopes for both the U3 and U2 direction show no change from this damage case. Although the changes in

mode shape 2 in the U3 direction appear to be noticeable even at low levels of damage, the negligible changes in natural frequency and MAC values show that this damage case may not be detectable using modal identification methods under this load case.

Mode	25% Damage	50% Damage	75% Damage
1	0.0%	0.0%	0.0%
2	-0.1%	-0.2%	-0.2%
3	-0.1%	-0.3%	-0.4%
4	0.0%	0.0%	0.0%
5	-	-	-
6	-	-	-
7	-	-	-
8	-	-	-
9	-	-	-
10	-	-	-
11	-	-	-
12	-	-	-
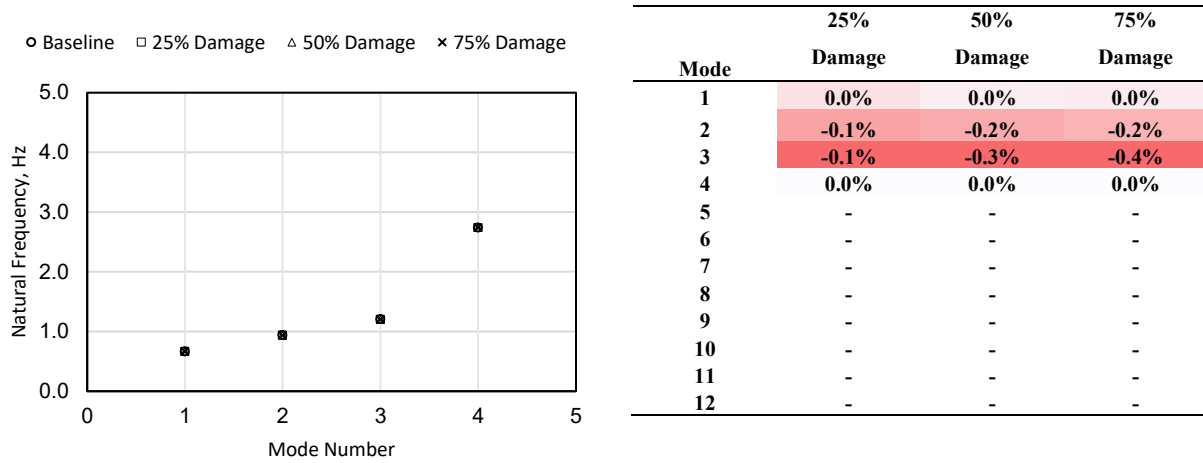
Figure 6.11. U3 direction natural frequency comparison with percent differences (CD-3)

Mode	25% Damage	50% Damage	75% Damage
1	0.0%	-0.1%	-0.1%
2	0.0%	0.0%	0.0%
3	0.0%	0.0%	0.0%
4	0.0%	0.0%	0.0%
5	-	-	-
6	-	-	-
7	-	-	-
8	-	-	-
9	-	-	-
10	-	-	-
11	-	-	-
12	-	-	-

Figure 6.12. U2 direction natural frequency comparison with percent differences (CD-3)

Table 6.5. CD-3 U3 direction MAC comparison

Mode Shape	Natural Frequency (Hz) (Average of P1, P2, P3)				MAC (Average of P1, P2, P3)		
	Baseline	25% Damage	50% Damage	75% Damage	25% Damage	50% Damage	75% Damage
1	0.6673	0.6672	0.6672	0.6670	1.0000	0.9999	0.9998
2	0.9401	0.9394	0.9387	0.9382	0.9859	0.9077	0.9138
3	1.2080	1.2064	1.2047	1.2031	1.0000	1.0000	1.0000
4	2.7405	2.7406	2.7406	2.7405	0.9999	0.9999	0.9999
5	-	-	-	-	-	-	-
6	-	-	-	-	-	-	-
7	-	-	-	-	-	-	-
8	-	-	-	-	-	-	-
9	-	-	-	-	-	-	-
10	-	-	-	-	-	-	-
11	-	-	-	-	-	-	-
12	-	-	-	-	-	-	-

Table 6.6. CD-3 U2 direction MAC comparison

Mode Shape	Natural Frequency (Hz)				MAC (Average of U1, U2 and U3)		
	Baseline	25% Damage	50% Damage	75% Damage	25% Damage	50% Damage	75% Damage
1	1.3080	1.3075	1.3071	1.3067	0.9997	0.9989	0.9975
2	3.4050	3.4044	3.4043	3.4043	0.9998	0.9998	0.9997
3	4.7206	4.7205	4.7205	4.7205	0.9998	0.9998	0.9998
4	4.8188	4.8188	4.8184	4.8184	0.9996	0.9995	0.9993
5	-	-	-	-	-	-	-
6	-	-	-	-	-	-	-
7	-	-	-	-	-	-	-
8	-	-	-	-	-	-	-
9	-	-	-	-	-	-	-
10	-	-	-	-	-	-	-
11	-	-	-	-	-	-	-
12	-	-	-	-	-	-	-

Vertical U3 (mm) (Mode 2) **Transverse U2 (mm) (Mode 1)**

Position 1 / Position 2 / Position 3

Baseline, f_n=0.9402; CD3 (25%), f_n=0.9394; CD3 (75%), f_n=0.9383
Baseline, f_n=1.308; CD3 (25%), f_n=1.3075; CD3 (75%), f_n=1.3067

Distance from North Abutment (m)   **Distance from North Abutment (m)**

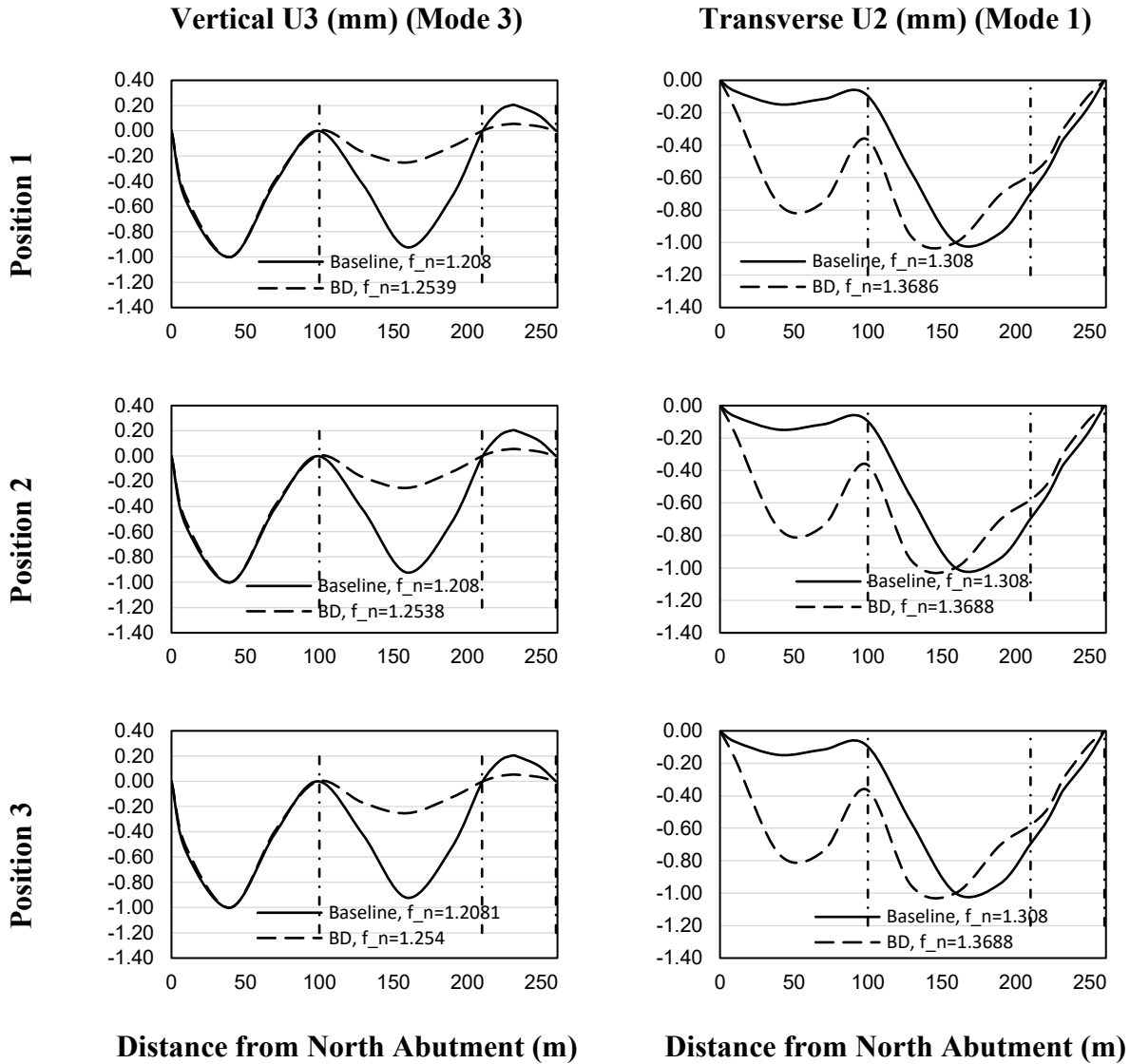*Figure 6.13. Governing mode shape comparison (CD-3) with vertical dashed lines indicating support locations.*

U3 Displacement Envelope
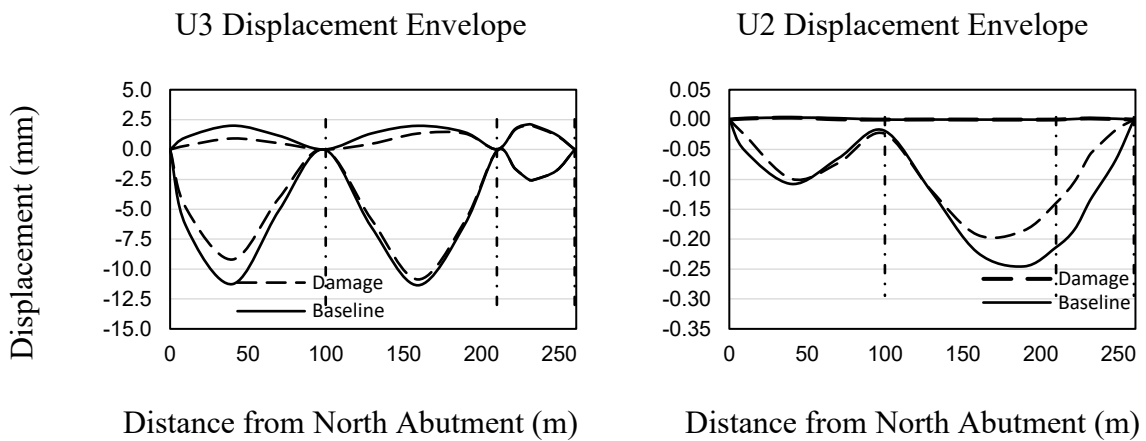
U2 Displacement Envelope
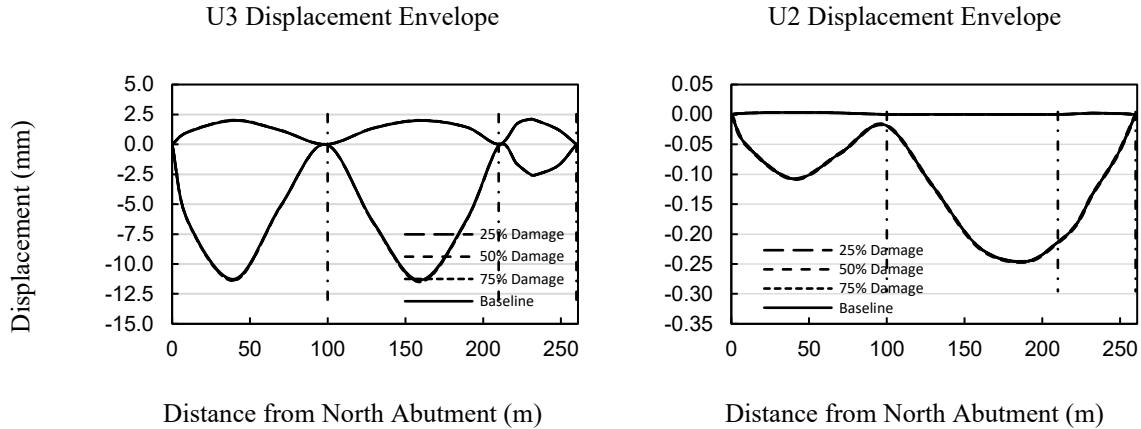
Figure 6.14. Displacement envelope comparisons (CD-3) with vertical dashed lines indicating support locations.

6.3.3   Girder Damage

The girder damage case is described in detail in Section 5.2.3 but repeated here for convenience. Girder damage was simulated by applying stiffness reductions of 25% and 75% to the segments adjacent to the stay tower (NP1 and SP1) and the two segments adjacent to stay cable 4 (roughly midspan). Damage to the concrete girder can occur from cracking of concrete or corrosion of the reinforcing steel.

6.3.3.1   Case 1: NP1 and SP1 Segment Damage (GD-1)

The damage case GD-1 investigates damage applied to the NP1 and SP1 segments only (Figure 6.5). For general flexural members where the positive moment resistance is greater than the negative moment resistance, plastic hinges tend to develop close to fixed supports before developing at midspan. These plastic hinges are expected to impact the global behaviour of the structure since they effectively change the boundary conditions at fixed supports and increase degrees of freedom.

Damage was simulated by applying stiffness reductions of 25% and 75% to segments NP1 and SP1 only. Figure 6.15 and 6.16 show the changes in natural frequency while Tables 6-7 to 6-8 show the average MAC values for each mode shape. The SSI-Cov algorithm detected 4 modes in the U3 direction and 4 modes in the U2 direction at 25% damage. Four modes were detected in the U3 direction and only 3 modes were detected in the U2 direction at 75% damage.

In the U3 (vertical) direction, all modes show decreases in natural frequency for 25% damage with percent differences ranging from -0.2% to -1.4%. At 75% damage, modes 2 and 3 in the U3 direction show notable decreases in natural frequency with percent differences of -5.1% and -6.5%, respectively. Mode shape 2 shows the greatest sensitivity at 25% damage with a MAC value of

95

0.9156, and mode shape 1 shows the greatest sensitivity at 75% damage with a MAC value of 0.3568. Mode shapes in the U2 (lateral) direction have negligible changes in natural frequency for 25% damage with the greatest decrease being -0.5% for mode 1. At 75% damage, mode shapes in the U2 direction still show very little changes in natural frequency with mode 1 having the greatest percent difference of -2.6%. Mode shapes in the U2 direction do not show much sensitivity to damage with MAC values ranging from 0.9711 to 0.9998 for 25% damage and 0.9298 to 0.9992 for 75% damage.

Figure 6.17 shows the governing mode shapes in the U3 and U2 directions and Figure 6.18 shows the displacement envelopes in the U3 and U2 directions. In the U3 direction, Mode 3 shows a gradual change in span 2 and span 3 deflections as damage increases. In the U2 direction, Mode 2 shows a gradual change in span 1 and span 2 deflections as damage increases. The displacement envelope shows an increase in max midspan displacement for spans 1 and 2 in the negative and positive U3 directions as damage increases. There is also an increase in max displacement in the negative U2 direction as damage increases which is most notable on span 2.

Natural frequency changes tend to be more detectable in the U3 direction than the U2 direction especially at low levels of damage which implies that this type of damage may affect the natural frequencies of the lower energy modes the most. In both directions, there is a notable change in the mode shapes. Changes may be difficult to detect at low damage levels, but significantly easier to detect at higher damage levels which implies that this damage case could be detected using modal identification methods under this loading scheme.

Mode	25% Damage	75% Damage
1	-1.0%	-0.4%
2	-0.8%	-5.1%
3	-1.4%	-6.5%
4	-0.2%	-0.6%
5	-	-
6	-	-
7	-	-
8	-	-
9	-	-
10	-	-
11	-	-
12	-	-

Figure 6.15. U3 direction natural frequency comparison with percent difference (GD-1)

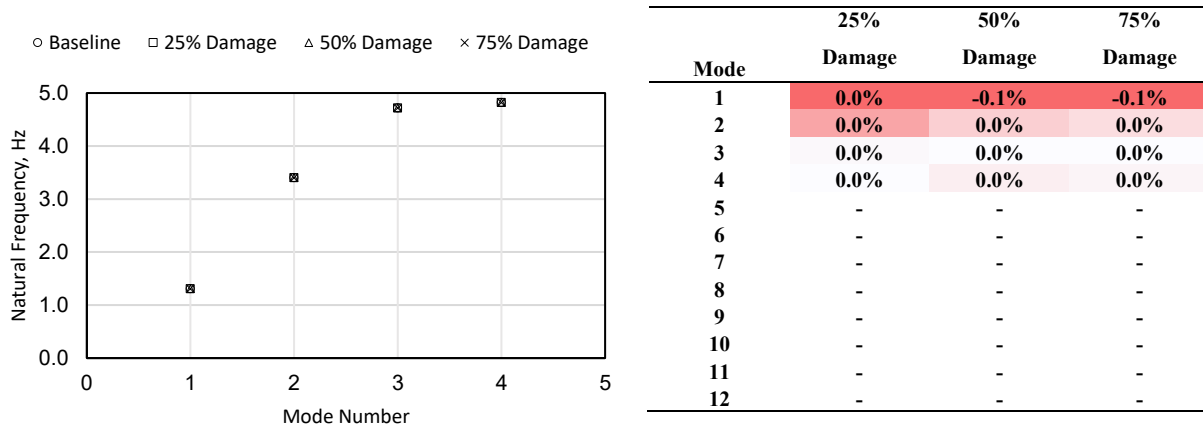| Mode	25% Damage	75% Damage
1	-0.5%	-2.6%
2	0.1%	0.2%
3	0.0%	0.2%
4	0.0%	-
5	-	-
6	-	-
7	-	-
8	-	-
9	-	-
10	-	-
11	-	-
12	-	-
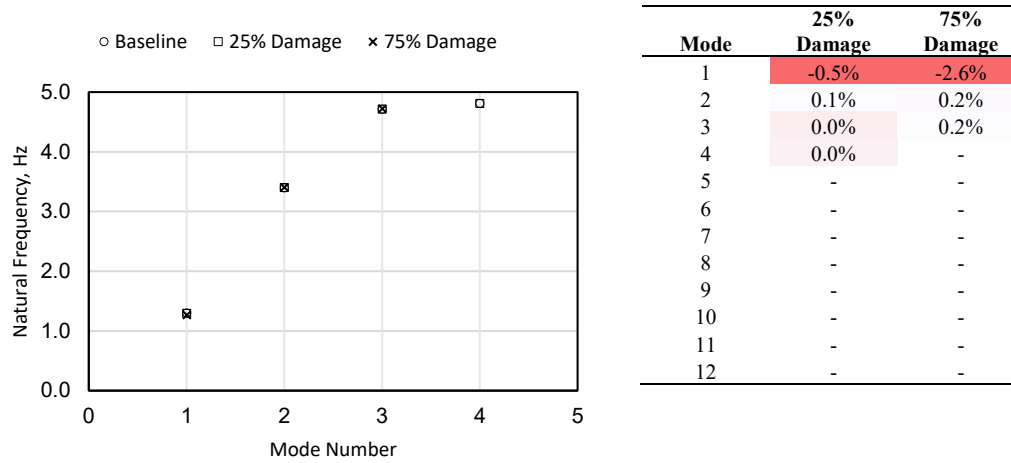
Figure 6.16. U2 direction natural frequency comparison with percent differences (GD-1)

Table 6.7. GD-1 U3 direction MAC comparison

Mode Shape	Natural Frequency (Hz) (Average of P1, P2, P3)			MAC (Average of P1, P2, P3)	
	Baseline	25% Damage	75% Damage	25% Damage	75% Damage
1	0.6673	0.6608	0.6645	0.9951	0.3568
2	0.9401	0.9331	0.8919	0.9156	0.8516
3	1.2080	1.1908	1.1296	0.9986	0.9884
4	2.7405	2.7355	2.7251	0.9987	0.7907
5	-	-	-	-	-
6	-	-	-	-	-
7	-	-	-	-	-
8	-	-	-	-	-
9	-	-	-	-	-
10	-	-	-	-	-
11	-	-	-	-	-
12	-	-	-	-	-

Table 6.8. GD-1 U2 direction MAC comparison

Mode Shape	Natural Frequency (Hz) (Average of P1, P2, P3)			MAC (Average of P1, P2, P3)	
	Baseline	25% Damage	75% Damage	25% Damage	75% Damage
1	1.3080	1.3019	1.2736	0.9711	0.9807
2	3.4050	3.4068	3.4117	0.9946	0.9298
3	4.7206	4.7206	4.7319	0.9998	0.9992
4	4.8188	4.8194	-	0.9996	-
5	-	-	-	-	-
6	-	-	-	-	-
7	-	-	-	-	-
8	-	-	-	-	-
9	-	-	-	-	-
10	-	-	-	-	-
11	-	-	-	-	-
12	-	-	-	-	-

Vertical U3 (mm) (Mode 3)

Transverse U2 (mm) (Mode 1)

Position 1

Position 2

Position 3

Baseline, f_n=1.208
GD1 (25%), f_n=1.1908
GD1 (75%), f_n=1.1296

Baseline, f_n=1.208
GD1 (25%), f_n=1.1908
GD1 (75%), f_n=1.1294

Baseline, f_n=1.2081
GD1 (25%), f_n=1.1907
GD1 (75%), f_n=1.1298

Baseline, f_n=3.405
GD1 (25%), f_n=3.4065
GD1 (75%), f_n=3.4119

Baseline, f_n=3.405
GD1 (25%), f_n=3.4069
GD1 (75%), f_n=3.4117

Baseline, f_n=3.405
GD1 (25%), f_n=3.4069
GD1 (75%), f_n=3.4117

Distance from North Abutment (m)

Distance from North Abutment

Figure 6.17. Governing mode shape comparison (GD-1) with vertical dashed lines indicating support locations.

U3 Displacement Envelope

U2 Displacement Envelope

Displacement (mm)

25% Damage
75% Damage
Baseline

25% Damage
75% Damage
Baseline

Distance from North Abutment (m)

Distance from North Abutment (m)

Figure 6.18. Displacement envelope comparison (GD-1) with vertical dashed lines indicating support locations.

98

6.3.3.2 Case 2: NP1, SP1, NQ12 and SQ12 Segment Damage

Damage was simulated by applying stiffness reductions of 25% and 75% to segments NP1, SP1, NQ12, and SQ12 which correspond to the segments adjacent to the stay tower (Pier 1) and the middle stay cables (roughly midspan). Figure 6.19 and 6.20 show the changes in natural frequency while Tables 6-9 to 6-10 show the average MAC values for each mode shape. The SSI-Cov algorithm detected 4 modes in the U3 direction and 3 modes in the U2 direction at 25% damage. At 75% damage, only 1 mode was detected in the U3 direction and 2 modes were detected in the U2 direction.

In the U3 (vertical) direction, all modes show decreases in natural frequency for 25% damage with percent differences ranging from -0.2% to -2.1%. At 75% damage, only mode 4 is detected and shows a percent difference of -0.6%. Mode shape 2 shows the greatest sensitivity to damage at 25% damage with a MAC value of 0.7653 with the rest of the values being close to 1.000. At 75% damage, only mode shape 4 can be detected which drops from a MAC value of 0.9989 to 0.8666 as damage increases. Mode shapes in the U2 (lateral) direction have negligible changes in natural frequency for 25% damage with the greatest percent difference being -0.5% for mode 1. At 75% damage, mode 1 shows the greatest percent difference again with a value of -1.3%. Mode 1 in the U2 direction also appears to be the most sensitive to damage with MAC values of 0.9595 at 25% damage and 0.8888 at 75% damage. The rest of the MAC values in the U2 direction are very close to 1.000.

Figure 6.21 shows the governing mode shapes in the U3 and U2 directions and Figure 6.22 shows the displacement envelopes in the U3 and U2 directions. In the U3 direction, Mode 4 shows a notable change in deflection at high levels of damage on span 1. There is a slight change in deflection at low levels of damage, but it would be difficult to detect in practice. In the U2 direction, Mode 1 shows a gradual change in the span 1 deflection which is notable at even low levels of damage. The displacement envelope shows an increase in max midspan displacement in the positive and negative U3 directions as damage increases. There is also an increase in max displacement in the negative U2 direction as damage increases which is most notable on span 2.

Similar to the GD-1 case, natural frequency changes tend to be more detectable in the U3 direction than the U2 direction especially at low levels of damage which implies that this type of damage may affect the natural frequencies of the lower energy modes the most. In both directions, there is a notable change in the mode shapes. Changes may be difficult to detect at low damage

levels, but significantly easier to detect at higher damage levels which implies that this damage case could be detected using modal identification methods under this loading scheme.
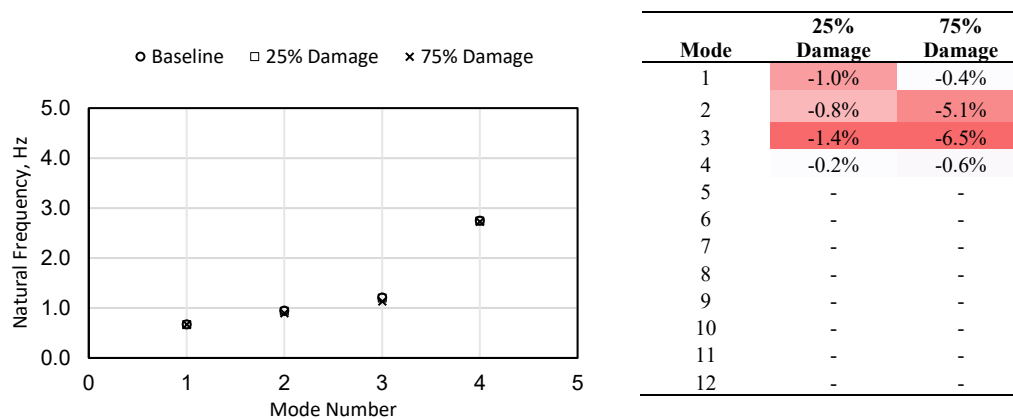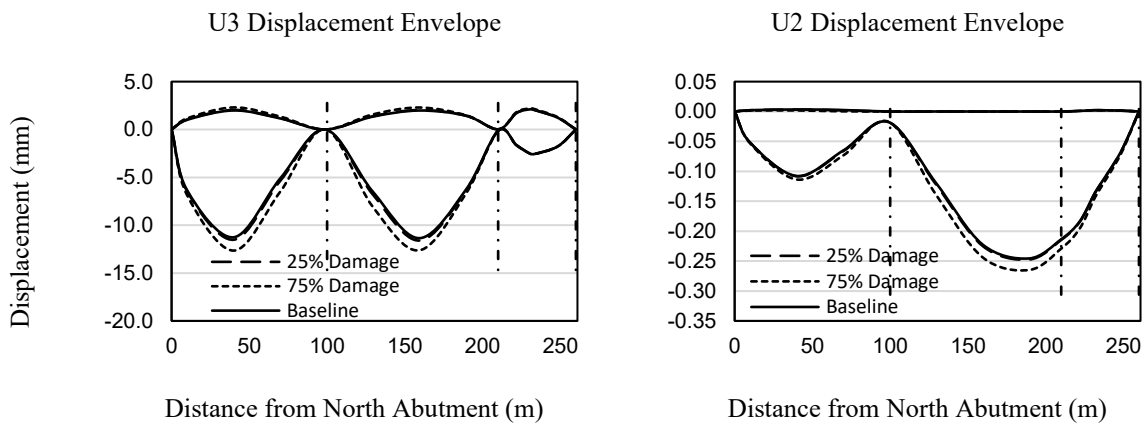

Mode	25% Damage	75% Damage
1	-2.0%	-
2	-1.3%	-
3	-2.1%	-
4	-0.2%	-0.6%
5	-	-
6	-	-
7	-	-
8	-	-
9	-	-
10	-	-
11	-	-
12	-	-
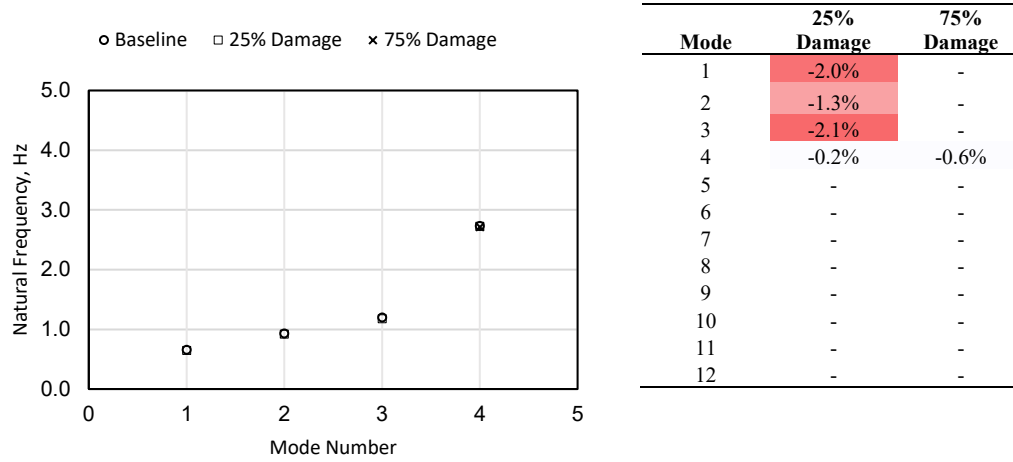
Figure 6.19. U3 direction natural frequency comparison with percent differences (GD-2)

Mode	25% Damage	75% Damage
1	-0.5%	-1.3%
2	0.1%	-
3	0.0%	0.1%
4	-	-
5	-	-
6	-	-
7	-	-
8	-	-
9	-	-
10	-	-
11	-	-
12	-	-
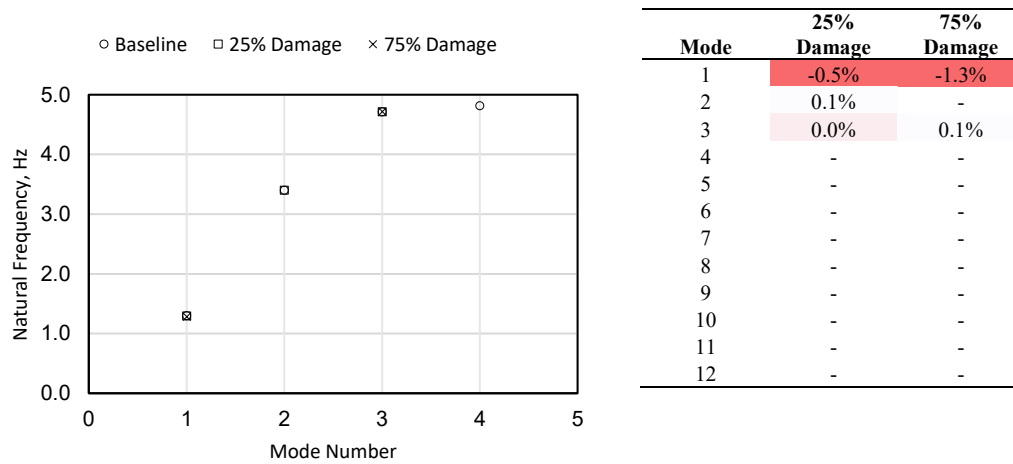
Figure 6.20. U2 direction natural frequency comparison with percent differences (GD-2)

Table 6.9. GD-2 U3 direction MAC comparison

Mode Shape	Natural Frequency (Hz) (Average of P1, P2, P3)			MAC (Average of P1, P2, P3)	
	Baseline	25% Damage	75% Damage	25% Damage	75% Damage
1	0.6673	0.6542	-	0.9984	-
2	0.9401	0.9275	-	0.7653	-
3	1.2080	1.1828	-	0.9977	-
4	2.7405	2.7357	2.7249	0.9989	0.8666
5	-	-	-	-	-
6	-	-	-	-	-
7	-	-	-	-	-
8	-	-	-	-	-
9	-	-	-	-	-
10	-	-	-	-	-
11	-	-	-	-	-
12	-	-	-	-	-

Table 6.10. GD-2 U2 direction MAC comparison

| Mode Shape | Natural Frequency (Hz) (Average of P1, P2, P3) | | | MAC (Average of U1, U2 and U3) | |
	Baseline	25% Damage	75% Damage	25% Damage	75% Damage
1	1.3080	1.3012	1.2907	0.9595	0.8888
2	3.4050	3.4071	-	0.9922	-
3	4.7206	4.7205	4.7244	0.9989	0.9799
4	4.8188	-	-	-	-
5	-	-	-	-	-
6	-	-	-	-	-
7	-	-	-	-	-
8	-	-	-	-	-
9	-	-	-	-	-
10	-	-	-	-	-
11	-	-	-	-	-
12	-	-	-	-	-

Vertical U3 (mm) (Mode 4)   **Transverse U2 (mm) (Mode 1)**

Distance from North Abutment (m)   **Distance from North Abutment (m)**

Figure 6.21. Governing mode shape comparison (GD-2) with vertical dashed lines indicating support locations.

U3 Displacement Envelope

U2 Displacement Envelope
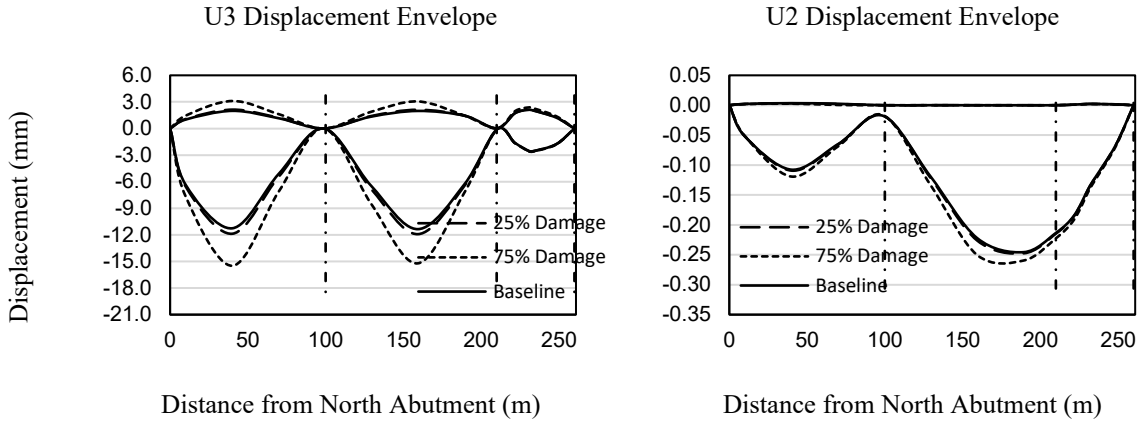
Figure 6.22. Displacement envelope comparison (GD-2) with vertical dashed lines indicating support locations.

6.3.4   Post-tensioning Tendon Damage (PT)

Post-tensioning tendons can be damaged from corrosion or wearing of materials over time which could lead to relaxation. The bridge contains several cantilever, soffit and draped tendons. Draped tendons are present along the entire span for all three spans and are the main tendons responsible for producing negative bending (Figure 6.23). Preliminary analysis showed that this damage case may not be detectable at low levels of damage, so a high level of damage was simulated by applying a 75% tension reduction to the draped tendons.
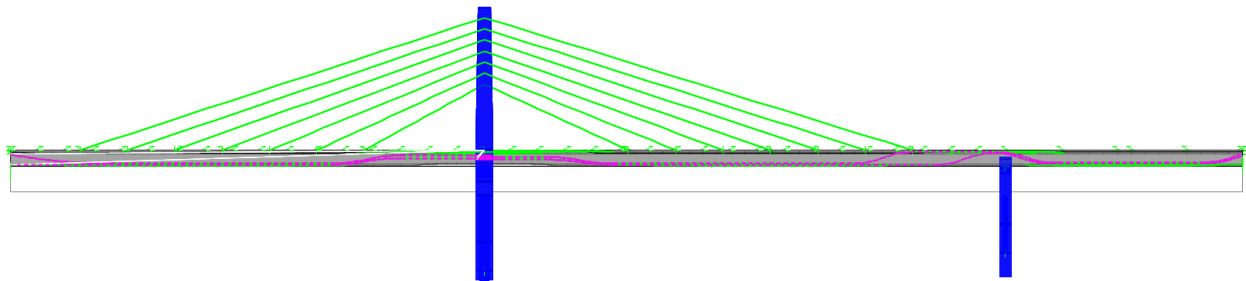
Figure 6.23. Bridge profile view with draped tendons shown.

Tables 6-11 and 6-12 show the average natural frequencies and MAC values for each mode shape, and Figure 6.24 shows the displacement envelopes in the U3 and U2 directions. All modes show no change in natural frequency and MAC values of essentially 1.000 which indicate that there are no changes to modal properties from this damage case. The displacement envelope for the U2 direction show a slight increase in displacement for this damage case which imply this damage case may reduce stiffness in the lateral direction. However, this damage case may not be detectable using modal identification methods under this load case.

Table 6.11. PT U3 direction natural frequency and MAC comparison

Mode Shape	Natural Frequency (Hz) (Average of P1, P2, P3)		MAC (Average of P1, P2, P3)
	Baseline	75% Damage	75% Damage
1	0.6673	0.6673	1.0000
2	0.9401	0.9401	0.9999
3	1.2080	1.2081	1.0000
4	2.7405	2.7408	0.9999
5	-	-	-
6	-	-	-
7	-	-	-
8	-	-	-
9	-	-	-
10	-	-	-
11	-	-	-
12	-	-	-

Table 6.12. PT U2 direction natural frequency and MAC comparison

| Mode Shape	Natural Frequency (Hz) (Average of P1, P2, P3)		MAC (Average of U1, U2 and U3)
	Baseline	75% Damage	75% Damage
1	1.3080	1.3080	1.0000
2	3.4050	3.4044	0.9999
3	4.7206	4.7206	0.9999
4	4.8188	4.8188	0.9997
5	-	-	-
6	-	-	-
7	-	-	-
8	-	-	-
9	-	-	-
10	-	-	-
11	-	-	-
12	-	-	-

Figure 6.24. Displacement envelope comparison (PT) with vertical dashed lines indicating support locations.

6.3.5 Tower Damage (TD)

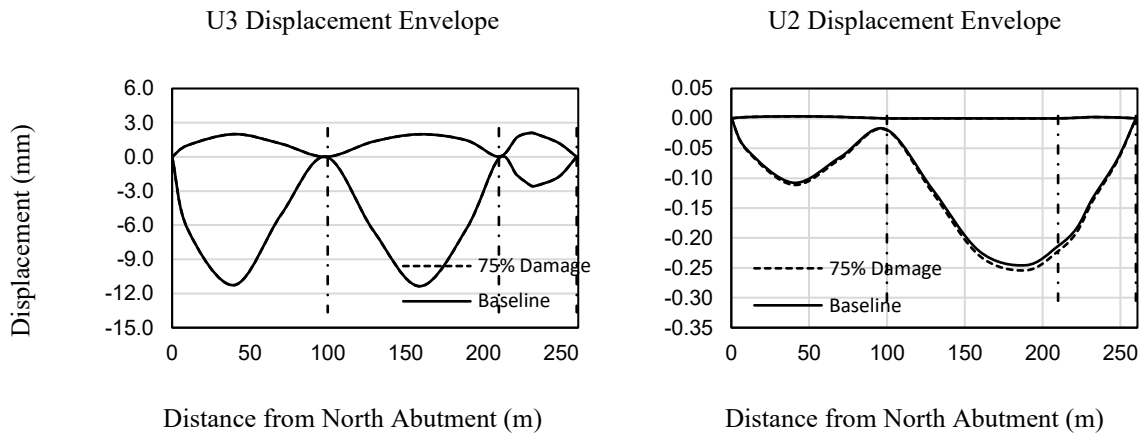The tower damage case is described in detail in Section 5.2.5 but repeated here for convenience. The stay towers are exposed to environmental effects such as high winds due to their height. Damage was simulated to the base of the stay tower, just above the deck, as this would be the point along each tower element that experiences the highest internal shear and bending moments.

The damage was simulated by applying a 25% and 75% stiffness reduction to the base of the stay tower just above deck level. Figure 6.25 and 6.26 show the changes in natural frequency while Tables 6-13 and 6-14 show the average MAC values for each mode shape. The SSI-Cov algorithm detected 4 modes in the U3 direction and 3 modes in the U2 direction at 25% damage. At 75% damage, 4 modes were found in the U3 direction and 3 modes in the U2 direction.

All modes show negligible changes in natural frequency in both the U2 and U3 directions. In the U3 direction, mode shape 2 appears to be the most sensitive to this damage type with MAC values of 0.9336 and 0.9101 for 25% damage and 75% damage, respectively. The rest of the MAC values for the U3 direction are very close to 1.000. In the U2 direction, all modes appear to have MAC values close to 1.000 for 25% damage. Mode 4 appears to be the most sensitive to this damage type at high damage levels with a MAC value of 0.9483 for 75% damage.

Figure 6.27 shows the governing mode shapes in the U3 and U2 directions and Figure 6.28 shows the displacement envelopes in the U3 and U2 directions. In the U3 direction, mode shape 2 would appear to be the most sensitive to damage. Upon further inspection, there is negligible change in deflection between 25% damage and 75% damage despite the 25% damage case varying considerably from the baseline. This implies that there is poor agreement between the mode shapes that is not necessarily indicative of damage. The rest of the mode shapes in the U3 direction do not show any notable changes in deflection. In the U2 direction, mode shape 3 shows a gradual change in deflections across all 3 spans as damage increases. The displacement envelopes, however, do not show any notable changes in max displacement for either the U3 or U2 direction.

Upon inspecting the natural frequencies and mode shapes, there do not seem to be any notable changes across all mode shapes for this damage case. Despite a notable change in deflections for mode shape 3 in the U2 direction for high levels of damage, the small change in deflections at low levels of damage implies that this damage case would be difficult to detect using modal identification methods under this loading scheme for low damage levels.

Mode	25% Damage	75% Damage
1	0.0%	-0.1%
2	-0.1%	-0.3%
3	-0.3%	-0.4%
4	0.0%	0.0%
5	-	-
6	-	-
7	-	-
8	-	-
9	-	-
10	-	-
11	-	-
12	-	-
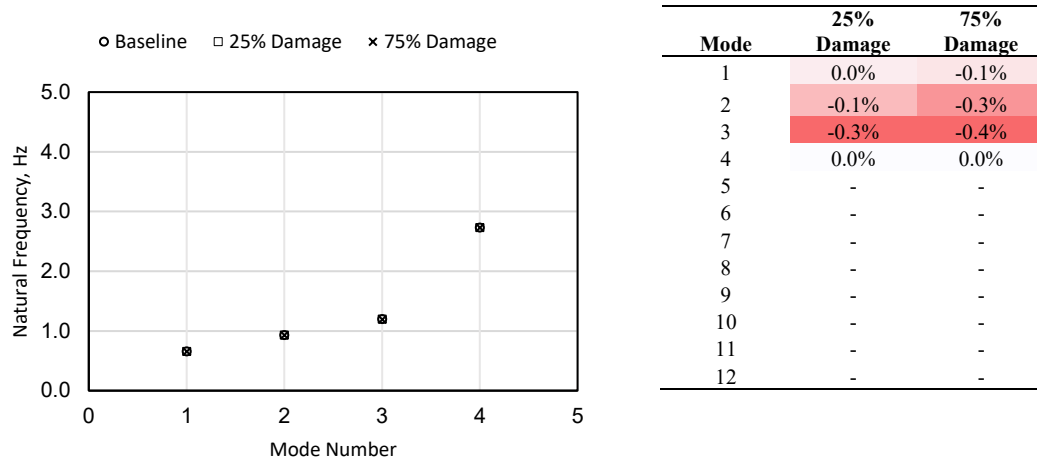
Figure 6.25. U3 direction natural frequency comparison with percent differences (TD)

Mode	25% Damage	75% Damage
1	0.0%	0.7%
2	0.0%	-0.3%
3	0.0%	0.2%
4	-	-
5	-	-
6	-	-
7	-	-
8	-	-
9	-	-
10	-	-
11	-	-
12	-	-
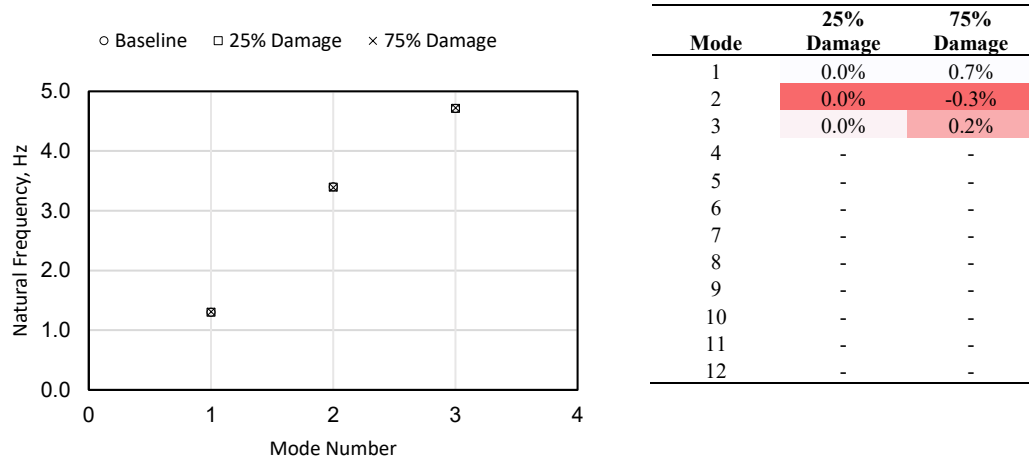
Figure 6.26. U2 direction natural frequency comparison with percent differences (TD)

Table 6.13. TD U3 direction MAC comparison

Mode Shape	Natural Frequency (Hz) (Average of P1, P2, P3)			MAC (Average of P1, P2, P3)	
	Baseline	25% Damage	75% Damage	25% Damage	75% Damage
1	0.6673	0.6672	0.6670	1.0000	0.9977
2	0.9401	0.9390	0.9376	0.9336	0.9101
3	1.2080	1.2046	1.2033	0.9999	0.9999
4	2.7405	2.7408	2.7408	0.9999	0.9998
5	-	-	-	-	-
6	-	-	-	-	-
7	-	-	-	-	-
8	-	-	-	-	-
9	-	-	-	-	-
10	-	-	-	-	-
11	-	-	-	-	-
12	-	-	-	-	-

Table 6.14. TD U2 direction MAC comparison

Mode Shape	Natural Frequency (Hz) (Average of P1, P2, P3)			MAC (Average of U1, U2 and U3)	
	Baseline	25% Damage	75% Damage	25% Damage	75% Damage
1	1.3080	1.3078	1.3173	1.0000	0.9987
2	3.4050	3.4034	3.3954	0.9978	0.9645
3	4.7206	4.7198	4.7291	0.9989	0.9483
4	4.8188	-	-	-	-
5	-	-	-	-	-
6	-	-	-	-	-
7	-	-	-	-	-
8	-	-	-	-	-
9	-	-	-	-	-
10	-	-	-	-	-
11	-	-	-	-	-
12	-	-	-	-	-

Vertical U3 (mm) (Mode 2)   **Transverse U2 (mm) (Mode 1)**

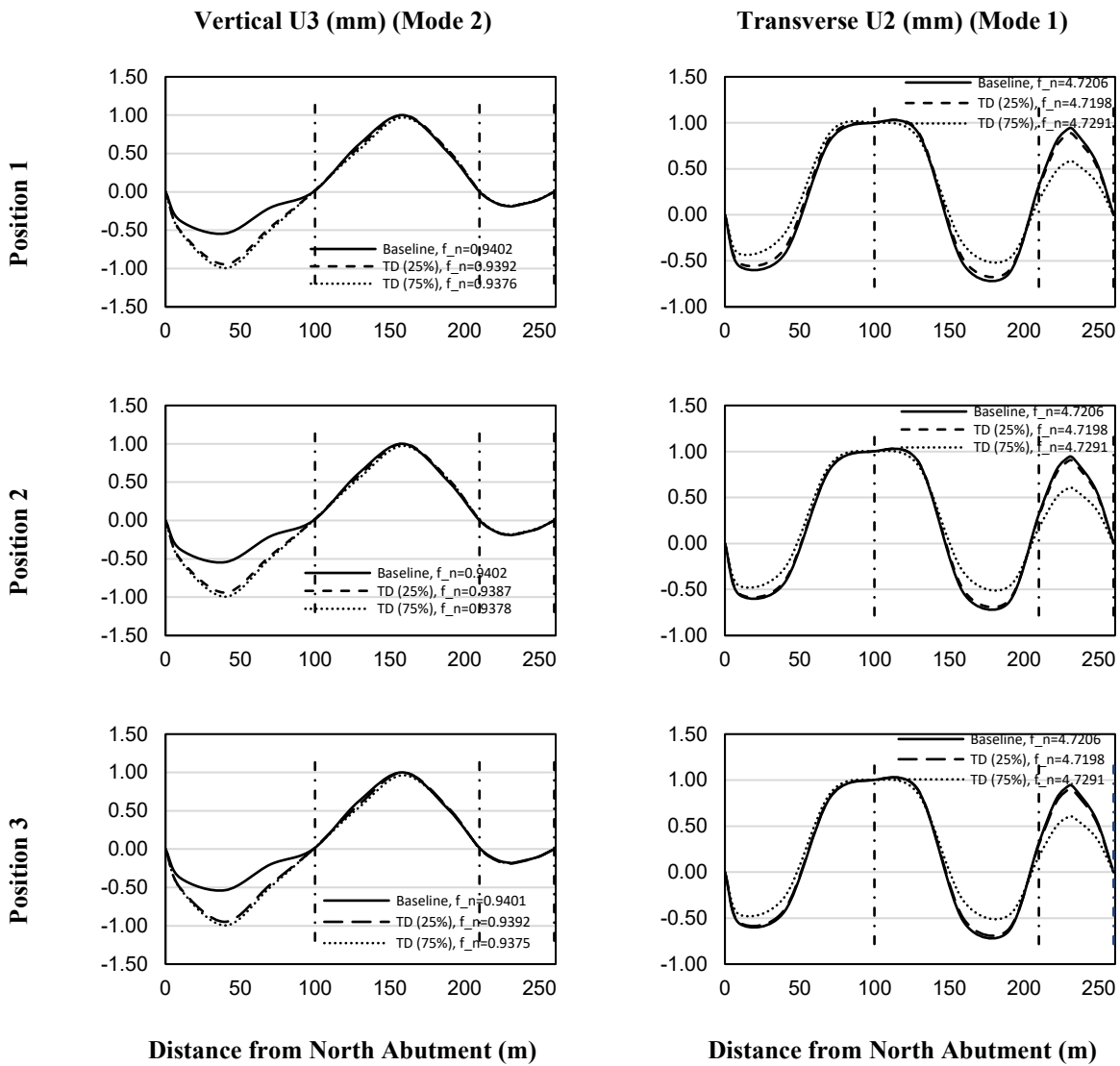**Distance from North Abutment (m)**   **Distance from North Abutment (m)**

Figure 6.27. Governing mode shape comparison (TD) with vertical dashed lines indicating support locations.

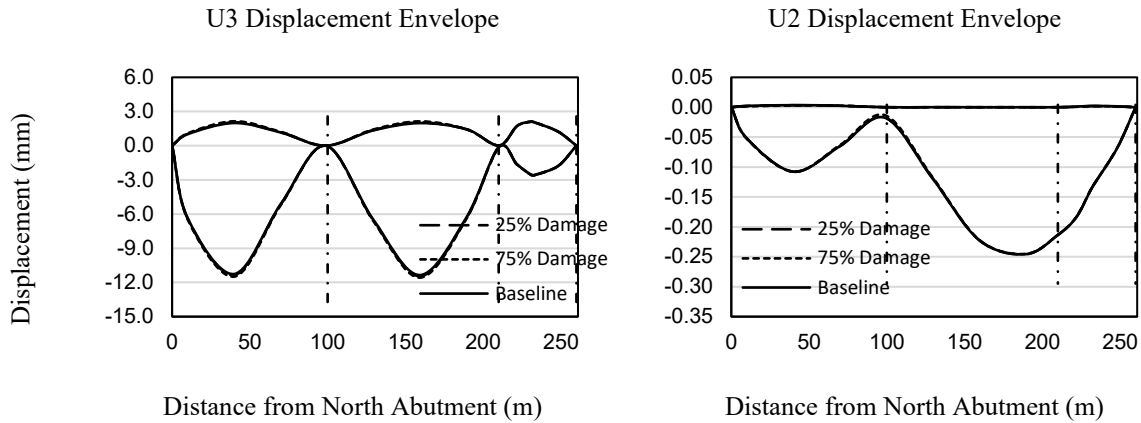U3 Displacement Envelope   U2 Displacement Envelope

Figure 6.28. Displacement envelope comparison (TD) with vertical dashed lines indicating support locations.

6.4 Chapter Summary

This chapter discussed the results of a linear modal time history analysis performed using CSiBridge. A train load was applied to determine the natural frequencies and mode shapes (modal properties) of the Tawatinâ bridge that may be observed in service. A baseline case was modelled to represent a healthy structure and compared with various damage cases. Each damage case simulated damage by reducing the stiffness or tension of specific components of the bridge. Based on the natural frequencies associated with the mode shapes detected in the U3 and U2 directions, it appears that this load case excites lower energy modes in the U3 direction and higher energy modes in the U2 direction. The load case applied did not seem to be effective in exciting modes in the U1 direction.

Stay cable damage (CD-3), post-tensioning tendon (PT) and tower damage (TD) had the least impact to the modes detected under this loading scheme. Although CD-3 and TD saw some notable changes in mode shapes at high levels of damage, there were only minor changes in mode shapes at low levels of damage and no changes in mode shapes at all for PT. Natural frequency changes and MAC values were also minor at all damage levels which imply that other methods (e.g. strain gauges on stay cables or additional accelerometers along stay towers) may be required to detect damage to these components. Additionally, the displacement envelopes had minor or no changes for all three damage cases which imply that greater loads may be required to detect damage to these components.

Bearing damage (BD) and girder damage (GD-1 and GD-2) were found to have notable impacts to the modes detected under this loading scheme. BD had notable changes in natural frequency for lower energy modes (around 1.000 Hz) and appeared to impact mode shapes in the U2 direction

the most. Overall, BD appears to be easy to detect using modal identification methods under this loading scheme. Natural frequency changes for both GD-1 and GD-2 were more noticeable in the U3 direction than the U2 direction. Additionally, fewer modes were detected for high levels of damage which could be a result of the overall stiffness of the bridge decreasing. Despite having slight changes in mode shapes, natural frequencies, the MAC values for GD-1 and GD-2 at low damage levels were fairly close to 1.000. Upon inspecting the displacement envelope at low damage levels, it would appear that a greater load is required to convincingly detect girder damage at low damage levels. However, the given loading scheme appears to be sufficient for detecting damage at higher damage levels which implies that this damage case may still be detectable using modal identification methods under this loading scheme.

It is worth noting that some of the results presented in this chapter could be displaying the effects of structural redundancies. The minimal changes to the mode shapes and displacement envelopes when applying damage to the cables, post-tensioning tendons, and the stay tower show that when damage is applied to just one of these components, other components may be able to transfer the loads. These structural redundancies are present in many modern bridges, especially cable-stayed bridges which are statically indeterminate to high degrees compared. Truss bridges and simply supported bridges typically do not have high degrees of redundancy.

Overall, the findings in this chapter appear to be consist with those found in Chapter 5 in terms of which damage cases were more easily detectable using a modal identification scheme. Relatively few modes were detected under this loading scheme, therefore different loading schemes (e.g., greater mass, higher speeds, trains traveling in both directions, wind loads, etc.) should be considered for future study. Chapter 7 discusses the conclusions and recommendations of the analyses discussed in Chapters 4, 5, and 6.

CHAPTER 7.   SUMMARY AND CONCLUSIONS

7.1   Summary

This thesis presented the modeling and analysis of the Tawatinâ Bridge to investigate the behaviour of the structure under ambient excitation and predicted train loads. Twelve triaxial accelerometers were deployed in four locations along the two longest spans of the bridge. The accelerometer data was processed using a Blackman windowing function and an SSI-Cov MATLAB procedure to determine the modal properties (e.g., natural frequencies and mode shapes) of the bridge and estimate a baseline response for future bridge monitoring. A model was developed using CSiBridge to determine theoretical baseline responses and perform damage simulations. An eigenvector analysis was performed to determine the first 12 mode shapes of the bridge. A linear modal time history analysis was also performed using simulated train loads and an SSI-Cov MATLAB script was used to determine the modal properties of the bridge. In both cases, the modal properties were used as a baseline and compared with other models to determine how effectively different damage types could be detected using the proposed damage detection scheme.

Chapter 2 provided a literature review of existing bridge testing methods including a detailed overview of current state-of-the-art structural health monitoring systems and their applications on real structures. The Tawatinâ Bridge was also introduced, and its significance as an extradosed cable-stayed bridge is discussed. Chapter 3 discussed the proposed layout of accelerometers and strain gauges and different modal identification methods for processing the accelerometer data. The development of the analytical model and the damage cases to be considered for damage simulation were also discussed. Chapter 4 discussed the results of the ambient and dynamic testing data collected from the field using the proposed sensor layout. Chapter 5 discussed the effects of various damage cases on the modal properties of the analytical bridge model which were determined using an eigenvector analysis to determine the hypothetical mode shapes that could be detected using ambient excitation data. Finally, Chapter 6 discussed a linear modal time history analysis performed on the analytical model where a train load was applied and the effects of the same damage cases on the modal properties of the bridge model were determined using an SSI-Cov algorithm.

7.2 Conclusions

Conclusions are drawn from the analysis of field data, and damage simulations using the analytical model as follows.

From Chapter 4, where field data from ambient excitation and dynamic testing is analyzed using FFT and SSI-Cov:

- Data collected from ambient testing appeared to have significant noise as many samples showed no peaks in the FFT plots, or peaks were difficult to identify. Very few mode shapes appeared consistently over different days. It appears that more data collection is required for measuring an accurate baseline response under ambient loads (environmental loads and construction activities) present while data was collected.

- Data collected from dynamic testing appeared to have issues with synchronization which made it infeasible to report accurate mode shapes. However, the forced excitation appeared to be effective in exciting some of the natural frequencies of the bridge, which implies the mode shapes of the bridge could be measured under forced excitation if data is properly synchronized.

- Two improved sensor layouts were provided. These included sensors added to the midspan and support locations while still maintaining twelve total accelerometers. The additional sensor locations would allow for more detailed mode shapes. Additional, data acquisition units capable of data transmission via a wireless network spread throughout the bridge would considerably improve data collection and synchronization.

From Chapter 5, where damage is simulated using the analytical model and modal properties are determined using eigenvector analysis:

- In general, comparing mode shapes and Modal Assurance Criterion (MAC) values were a more effective way of detecting damage than relying on natural frequency changes alone.

- Stay cable damage and tower damage were found to have the least impact on the modal properties of the bridge. These results imply that other SHM methods may be required to detect damage to the stay cables and the stay tower, such as strain gauges on the stay cables or additional accelerometers along the stay towers.

- Bearing damage and girder damage had notable impacts on the modal properties of the bridge with noticeable changes in both MAC and natural frequency values. Theses results

imply that bearing damage and girder damage would be easy to detect using a modal identification scheme.

From Chapter 6, where damage is simulated using the analytical model, dynamic testing is performed using estimated train loads, and modal properties are determined using SSI-Cov:

- The applied train loads used to simulate an empty train excited lower energy modes in the U3 (vertical) direction and higher energy modes in the U2 (transverse) direction with little effect on the U1 (longitudinal) direction.

- Stay cable damage and tower damage were again found to have the least impact on the modal properties of the bridge, further reinforcing the need for other methods to detect damage to these components.

- Bearing damage and girder damage were again found to have notable impacts to the mode shapes detected under the train loading scheme which implies that these damage cases may be detectable using modal identification methods under this loading scheme.

- A closer inspection of the displacement envelopes for these damage cases show that a greater load may be required to convincingly detect damage at low damage levels (e.g., partially, or fully loaded trains). However, the given loading scheme appears to be sufficient for detecting damage at higher levels of damage.

7.3   Recommendations for Future Work

This research project aimed to measure the modal properties of the Tawatinâ bridge and provide a framework for a monitoring system that can effectively establish a baseline response for future structural health monitoring and to predict the effects of various damage cases on the modal properties of the bridge. A baseline response could not be effectively measured due to limitations of the sensor layout and data collection methods, such as limited time on site, and coordinating site visits during the pandemic. Therefore, improvements to the structural health monitoring system have been recommended for future studies. Relocating some of the sensors along the bridge would allow for more detailed mode shapes and eliminate the need for assumptions at support locations. The addition of multiple data acquisition units which can be connected to a wireless network would allow for remote data collection, improved synchronization, and improved FFT resolution. The ability to collect data remotely would also allow for more frequent data collection (including extreme weather events) which would greatly increase the sample size and help determine the true modes of the bridge with statistical confidence.

Improvements to the analytical model could also be made for future study. The shared-use-pathway (SUP) was not included in the model for simplicity. Damage cases were also limited to those discussed in Chapters 5 and 6, and modal properties were calculated using an eigenvector analysis and an SSI-Cov algorithm. Comparisons with other modal identification methods, such as those discussed in Chapter 3, may be of interest for redundancy or to determine the limitations of each method. Additionally, model updating, which updates certain parameters of the analytical model based on data collected in the field, should be considered as part of future structural health monitoring of this bridge.

The techniques and monitoring methods presented in this thesis can be applied to different bridge types. In essence, accelerometers should be spaced along the spans of the bridge to allow for calculating the mode shapes if the goal is global monitoring. Sensor layouts can be optimized and critical areas for placing sensors can be determined using an analytical model. Additional sensors should also be placed at key components based on the bridge type (e.g., post tensioning tendons, steel girders, arches, cables). In the author's experience, structural health monitoring systems for long-term monitoring are rarely used in practice. The decreasing cost and improving ease of use of these systems is allowing them to become more feasible, but an obstacle for adoption is educating asset owners on the advantages and potential long-term cost savings of these systems.

REFERENCES

Alberta Infrastructure and Transportation. (2008). *Bridge inspection and maintenance system : BIM inspection manual. Version 3.1.* Retrieved from Government of Alberta: https://open.alberta.ca/publications/bim-inspection-manual-version-3-1

Barnes, C. L., Trottier, J.-F., & Forgeron, D. (2008). Improved concrete bridge deck evaluation using GPR by accounting for signal depth–amplitude effects. *NDT & E International*, 427-433.

Bayraktar, A., Altunişik, A. C., Sevim, B., Türker, T., & Taş, Y. (2009). Vibration Characteristics of Kömürhan Highway Bridge Constructed with Balanced Cantilever Method. *Journal of Performance of Constructed Facilities*, 90-99.

Bennetts, J., Vardanega, P., Webb, G. T., Denton, S. R., & Loudon, N. (2018). Quantifying Uncertainty in Visual Inspection Data. *Maintenance, Safety, Risk, Management and Life-Cycle Performance of Bridges: Proceedings of the Ninth International Conference on Bridge Maintenance, Safety and Management (IABMAS 2018)*, (pp. 9-13).

Bogas, J. A., Gomes, M. G., & Gomes, A. (2013). Compressive strength evaluation of structural lightweight concrete by non-destructive ultrasonic pulse velocity method. *Ultrasonics*, 962-972.

Casas, J. R., & Gomez, J. D. (2013). Load Rating of Highway Bridges by Proof-loading. *KSCE Journal of Civil Engineering*, 556-567.

Cawley, P., & Adams, R. (1979). The location of defects in structures from measurements of natural frequencies. *The Journal of Strain Analysis for Engineering Design*, 49-57.

Cawley, P., & Adams, R. (1988). The mechanics of the coin-tap method of non-destructive testing. *Journal of Sound and Vibration*, 299-316.

Chen, H.-P., & Ni, Y.-Q. (2018). Modal Analysis of Civil Engineering Structures. In H.-P. Chen, & Y.-Q. Ni, *Structural Health Monitoring of Large Civil Engineering Structures* (pp. 126-164). Wiley Blackwell.

Cheynet, E. (2020). *Operational modal analysis with automated SSI-COV algorithm*. Retrieved from Zenodo: https://zenodo.org/record/3774061

Cheynet, E., Jakobsen, J. B., & Snæbjörnsson, J. (2019). Flow distortion recorded by sonic anemometers on a long-span bridge: Towards a better modelling of the dynamic wind load in full-scale. *Journal of Sound and Vibration*, 214-230.

Cheynet, E., Jakobsen, J. B., & Snæbjörnsson, J. Þ. (2017). Damping estimation of large wind-sensitive structures. *Procedia Engineering*, 2047-2053.

Cheynet, E., Snæbjörnsson, J. Þ., & Jakobsen, J. B. (2017). Temperature Effects on the Modal Properties of a Suspension Bridge. *Dynamics of Civil Structures, Volume 2. Proceedings*

of the 35th IMAC, A Conference and Exposition on Structural Dynamics. Springer International Publishing.

Collings, D., & Gonzalez, A. S. (2013). Extradosed and cable-stayed bridges, exploring the boundaries. *Bridge Engineering*, 231-239.

De Laurentiis, A. (2015). *Investigation and Analysis of the New Walterdale Bridge to Develop a Structural Health Monitoring System.* MSc. Thesis, University of Alberta.

Farrar, C. R., Baker, E. W., Bell, T. M., Cone, K. M., Darling, T. W., Duffey, T. A., . . . Migliori, A. (1994). *Damage characterization and damage detection in the I-40 bridge over the Rio Grande.* Los Alamos National Laboratory.

Farrar, C. R., Duffey, T. A., Cornwell, P. K., & Doebling, S. W. (1999). *Excitation Methods for Bridge Structures.* Los Alamos National Laboratory.

Federal Highway Administration (FHWA). (2016). *LTBP Program's Literature Review on Weigh-in-Motion Systems.* McLean, VA.

Guan, H., Karbhari, V., & Sikorsky, C. (2006). Web-based structural health monitoring of an FRP composite bridge. *Computer-Aided Civil and Infrastructure Engineering*, 39-56.

Guan, H., Karbhari, V., & Sikorsky, C. (2007). Long-term structural health monitoring system for a FRP composite highway bridge structure. *Journal of Intelligent Material Systems and Structures*, 809-823.

Guo, W., Briseghella, B., Xue, J., Luo, X., Chen, Q., & Huang, F. (2020). Analysis of Dynamic Characteristics of Long-span Railway Extradosed Bridge. *2020 International Conference on Intelligent Transportation, Big Data & Smart City (ICITBS)*.

Han, H., Wang, J., Meng, X., & Liu, H. (2016). Analysis of the dynamic response of a long span bridge using GPS/accelerometer/anemometer under typhoon loading. *Engineering Structures*, 238-250.

Hola, J., Sadowski, L., & Schabowicz, K. (2008). Non-destructive Evaluation of the Concrete Floor Quality using Impulse Response S'Mash and Impact-Echo Methods. *Defektoskopie 2008, 38th International Conference.* Brno, Czech Republic.

Huth, O., Feltrin, G., Maeck, J., Kilic, N., & Motavalli, M. (2005). Damage Identification Using Modal Data: Experiences on a Prestressed Concrete Bridge. *Journal of Structural Engineering*.

Kato, M., & Shimada, S. (1986). Vibration of PC Bridge during Failure Process. *Journal of Structural Engineering*.

Kim, J.-T., & Stubbs, N. (2003). Nondestructive Crack Detection Algorithm for Full-Scale Bridges. *Journal of Structural Engineering*, 1358-1367.

Kocherla, A., & Subramaniam, K. V. (2020). Stress and damage localization monitoring in fiber-reinforced concrete using surface-mounted PZT sensors. *Measurement Science and Technology*.

La Mazza, D., Basone, F., Longo, M., Daro, O., & Cigada, A. (2023). Anomaly Detection Through Long-Term SHM: Some Interesting Cases on Bridges. *Dynamics of Civil Structures, Volume 2. Proceedings of the 40th IMAC, A Conference and Exposition on Structural Dynamics 2022* (pp. 57-65). Springer.

Lee, L. S., Karbhari, V., & Sikorsky, C. (2007). Structural Health Monitoring of CFRP Strengthened Bridge Decks Using Ambient Vibrations. *Structural Health Monitoring*, 199-214.

Li, H., & Ou, J. (2015). The state of the art in structural health monitoring of cable-stayed bridges. *Journal of Civil Structural Health Monitoring*, 43-67.

Li, H., Ou, J., Zhao, X., Zhou, W., Li, H., & Zhou, Z. (2006). Structural Health Monitoring System for the Shandong Binzhou Yellow River Highway Bridge. *Computer-Aided Civil and Infrastructure Engineering*, 306-317.

Lin, H., Xiang, Y., & Jia, Y. (2018). Study on Health Monitoring System Design of Cable-Stayed Bridge. *Facing the Challenges in Structural Engineering*, 216-228.

Lu, P., Phares, B. M., Greimann, L., & Wipf, T. J. (2010). Bridge Structural Health-Monitoring System Using Statistical Control Chart Analysis. *Transportation Research Record Journal of the Transportation Research Board*, 123-131.

Magalhaes, F., Cunha, A., & Caetano, E. (2009). Online automatic identification of the modal parameters of a long span arch bridge. *Mechanical Systems and Signal Processing*, 316-329.

Meng, X., Dodson, A., & Roberts, G. (2007). Detecting bridge dynamics with GPS and triaxial accelerometers. *Engineering Structures*, 3178-3184.

Meng, X., Roberts, G. W., Cosser, E., & Dodson, A. H. (2003). Real-time Bridge Deflection and Vibration Monitoring using an Integrated GPS/Accelerometer/Pseudolite System. *11th FIG Symposium on Deformation Measurements*, (pp. 25-28). Santorini, Greece.

Middleton, C. R., Fidler, P. R., & Vardanega, P. J. (2016). *Bridge Monitoring: A practical guide.* ICE Publishing.

Mirza, S. (2007). *Danger Ahead: The Coming Collapse of Canada's Municipal Infrastructure.* Ottawa Ontario: Federation of Canadian Municipalities.

Moschas, F., & Stiros, S. (2011). Measurement of the dynamic displacements and of the modal frequencies of a short-span pedestrian bridge using GPS and an accelerometer. *Engineering Structures*, 10-17.

National Instruments. (2000). *The Fundamentals of FFT-Based Signal Analysis and Measurement.* National Instruments Corporation.

National Instruments. (N.D.). *Understanding FFTs and Windowing*. Retrieved from National Instruments: https://www.ni.com/en/shop/data-acquisition/measurement-fundamentals-main-page/analog-fundamentals/understanding-ffts-and-windowing.html#:~:text=Windowing%20consists%20of%20multiplying%20the,continuous%20waveform%20without%20sharp%20transitions.

Ni, Y., Alamdari, M., Ye, X., & Zhang, F. (2021). Fast operational modal analysis of a single-tower cable-stayed bridge by a Bayesian method. *Measurement*.

Niu, J., Zong, Z., & Chu, F. (2015). Damage identification method of girder bridges based on finite element model updating and modal strain energy. *Science China Technological Sciences*, 701-711.

Ogier, E. (2021). *Hierarchical Clustering*. Retrieved from MATLAB Central File Exchange: https://www.mathworks.com/matlabcentral/fileexchange/56844-hierarchical-clustering

Olaszek, P., Swit, G., & Casas Rius, J. (2010). Proof load testing supported by acoustic emission: an example of application. *Bridge Maintenance, Safety, Management and Life-Cycle Optimization: Proceedings of the Fifth International IABMAS Conference*, (pp. 11-15). Philadelphia, USA.

Peeters, B., & De Roeck, G. (2001). Stochastic System Identification for Operational Modal Analysis: A Review. *Journal of Dynamic Systems, Measurement, and Control*.

Peeters, B., & Ventura, C. (2003). Comparative Study of Modal Analysis Techniques for Bridge Dynamic Characteristics. *Mechanical Systems and Signal Processing*, 965-988.

Petersen, Ø., Øiseth, O., & Lourens, E. (2020). Investigation of dynamic wind loads on a long-span suspension bridge identified from measured acceleration data. *Journal of Wind Engineering & Industrial Aerodynamics*.

Phares, B. (2001). Highlights of study of reliability of visual inspection. *Annual Meeting of TRB Subcommittee AC2C05 (1): Non-destructive Evaluation of Structures, FHWA Report No FHWARD-01-020 and FHWA-RD-01-0212001*.

Phares, B., Lu, P., Wiipf, T., Greimann, L., & Seo, J. (2013a). Evolution of a Bridge Damage-Detection Algorithm. *Transportation Research Record Journal of the Transportation Research Board*, 71-80.

Phares, B., Lu, P., Wiipf, T., Greimann, L., & Seo, J. (2013b). Field Validation of a Statistical-Based Bridge Damage-Detection Algorithm. *Journal of Bridge Engineering*, 1227-1238.

Pines, D., & Aktan, A. (2002). Status of structural health monitoring of long-span bridges in the United States. *Progress in Structural Engineering and Materials*, 372-380.

Podder, P., Khan, T. Z., Khan, M. H., & Rahman, M. M. (2014). Comparative Performance Analysis of Hamming, Hanning and Blackman Window. *International Journal of Computer Applications*.

Raja, B. N., Miramini, S., Duffield, C., Sofi, M., & Zhang, L. (2021). Infrared thermography detection of delamination in bottom of concrete bridge decks. *Structural Control & Health Monitoring*.

Rehman, S. K., Ibrahim, Z., Memon, S. A., & Jameel, M. (2016). Nondestructive test methods for concrete bridge: A review. *Construction and Building Materials*, 58-86.

Rucka, M., & Wilde, K. W. (2013). Experimental Study on Ultrasonic Monitoring of Splitting Failure in Reinforced Concrete. *Journal of Nondestructive Evaluation*, 372-383.

Seo, J., Hu, J. W., & Lee, J. (2016). Summary Review of Structural Health Monitoring Applications for Highway Bridges. *Journal of Performance of Constructed Facilities*.

Shi, Z. Y., Law, S. S., & Zhang, L. M. (2000). Structural damage detection from modal strain energy change. *Journal of Engineering Mechanics*.

Sun, M., Alamdar, M. M., & Kalhori, H. (2017). Automated Operational Modal Analysis of a Cable-Stayed Bridge. *Journal of Bridge Engineering*.

Svensson, H. (2013). *Cable-Stayed Bridges: 40 Years of Experience Worldwide.* Berlin, Germany: Wilhelm Ernst & Sohn.

Tomlinson, D., Moardi, F., Hajiloo, H., Ghods, P., & Alizadeh, A. (2017). Early age electrical resistivity behaviour of various concrete mixtures subject to low temperature cycling. *Cement and Concrete Composites*, 323-334.

Transportation Research Board of the National Academies. (2013). *Nondestructing Testing to Identify Concrete Bridge Deck Deterioration.* Washington, D.C.: Transportation Research Board.

Vardanega, P., Webb, G., Fidler, P., & & Middleton, C. (2016). Assessing the potential value of bridge monitoring systems. *Bridge Engineering*, 126-138.

Whelan, M. J., & Janoyan, K. D. (2009). In-Service Diagnostics of a Highway Bridge from a Progressive Damage Case Study. *Journal of Bridge Engineering*.

Wipf, T. J., Phares, B. M., Doornink, J. D., Greimann, L. F., & Wood, D. L. (2007). *Evaluation of Steel Bridges (Volume I): Monitoring the Structural Condition of Fracture-Critical Bridges using Fiber Optic Technology.* Ames, IA: Bridge Engineering Centre.

Wong, K.-Y. (2004). Instrumentation and health monitoring of cable-supported bridges. *Structural Control and Health Monitoring*, 91-124.

Wong, K.-Y. (2004). Instrumentation and health monitoring of cable-supported bridges. *Structural Control and Health Monitoring*, 91-124.

Wong, K.-y., Chan, W.-Y., Man, K.-L., Mak, W. L., & Lau, C. (2000). Structural health monitoring results on Tsing Ma, Kap Shui Mun, and Ting Kau bridges. *SPIE's 5th Annual International Symposium on Nondestructive Evaluation and Health Monitoring of Aging Infrastructure* (pp. 288-299). Newport Beach, CA: SPIE.

Wong, K.-Y., Lau, C., & Flint, A. (2000). Planning and implementation of the structural health monitoring system for cable-supported bridges in Hong Kong. *SPIE's 5th Annual International Symposium on Nondestructive Evaluation and Health Monitoring of Aging Infrastructure* (pp. 266-275). Newport Beach, CA: SPIE.

Wu, Z. (2021). Flexural and Shear Response of Deteriorated Prestressed Concrete Girders Taken from a Decommissioned Bridge in Alberta. *Master of Science Thesis Report*. University of Alberta.

Xu, X., Ren, Y., Huang, Q., Fan, Z.-Y., Tong, Z.-J., Chang, W.-J., & Liu, B. (2020). Anomaly detection for large span bridges during operational phase using structural health monitoring data. *Smart Materials and Structures*.

Xu, Y. L., & Xia, Y. (2013). *Structural Health Monitoring of Long-Span Suspension Bridges.* London: Taylor & Francis Group.

Yang, X.-M., Yi, T.-H., Qu, C.-X., Li, H.-N., & Liu, H. (2021). Performance Assessment of a High-Speed Railway Bridge through Operational Modal Analysis. *Journal of Performance of Constructed Facilities*.

Ye, S., Lai, X., Bartoli, I., & Aktan, A. E. (2020). Technology for condition and performance evaluation of highway bridges. *Journal of Civil Structural Health Monitoring*, 573-594.

Yonggang. (2021). *Fast Hierarchical Clustering Method - PHA*. Retrieved from MATLAB Central File Exchange: https://www.mathworks.com/matlabcentral/fileexchange/46134-fast-hierarchical-clustering-method-pha

Zhai, W., Han, Z., Chen, Z., Ling, L., & Zhu, S. (2019). Train–track–bridge dynamic interaction: a state-of-the-art review. *International Journal of Vehicle Mechanics and Mobility*, 984-1027.